Section 3:

Session 3: Structural Analysis and Fracture Mechanics Issues

Probabilistic Fracture Mechanics Analysis to Support Inspection Intervals for RPV Top Head Nozzles

Peter Riccardella, Nathaniel Cofie, Angah Miessi
Stan Tang, Bryan Templeton
Structural Integrity Associates

U.S. Nuclear Regulatory Commission
Argonne National Laboratory

Conference on Vessel Head Penetration Inspection,
Cracking, and Repairs

September 29 – October 2, 2003
Gaithersburg, Maryland

Summary

A Probabilistic Fracture Mechanics (PFM) tool for RPV top head nozzles has been developed under sponsorship of EPRI and the PWR Materials Reliability Program (MRP). Extensive analyses have been performed with this tool to predict the probability of leakage and failure versus plant operating time for various input parameters that influence nozzle structural reliability. Significant input parameters include head operating temperature, effective full power years of operation, inspection type (visual or non-visual NDE) and inspection interval. The PFM algorithm includes an empirical time-to-leakage or cracking correlation based on a Weibull model of plant inspections through Spring 2003. It incorporates finite element stress and stress intensity factor calculations of various nozzle configurations containing axial and circumferential cracks, and a statistical representation of crack growth rate data for Alloy 600. The model has been benchmarked against field experience with leaking and circumferential cracking.

The PFM model can be used to define susceptibility categories for plants based on their operating time and head temperature, as well as to study the effect of various inspection types and intervals. The probabilistic model provides a useful tool to guide long term inspect and repair versus head replacement decisions.

Introduction

Cracking and leakage has been observed for several years in the reactor pressure vessel (RPV) top head nozzles of operating PWRs in the Untied States. The cracking is attributed to a phenomenon known as Primary Water Stress Corrosion Cracking (PWSCC) of the nozzle material, Alloy-600 nickel alloy and its associated weld metals. Several plants have detected leakage and/or cracking. The leakage is generally detected in the form of small deposits of boric acid crystals that emanate from the annuli between the nozzles and the vessel head. In other cases, cracking has been detected, with or without evidence of leakage, via volumetric non-destructive examination (NDE) of the nozzles and/or weldments. A schematic of a typical RPV head CRDM nozzle configuration and the general nature of the observed cracking are shown in Figure 1.

Initially, leaking nozzles were thought to be exclusively the result of axial cracks in the nozzles, and thus it was believed that they did not present a safety concern to the plants. However, as more examinations were performed, several findings arose that called this hypothesis into question. Specifically:

- Relatively long circumferential cracks were observed in two nozzles in the Oconee Unit 2 RPV head, and several other plants also discovered shorter circumferentially oriented cracks.
- As a result of allowing leakage to exist for an extended period, and thus build up massive deposits of boric acid on the vessel head, the Davis-Besse plant experienced severe wastage corrosion of their RPV head, to the point that safety margins in the head were reduced below ASME Code allowables.
- Circumferential cracking was discovered in the North Anna Unit 2 head in nozzles that had no apparent signs of boric acid deposits indicating leakage

This paper summarizes a probabilistic fracture mechanics (PFM) evaluation of the probability of a circumferential crack initiating (or forming as a consequence of branching or redirection of an axial crack), and growing to a size that could cause a nozzle ejection-type failure. Major elements of the PFM evaluation include:

- computation of applied stress intensity factors for circumferential cracks in various nozzle geometries as a function of crack length,
- determination of critical circumferential flaw sizes for nozzle failure,
- an empirical (Weibull) analysis of the probability of nozzle cracking or leakage as a function of operating time and temperature of the RPV head,
- statistical analysis of PWSCC crack growth rates in the PWR primary water environment as a function of applied stress intensity factor and service temperature, and
- modeling of the effects of inspections, including inspection type, frequency and effectiveness.

The elements and major assumptions of the method are summarized in this paper, and a sampling of the results is presented for a typical RPV top head as a function of operating time and temperature.

.

PFM Methodology

Figure 2 presents a flow chart of the probabilistic fracture mechanics methodology developed for the RPV top head nozzles. The methodology has been implemented in a computer program (MRPER) which is described in detail in Reference [1]. The MRPER methodology implements a time-dependent Monte Carlo analysis scheme which predicts the probability of leakage and nozzle ejection versus time for a specific set of top head parameters. Deterministic parameters specific to the top head being analyzed include number of nozzles, the angle of each nozzle with respect to the head, nozzle diameter and wall thickness, number of heats of nozzle material, and identification of which nozzles are from which heat. Another plant-specific input consists of K-matrices for each of several nozzle angles. These are matrices of stress intensity factor versus crack length for several characteristic nozzle angles (usually four) into which individual nozzles are lumped based on their angle. The K-matrices are obtained from deterministic fracture mechanics analyses of the specific head geometry and may include stress intensity factor data for ranges of nozzle yield strengths and nozzle-to-vessel interference fits, for cracks centered at both the uphill and downhill sides of the nozzles.

Statistical parameters (random variables) utilized in the Monte Carlo analysis include:

- head operating temperature
- yield strengths for each heat of nozzle material
- nozzle interferences (or gaps)
- number of assumed cracks per nozzle (for NDE detection)
- initial crack size and crack initiation time (for NDE detection)
- distribution of crack locations (uphill or downhill)
- Weibull distribution of time to leakage or cracking (dependent on plant operating time and head temperature)
- stress corrosion crack growth law
- correlation factor between time to crack initiation and crack growth, and
- critical crack size for each characteristic nozzle angle.

Various distribution types are used, as appropriate, for these statistical parameters (normal, triangular, log-normal, log-triangular, Poisson, Weibull, etc.), along with their mean and standard deviation or range. As illustrated in Figure 2, the analysis algorithm consists of two nested Monte Carlo simulation loops, which step through time for each nozzle in a head, and then for the total number of head simulations specified. For each nozzle simulation, a time to leakage (or cracking) is predicted based on the Weibull distribution. When leakage is predicted, a circumferential crack equal to 30º of nozzle circumference is assumed to exist, of a through-wall depth specified by the user (100%

through-wall has been assumed for the runs presented here). The assumed circumferential crack is then grown based on the nozzle-specific stress intensity factor, which is interpolated based on nozzle yield strength and interference fit, and using a stress corrosion crack growth law obtained from random sampling of the crack growth rate distribution. The crack growth analysis for each nozzle continues until either the end of the evaluation period, or until the crack length reaches the critical flaw size for that nozzle (established based on random sampling of the critical crack size distribution). The analysis is repeated for each nozzle in the head, and then the user repeats the process for the total number of head simulations specified. The software records the total number of top heads predicted to experience at least one leak or failure as a function of operating time, as well as the total number of nozzles with predicted leaks or failures versus time. The probability of a nozzle leak or failure at a given time is the ratio of the number predicted to have leaks or failures divided by the total number of top heads simulated.

A correlation factor between crack initiation and crack growth is included as a user input, which allows one to simulate an inter-relationship between the time to initiation and the crack growth rate for each nozzle. A high negative correlation factor (-0.9 or -1) implies that a material heat that tends to be bad from the perspective of crack initiation (i.e. leaks early in life) would also have a high crack growth rate. A correlation factor of 0 implies no correlation.

The program also permits the user to specify inspections performed at various times within the analysis interval. Either visual inspections (for leakage) or non-destructive examinations (for cracking) or some combination thereof may be specified. For each inspection the user also specifies inspection coverage (% of nozzles inspected) and reliability (probability of detecting a leak if it exists in a visual examination or probability of detection versus crack depth for a non-destructive examination). When inspections are performed, cracks in nozzles that are predicted to be detected are removed from the simulation, and are no longer considered threats to grow to leakage or failure. One can thus perform multiple analyses, with and without various forms of inspection at various intervals, to compare the probabilities of leakage and failure, and thus evaluate the effectiveness of different inspection regimens.

Stress Intensity Factor Calculations

A key element of this PFM evaluation is computation of applied stress intensity factors for circumferential cracks of various lengths ranging from relatively small cracks that might be initiated once leakage is detected, up to and including critical crack lengths that could potentially lead to gross failure of the nozzles (nozzle ejection). Figure 3 illustrates the general nature of the circumferential cracking assumed for this evaluation. Located in a plane above and parallel to the top of the J-groove weld, the circumferential cracking can begin and end at any azimuth around the nozzle, but for purposes of this evaluation, two flaw locations were assumed as illustrated, one centered on the uphill side of angled nozzles, and the other centered on the downhill side.

The basic approach used to determine stress intensity factors for the assumed top head nozzle cracks is the widely-accepted superposition technique for fracture mechanics analysis of complex geometries and stresses [2] illustrated schematically in Figure 4. Operating and residual stress analyses were obtained from prior three-dimensional, elastic-plastic finite element models of the nozzle, head and J-groove weld region, but with no cracks present [3]. Stresses from these uncracked nozzle models were then superimposed on simplified elastic finite element models of the nozzles, without the vessel head or J-groove welds, but with cracks of various lengths and depths built into the models, and with boundary conditions applied that represent the constraints imposed by the vessel head and J-groove welds. The resulting stress intensity factors are tabulated, in the form of K-matrices, for input to the PFM model.

Since U.S. plants have varying numbers of nozzles, ranging from 37 to 101 depending on plant size and type, and with nozzles penetrating the heads at various angles with respect to the head tangent angle at the attachment point, numerous nozzle and flaw geometries need to be addressed. Different plant types also have different nozzle, head and J-groove weld geometries, and as mentioned above, cracks are assumed at both the uphill and downhill sides of angled nozzles. To limit the analyses to a practical number of cases, a set of characteristic plants (one each from two PWR vendors and two from a third vendor) have been selected for analysis. An evaluation was performed, which demonstrates that the characteristic plants selected for analysis bound the U.S. PWR fleet in terms of the parameters important to nozzle stresses in the vicinity of the RPV top head J-groove welds (Figure 5).

Typical stress and stress intensity factor results are illustrated in Figures 6 – 8. Figure 6 illustrates the applied plus residual stress distribution for the steepest angle nozzle in a B&W type plant (Plant A). The stresses are averaged through the thickness of the nozzles, and plotted at several slices parallel to the root of the J-groove weld. The curve labeled 1400s is right at the root of the weld, the 1500s slice is ¼ inch above that, etc. Also shown as a heavy line in the figure is an envelope curve, which bounds the stresses at all sections at or above the weld. For conservatism, and to allow for potential meandering of the crack in different stress planes, the envelope stress curve was used in the stress intensity factor computations.

Figures 7 and 8 illustrate stress intensity factors computed in this manner for through-wall crack lengths ranging from 30º to 300º for selected plant types and nozzle angles. Figure 7 results are for cracks centered at the uphill side of the nozzles, while Figure 8 illustrates similar results for cracks centered at the downhill side.

Finally, critical flaw sizes were determined for each of the characteristic plants. Due to the inherent ductility of the Alloy-600 nozzle material, limit load analysis was used to determine critical circumferential crack lengths in the nozzles. With the limit load approach, the net effect of cracking is to reduce the cross sectional area of the nozzle; and failure is predicted when net section collapse (NSC) of the nozzle cross-section minus the crack cross-section is predicted.

Weibull Analysis of Time to Cracking or Leakage

RPV top head inspections have been conducted in U.S. PWRs since the mid-1990s. Initially, only a sampling of U.S. plants was inspected, in response to overseas cracking incidents. In 2001, when cracking and leakage began to be discovered in U.S. Plants, a more complete inspection program began to evolve, primarily bare metal visual (BMV) examinations of heads, looking for evidence of boric acid residue (resulting from RPV coolant leakage) in the annular regions between the nozzles and vessel head. When evidence of such leakage was detected, plants would proceed to non-visual NDE (ultrasonic or eddy current examinations) to verify the source(s). As time progressed, and more degradation was detected, plants began to perform pre-emptive NDE, even when no evidence of leakage was present. In February 2003, the U.S. NRC issued an order requiring extensive NDE examinations in many plants, and a substantial number were performed in the Spring 2003 outage season. By the end of Spring 2003, a total of 30 of the 69 U.S. PWRs had performed some form of NDE, of which 14 plants had detected leakage or some form of cracking.

U.S. plants have been prioritized for inspection using an approximate susceptibility ranking for top head nozzle cracking based on a parameter known as Effective Degradation Years (EDYs). The definition of EDYs takes into account the widely accepted temperature dependence of the PWSCC cracking phenomenon. EDYs are effective operational years at a reference temperature of 600ºF, and are determined from plant effective full power years (EFPYs) at various head temperatures by the following expression:

$$EDY_{600^\circ\mathrm{F}} = \sum_{j=1}^{n}\left\{\Delta EFPY_j \exp\left[-\frac{Q_i}{R}\left(\frac{1}{T_{head,j}}-\frac{1}{T_{ref}}\right)\right]\right\}$$

where:

$EDY_{600^\circ\mathrm{F}}$ = total effective degradation years through February 2001, normalized to a reference temperature of 600°F
$EFPYj$ = effective full power years at head temperature j
Q_i = activation energy for crack initiation (50 kcal/mole)
R = universal gas constant (1.103×10^{-3} kcal/mol-°R)
$T_{head,j}$ = 100% power head temp. during time period *j* (°R = °F + 459.67)
T_{ref} = reference temperature (600°F = 1059.67°R)
n = number of different head temperatures during plant history

Figure 9 presents a summary of inspection results from U.S. PWR top heads through the Spring 2003 outage season. The data are plotted in terms of head operating temperature (horizontal axis), and number of effective full power years at the current head operating temperature (vertical axis). A few plants have operated at multiple head operating temperatures, in which cases the data are plotted at equivalent EFPYs at the current temperature using the above equation, but with the reference temperature set equal to the current head temperature for that plant instead of 600ºF. Data points in Figure 9 are differentiated by type of inspections performed (BMV or NDE), and inspection findings (clean, leaks, or cracks but no leaks). Also shown are lines of constant EDY, plotted in accordance with the above equation. Referring to the 10 EDY curve, it is seen that, in accordance with the above-described EDY algorithm, a plant operating at a 560ºF head temperature requires more than 50 years to accumulate the same effective degradation as a plant with a 600ºF head temperature would accumulate in ten years.

From Figure 9, the EDY-based susceptibility model is seen to be well-corroborated by plant inspection data to date. All plants that have observed leaks (solid triangles) are on or above the 15 EDY curve. Plants which have experienced cracks but not leaks (open squares) are all above the 10 EDY curve. Numerous low EDY plants have performed visual examinations with no leakage observed (solid diamonds). A total of 16 plants, of ages 8 EDY or greater, had performed NDE to through Spring 2003, with no indications of cracking (lightly shaded squares).

For purposes of the Weibull analysis, the population has been limited to just those plants that had leaks or cracks or that have performed non-visual NDE and were found clean. Plants that performed only visual examinations and were found clean (solid diamond points in Figure 9) were not included. Limiting the population in this manner is conservative, since it assumes that leaking or cracking may have existed and gone undetected by those visual exams.

Data for the 30 plants that performed NDE or experienced cracks or leaks have been adjusted, as described below, and fit to a standard two-parameter Weibull cumulative distribution function [4] as follows:

$$F(t) = 1\text{-EXP}\ (-(t/\theta)^{\beta})$$

where: $F(t)$ = fraction of vessel heads with a leak or crack
t = time to most recent inspection (in EDYs)
θ = characteristic life or scale parameter
β = slope or shape parameter

The lightly shaded circles in Figure 10 represent the 14 plants that have detected leakage or cracking, plotted on Weibull paper with the ordinate equal to EDYs at the time of inspection. Direct fitting of these data would lead to a very steep slope (i.e. a high value of the Weibull shape parameter β), since the data show only one plant with cracking at less than ~14 EDYs, and a very high percentage of leakage or cracking for plants with 16 or more EDYs. However, this apparent trend is the result of an "inspection transient", since little or no top head inspections (especially NDE) were conducted in US plants before 2000. It is likely that many of these plants, especially those in which multiple cracks or leaks were observed in the initial inspections, had cracking present earlier in their operating lives that wasn't detected. Also, based on other PWSCC experience in Alloy 600, including laboratory data and steam generator tube failures in PWRs, a Weibull slope of 3 is considered to be a reasonable value for this phenomenon [5].

Based on the above discussion, it was decided to employ a WeiBayes approach [4] to fit the data, assuming a Weibull slope of 3 ($\beta = 3$ in the above equation) as a baseline for the Weibull analysis, and to extrapolate the inspection data back to the time at which cracking or leakage is first predicted to occur using this slope.

The adjusted data are indicated by the solid circles in Figure 10. The "extrapolated-back" EDYs at 1st cracking were curve fit via a median rank regression algorithm in Weibull graph coordinates, assuming a slope of 3, to determine the best fit shown by the heavy solid line in Figure 10. (In selected cases, thin dashed lines are drawn connecting the data for a specific plant, before and after the adjustment, to illustrate the effect of the extrapolation.) The 16 plants that were inspected and found clean were treated as "suspended items" in the analysis, in accordance with the standard approach described in Reference [4].

It is seen from Figure 10 that the extrapolated data are very well fit by the Weibull line with a slope of 3, and result in a characteristic time to failure (time to 1st cracked or leaking nozzle in 63% of the plants) of 15.2 EDYs.

PWSCC Crack Growth Rates

Reference [6] presents an extensive compilation of PWSCC crack growth rate data for Alloy 600 material in the PWR primary coolant environment. The data are from controlled testing of 158 fracture mechanics specimens fabricated from 22 heats of CRDM nozzle, thick-wall tube, rolled bar, and forged bar material and 4 heats of plate material. Data are included from tests conducted at several laboratories around the world. The data were reviewed by an international panel of experts in the area of stress corrosion crack growth, and only tests that incorporated careful control of applied load and temperature, as well as accurate measurement of crack growth rates were considered. These data formed the basis for a statistical analysis to develop distributions of crack growth rates for use in the PFM analyses.

The data were first fit to a standard power-law relationship for crack growth rate as a function of applied stress intensity factor:

$$\dot{a} = \exp\left[-\frac{Q_g}{R}\left(\frac{1}{T}-\frac{1}{T_{ref}}\right)\right]\alpha\left(K-K_{th}\right)^{\beta}$$

where:

$\dot{a}$ = crack growth rate at temperature T in m/s (or in/hr)
Q_g = thermal activation energy for crack growth
= 31.0 kcal/mole
R = universal gas constant
= 1.103×10^{-3} kcal/mole·°R
T = absolute test temperature (°R)
T_{ref} = absolute reference temperature used to normalize data
= 617ºF (1076.67°R)
α = crack growth amplitude
K = crack tip stress intensity factor, (ksi $\sqrt{\text{in}}$)
K_{th} = crack tip stress intensity factor threshold, (ksi $\sqrt{\text{in}}$)

The above equation incorporates an activation energy-based temperature correction, similar to that described above for plant susceptibility ranking, but with a different activation energy, to normalize data obtained at different test temperatures to a single reference temperature (617ºF).

Statistical analyses of the data were performed, first by-heat, using the mean value of α for each heat of material tested (Figure 11), and then for within-heat statistical variability (Figure 12). Log-normal and log triangular fits were developed for both. The peaks of the log-triangular distributions are noted in Figures 11 and 12 (8.5 times the median for heat-to-heat, and 4.2 times the median for within-heat variability). Thus, a bad nozzle from a bad heat of material (which results when high values of the random numbers for these two variables are selected in the Monte Carlo analysis) would have a crack growth rate equal to ~36 times the median.

Finally, a correlation factor was incorporated as an input parameter in the software, to permit the user to correlate crack initiation with crack growth rate. In theory, a heat or nozzle that tends to crack or leak early in life (i.e. at the low end of the Weibull distribution of Figure 10) might be expected to have a high crack growth rate (i.e. at the high ends of Figures 11 and 12). As illustrated in Figure 13, if the user specifies a correlation factor of -1, the two are assumed to be totally correlated, and in essence, a single random number is used for selection of both parameters. If a correlation factor of 0 is input, the two are assumed totally uncorrelated, with independent random numbers selected for each. Correlation factors between 0 and 1 were evaluated in sensitivity studies, and the factor was ultimately used to calibrate the analysis with respect to observed field experience with circumferential cracking.

Effect of Inspections

The user may also specify inspections of various types and intervals. Probabilities of detection (PODs) for the inspections may be selected from built-in curves in the program, or the user may define a custom POD. In either case, the program compares the crack sizes predicted to exist in each nozzle at the time the inspection is performed, and randomly decides whether the crack is detected or not based on the POD for that crack size. If the flaw is predicted to be detected, that nozzle is assumed to be replaced or repaired, and therefore removed from the population of potential failures.

The MRPER software can simulate two types of inspections: non-destructive examinations for cracks (NDE) and visual examinations for leakage (BMV). The user can specify times of inspection, inspection coverage (in percent) and the probability of detection (POD) for each type of inspection.

Leakage Inspections

Detection of leakage depends on when the leakage starts and the amount of initial shrink fit in each nozzle. Therefore, the POD curves for leakage inspection are defined as a function of nozzle initial shrink fit. Before the start of leakage in a nozzle, leakage inspection has no effect on the results, even if all nozzles are inspected with a POD of one.

If a nozzle leak is not detected (because of POD) by the first leakage inspection after leakage is predicted to occur, it is assumed that subsequent inspections of the same nozzle may also miss the leakage, because it is obstructed or otherwise difficult to inspect. A scale factor on the POD curve during the subsequent inspection is used to simulate a reduction of the probability of detection. A scale factor of 0.2 was assumed for most analyses.

Crack inspections

When a nozzle is determined to be within the inspection coverage of a crack inspection, detection of the crack is based on the POD curve selected for that inspection. One of the built-in crack inspection POD curves in the software is illustrated in Figure 14. It corresponds to a FULLV ultrasonic angle beam examination defined in Reference [7]. Figure 14 also illustrates a comparison of that curve to performance of two NDE vendors in NDE demonstration tests on top head nozzle mockups containing fabricated defects. The bands at the bottom of the figure indicate the range of crack depths that were missed by the two vendors. The bands at the top of the chart indicate the range of crack depths that were fully detected. As expected, the POD curve transitions from very low probabilities of detection in the regime where many defects were missed, to higher PODs in the size regime where all flaws were detected. The POD curve is at about 75% at the maximum size at which flaws were missed by either vendor, and peaks at 95%, meaning that 5% of flaws are assumed to be missed no matter how large.

For crack inspections, the user also specifies an initiation time and size (a-init and t-init in Figure 15). For the circumferential crack growth analysis described above, a through-wall crack equal to 30% of the circumference is assumed at the time-to-leakage predicted for that nozzle by the Weibull distribution (t-Weibull). However, for purposes of assessing NDE detectibility, it is assumed that a part-through-wall crack of some fraction of the wall-thickness (a-init) initiates at some fraction of t-Weibull (t-init) and grows linearly in time to a/t=0.5 at t-Weibull. POD curves are then compared to the part-through-wall flaw depth predicted by this crack growth assumption at the time of inspection. Sensitivity studies of the crack initiation parameters were conducted. The analyses presented here were performed with a-init = 0.05 and t-init=0.5 (solid curve in Figure 15).

Analysis Results

A series of PFM analyses were performed using the MRPER program covering a wide variety of conditions and assumptions for the four characteristic plants discussed above. These included base cases, with and without inspections for the four plant types, and sensitivity studies to evaluate the effects of various statistical and deterministic assumptions in the analysis. The model was then benchmarked with respect to field experience with top head inspections performed to date, considering the occurrence of cracking and leakage and of circumferential cracks of various sizes. The benchmark cases were then used to select a set of analytical parameters that characterize the probability of large circumferential cracks in a reasonably conservative manner compared to field experience. Finally, the benchmarked parameters were used to analyze a set of case studies of actual plants, to evaluate the effects of various assumed inspection programs on probability of nozzle failure and leakage. A sampling of such case studies is presented in Figures 16 and 17.

Figure 16 illustrates the effect on probability of nozzle failure (Net Section Collapse, or ejection of a nozzle) of inspections of a typical set of plants operating at head temperatures ranging from 580º F to 600ºF. A no-inspection curve is shown for each temperature. Runs were then made assuming NDE inspections of the nozzles. The initial inspection times were set equal to approximately 12 EDYs, corresponding to increasing numbers of EFPYs as the assumed head temperatures decrease (see legend). Inspections were assumed to be performed on a 4 EDY interval after the initial inspections. It is seen from this figure that the assumed inspection regimen is sufficient to maintain the nozzle failure probability (per plant year) below the generally accepted target value of 1×10^{-3}.

Figure 17 illustrates results of similar analyses for probability of leakage. It is seen from this figure that the 4 EDY inspection interval maintains probability of leakage at or about 6% for the cases analyzed.

Conclusions

Extensive Probabilistic Fracture Mechanics analyses have been performed to determine the probabilities of nozzle leakage and failure in PWR top heads due to PWSCC of the Alloy 600 nickel alloy nozzle material and associated weldments. A PFM software tool was developed for this purpose, and the major computational elements and assumptions of that tool are briefly described in this paper. These include stress intensity factor computations, empirical analysis of time to leakage or cracking based on plant data, statistical analysis of PWSCC crack growth rates, and modeling of the effects of various types of inspections.

Sensitivity analyses of the various assumptions in the analyses were performed, and the PFM tool was benchmarked and calibrated with respect to plant experience. The calibrated tool was then used to evaluate various inspection regimens for PWR heads as a function of head operating temperatures and service times. A sampling of such results is presented in this paper. The probabilistic model is part of an overall MRP safety assessment of RPV head nozzle cracking and provides a useful tool to guide long term inspection recommendations and repair versus head replacement decisions.

References

1. Materials Reliability Program Probabilistic Fracture Mechanics Analysis of PWR Reactor Pressure Vessel Top Head Nozzle Cracking (MRP-105), EPRI TR-1007834; Electric Power Research Institute, Palo Alto, CA: 2004
2. T. L. Anderson, “Fracture Mechanics Fundamentals and Applications”, CRC Press, 1991
3. Dominion Engineering, Inc, “CRDM Stress Analyses”, Several Proprietary Calculation Notes, Prepared 2001 through 2003)
4. R. B. Abernathy, “The New Weibull Handbook, Reliability and Statistical Analysis for Predicting Life, Safety, Survivability, Risk, Cost and Warranty Claims,” Fourth Edition, Sept. 2000
5. “PWSCC Prediction Guidelines,” EPRI Report No. TR-104030, 1994
6. Materials Reliability Program, “Crack Growth Rates for Evaluating Primary Water Stress Corrosion Cracking (PWSCC) of Thick-Wall Alloy 600 Material,” MRP-55, Revision 1, November 2002. EPRI TR-1006695NP; Electric Power Research Institute, Palo Alto, CA:
7. Dimitrijevic, V. and Ammirato, F., “Use of Nondestructive Evaluation Data to Improve Analysis of Reactor Pressure Vessel Integrity, “ EPRI Report TR-102074, Yankee Atomic Electric Co. March 1993

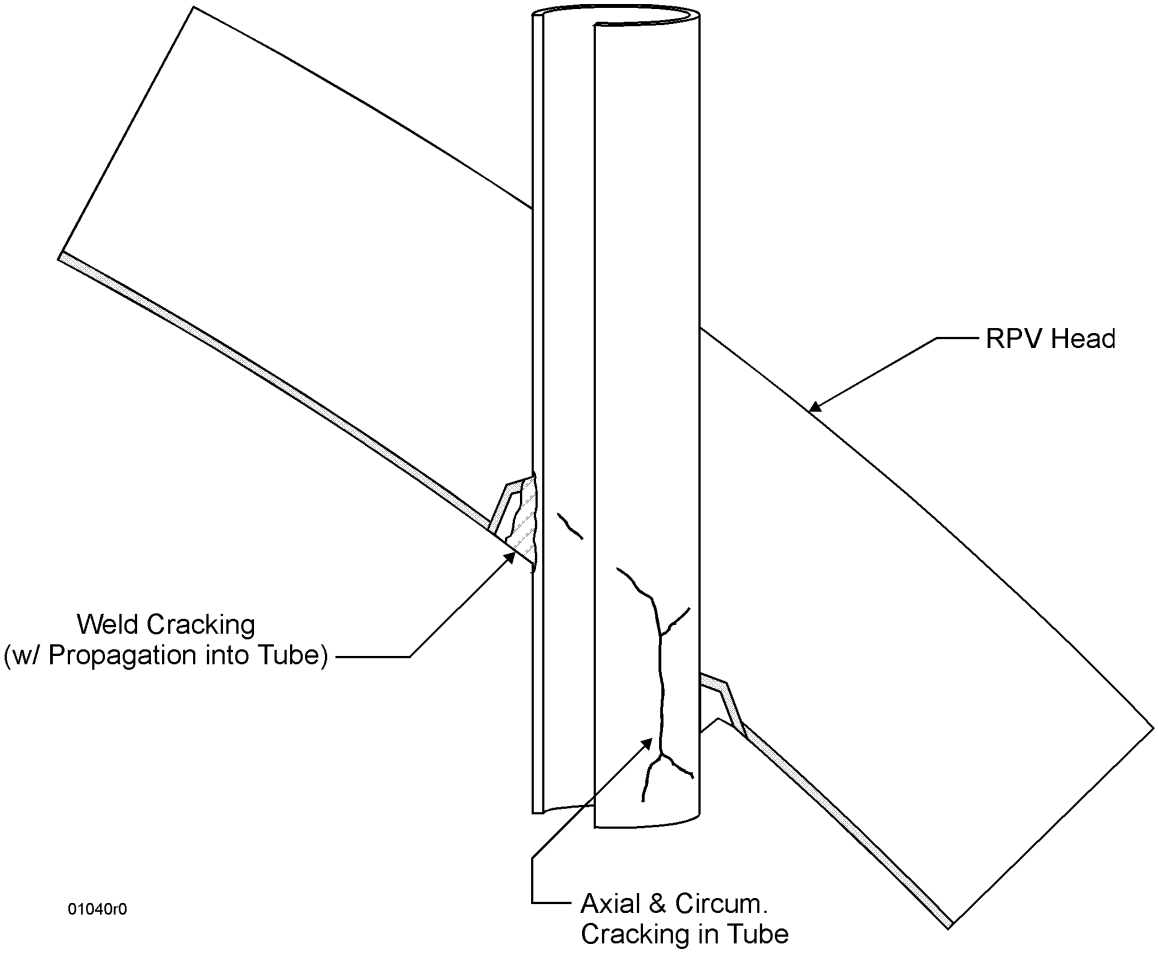

Figure 1
Schematic of RPV Top Head Nozzle Geometry and Nature of Observed Cracking

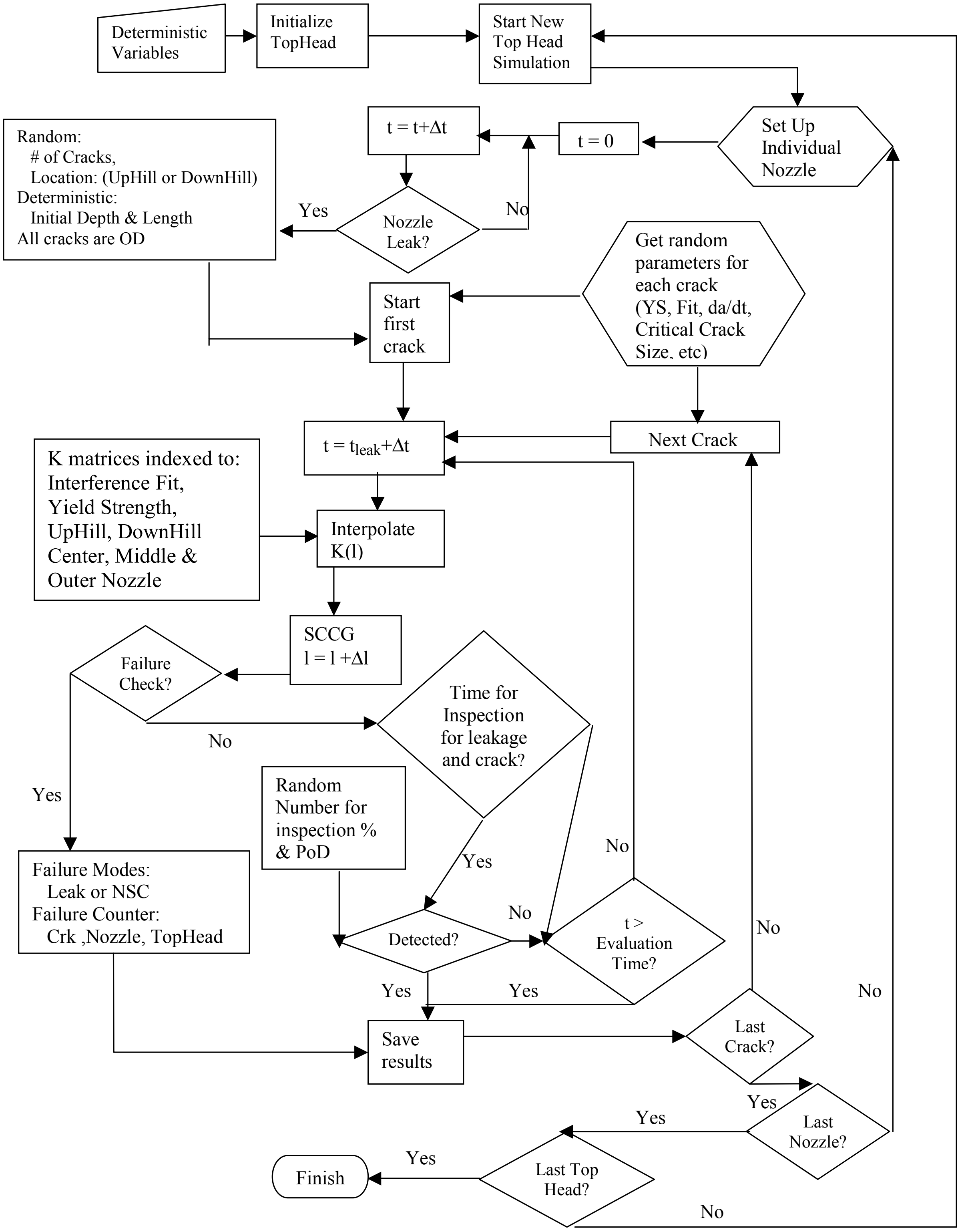

Figure 2
Flow Chart of PFM Methodology

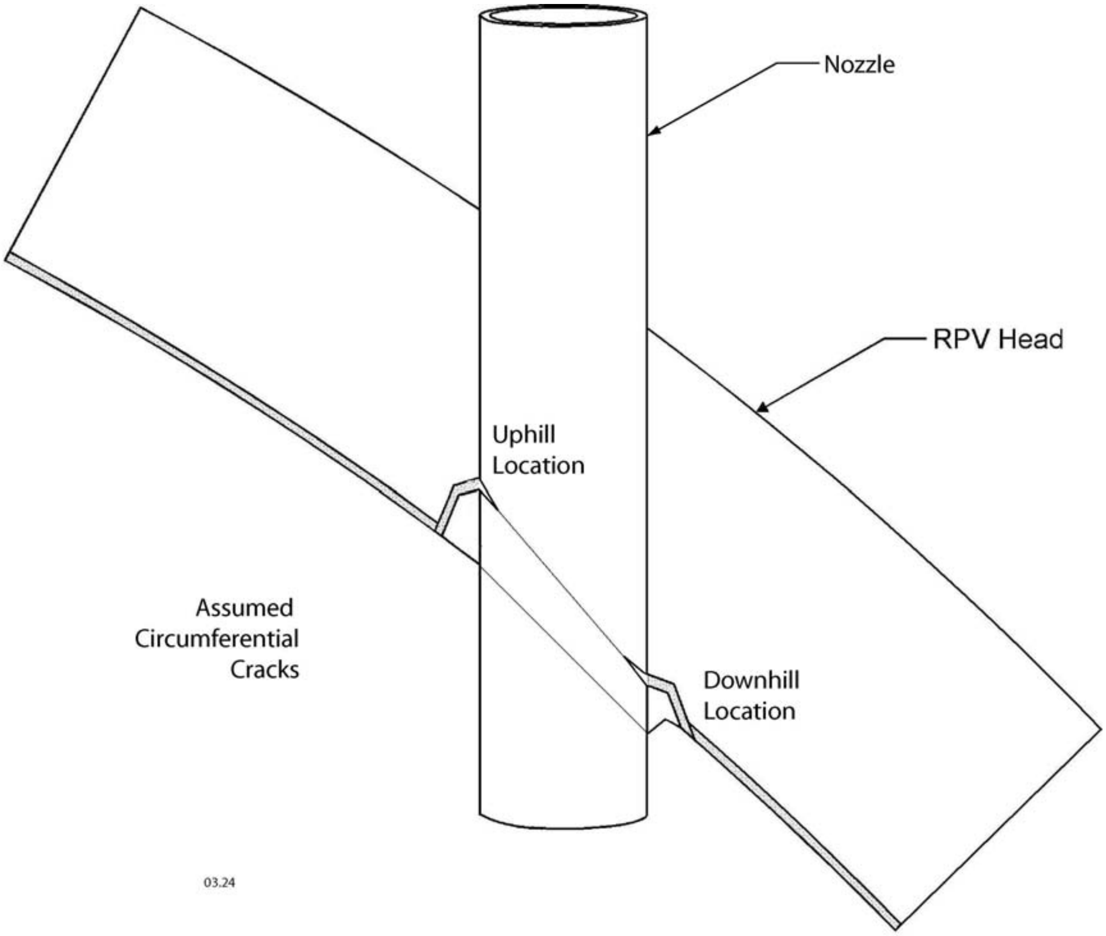

Figure 3
Schematic Illustration of Assumed Circumferential Flaws above J-Groove Welds

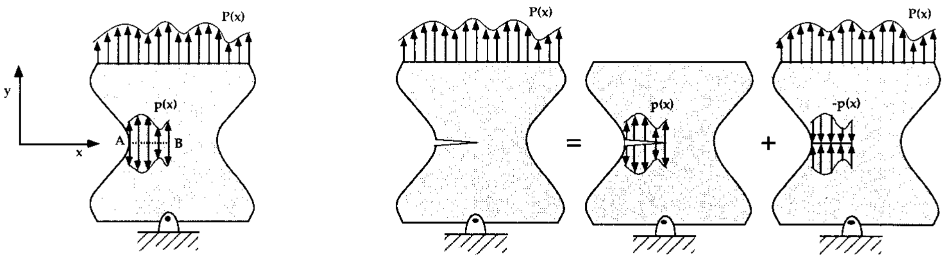

(a) (b) (c) (d)

Figure 4
Illustration of Superposition Approach for Cracks in Complex Structures Subject to Complex Loading Patterns

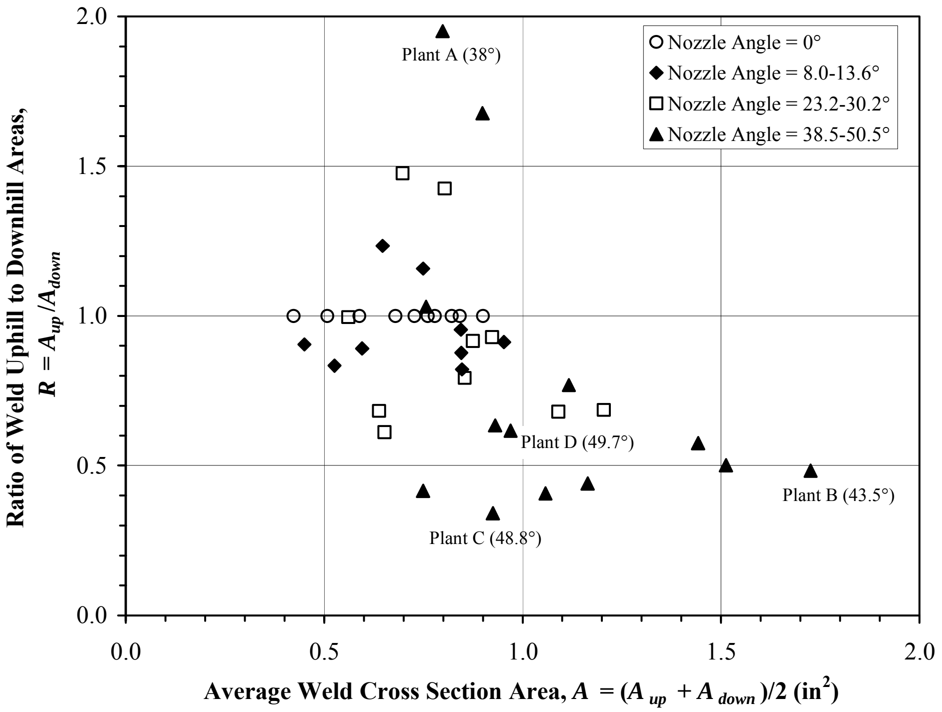

Figure 5
Comparison of Key Weld Geometry Variables Influencing Nozzle Residual Stresses – Characteristic Plants Evaluated in this Study are Labeled

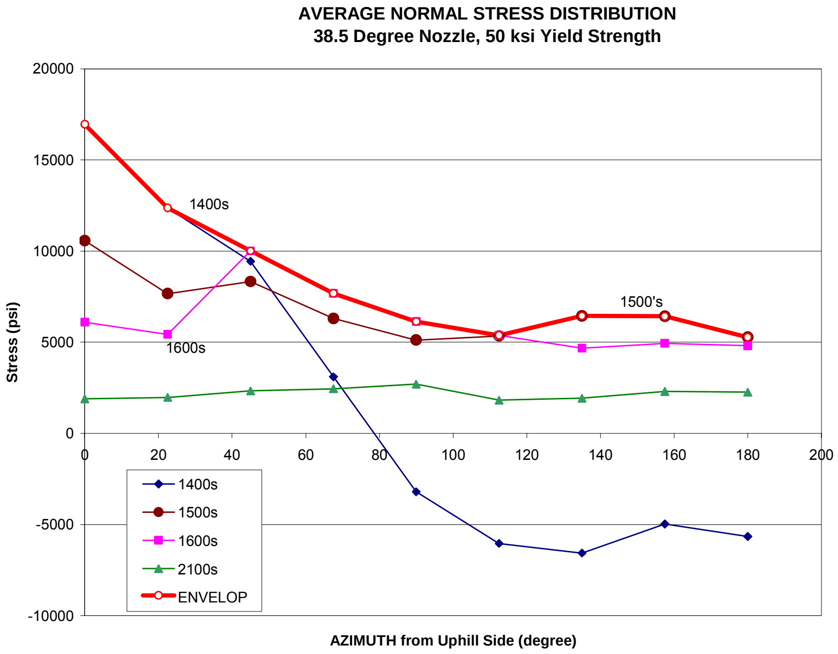

Figure 6
Through-Wall Averaged Stress Normal to Crack Surface vs. Distance from the Uphill Side of the Nozzle – Steepest Angle Nozzle – Plant A.

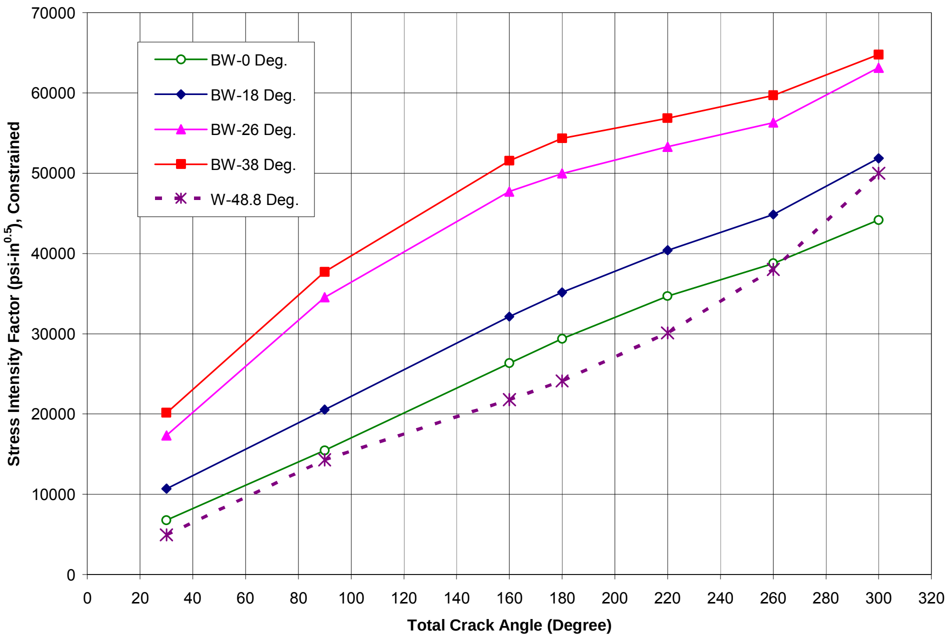

Figure 7
Stress Intensity Factor Comparison; B&W vs. W Heads; Uphill Flaws; Envelop Stress

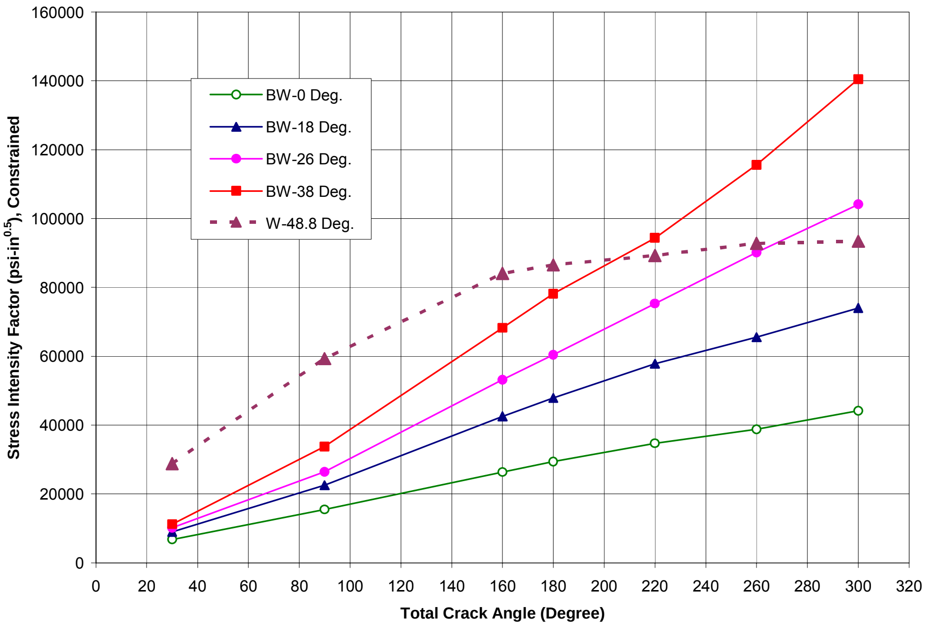

Figure 7
Stress Intensity Factor Comparison; B&W vs. W Heads; Downhill Flaws; Envelop Stress

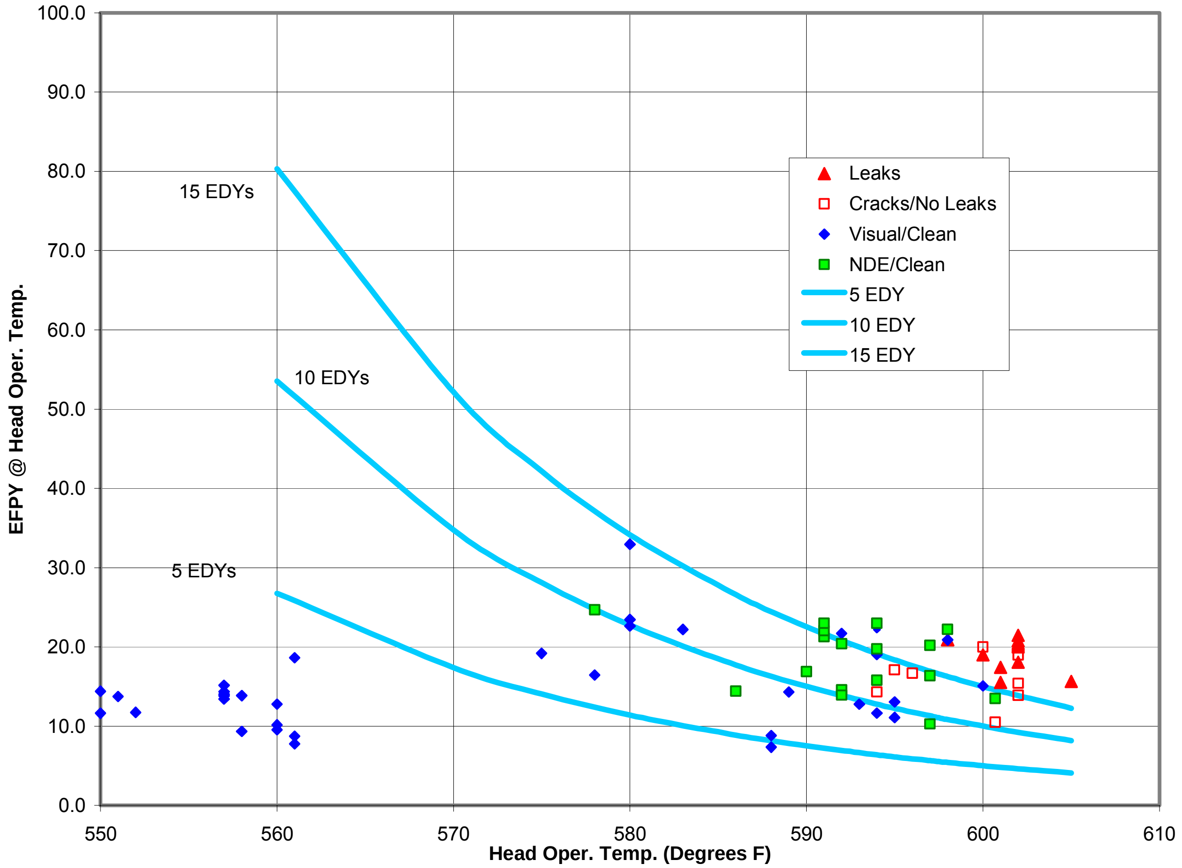

Figure 9
Summary of RPV Top Head Inspection Results in Terms of Years of Operation at Various Head Operating Temperatures. Constant EDY Curves Indicated

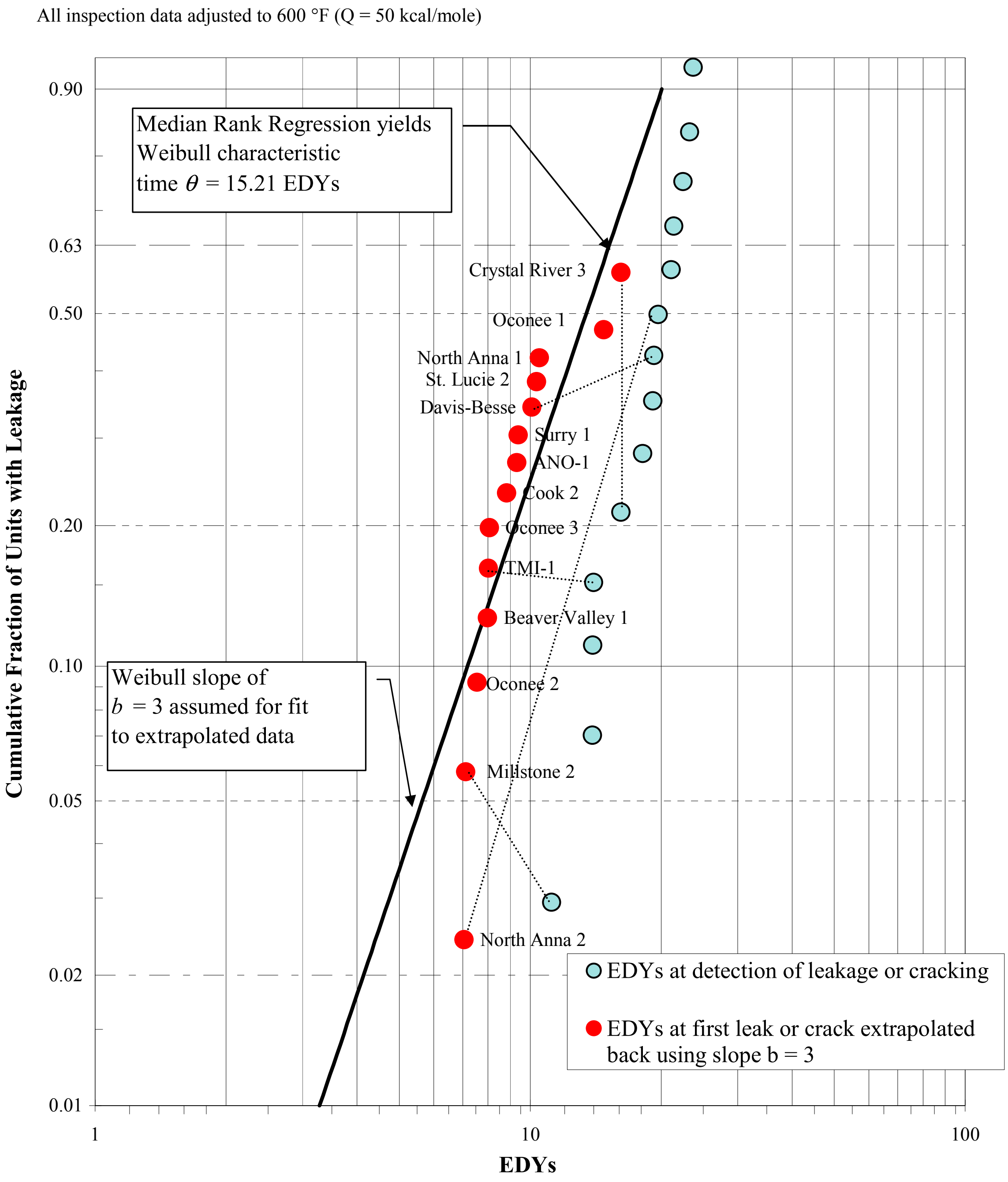

Figure 10
Weibull Plot of Plant Inspection Data Showing Extrapolation Back to Time of First Leakage or Cracking. Plants that Performed NDE and were found clean are treated as suspensions.

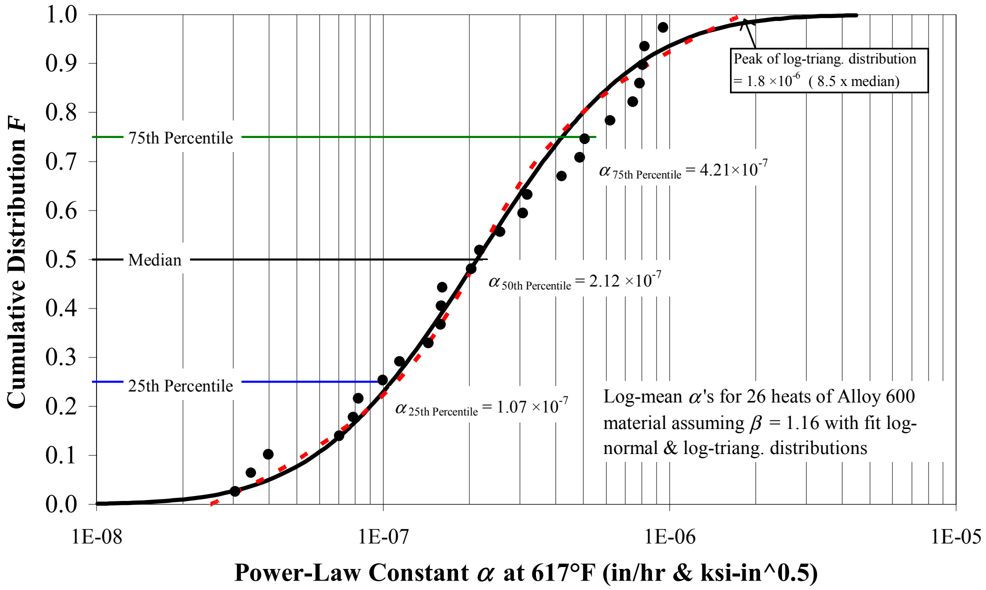

Figure 11
Distribution of Log-Mean CGR Power Law Constant for the 26 Heats of Material Reported in Ref. [11]. Log-Normal and Log-Triangular Fits to the Data also Shown

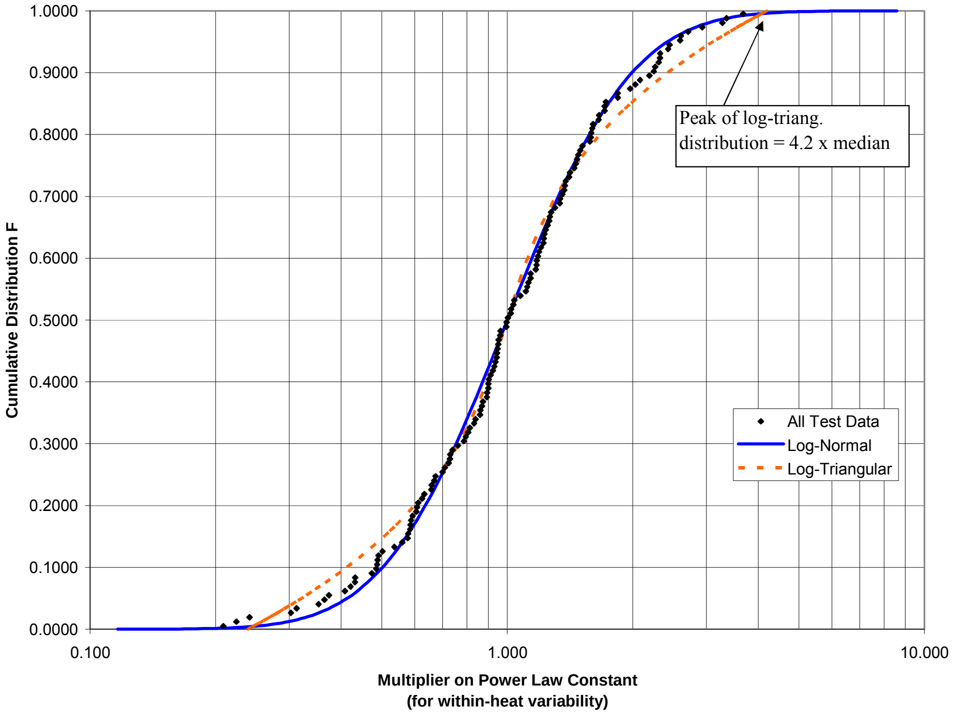

Figure 12
Distribution of 158 Individual Data Points from Ref. [11] Plotted Relative to the Means of their Respective Heats. Log-Normal and Log-Triangular Fits to the Data also Shown

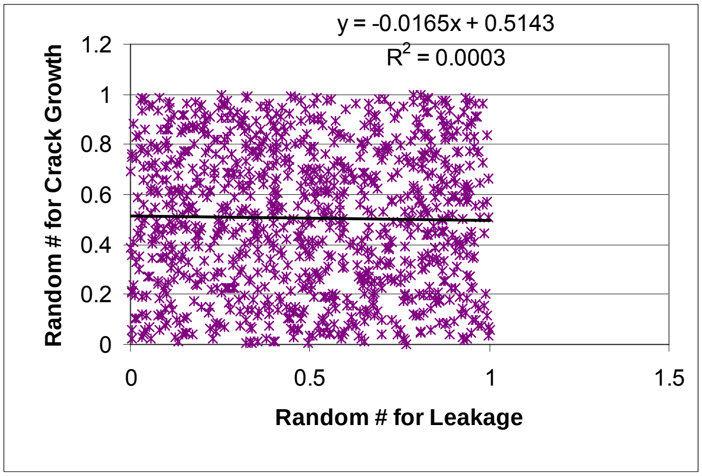

ρ = 0, uncorrelated

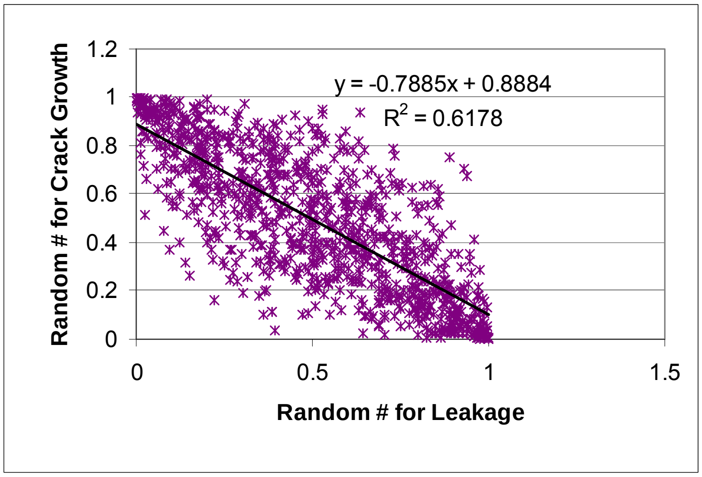

ρ = -0.8, moderate correlation

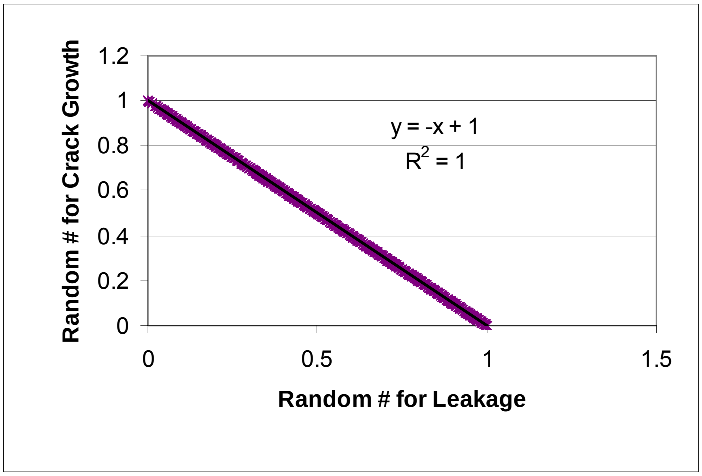

ρ = -1, totally correlated

Figure 13
Illustration of Correlation Factors for Crack Initiation and Growth

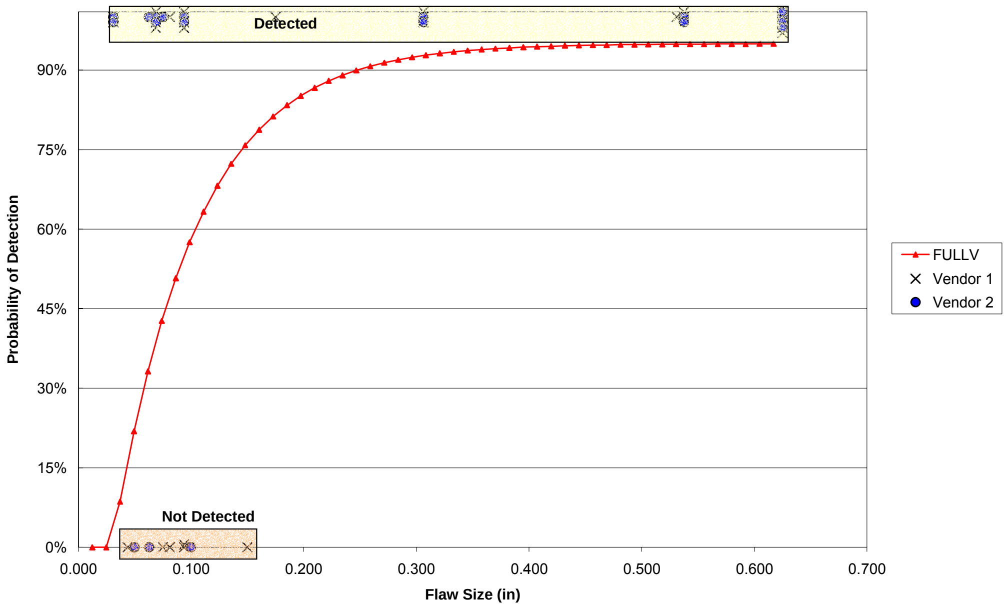

Figure 14
Illustration of Probability of Detection Curve for NDE and Comparison to Vendor Performances in Demonstration Program

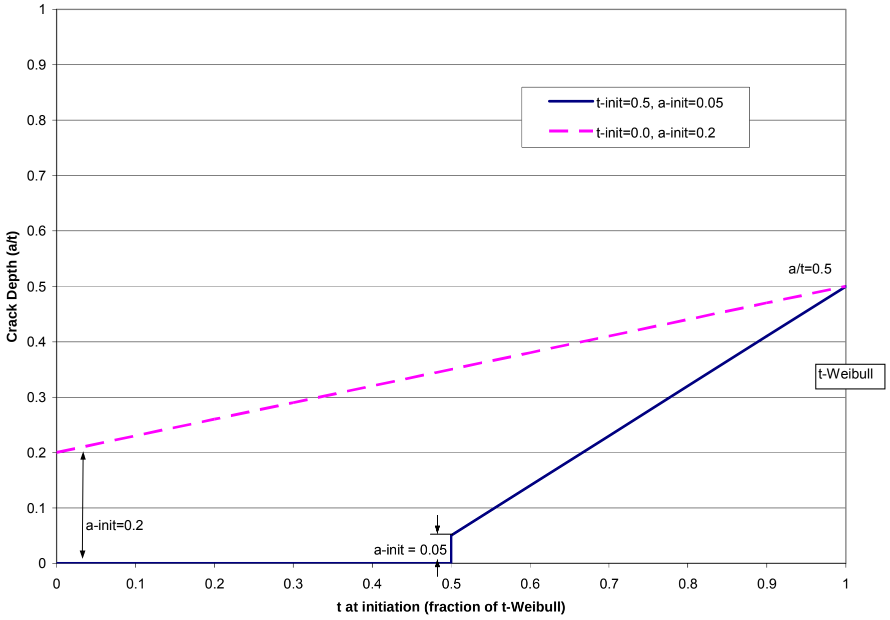

Figure 15
Illustration of Crack Initiation Time Concept for Crack Detection Prior to Leakage

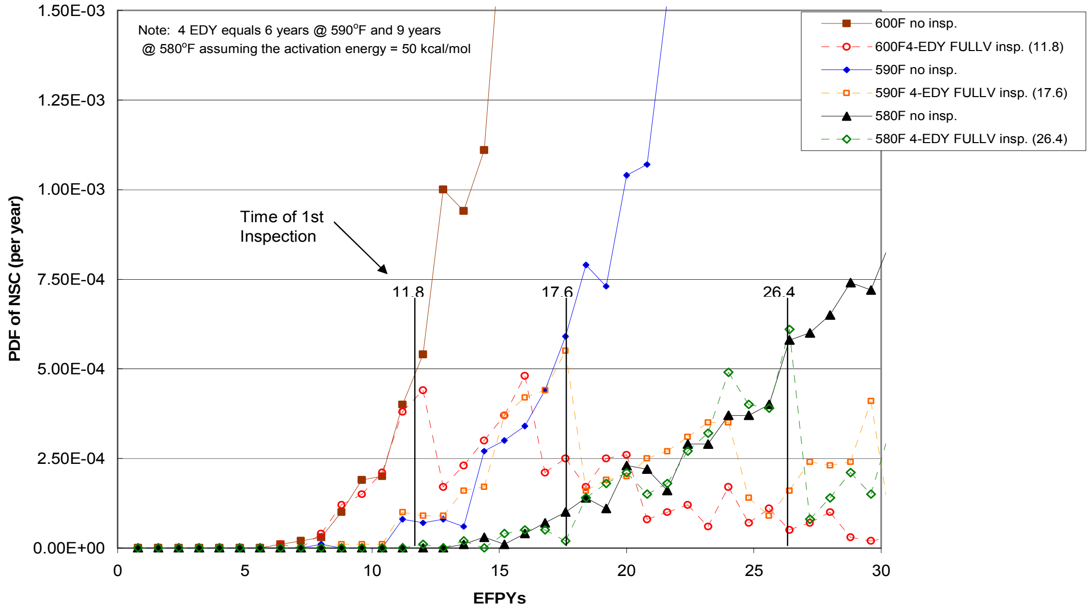

Figure 16
Probability of Nozzle Failure (NSC) as a Function of Variations in Top Head Temperature and Inspection Intervals

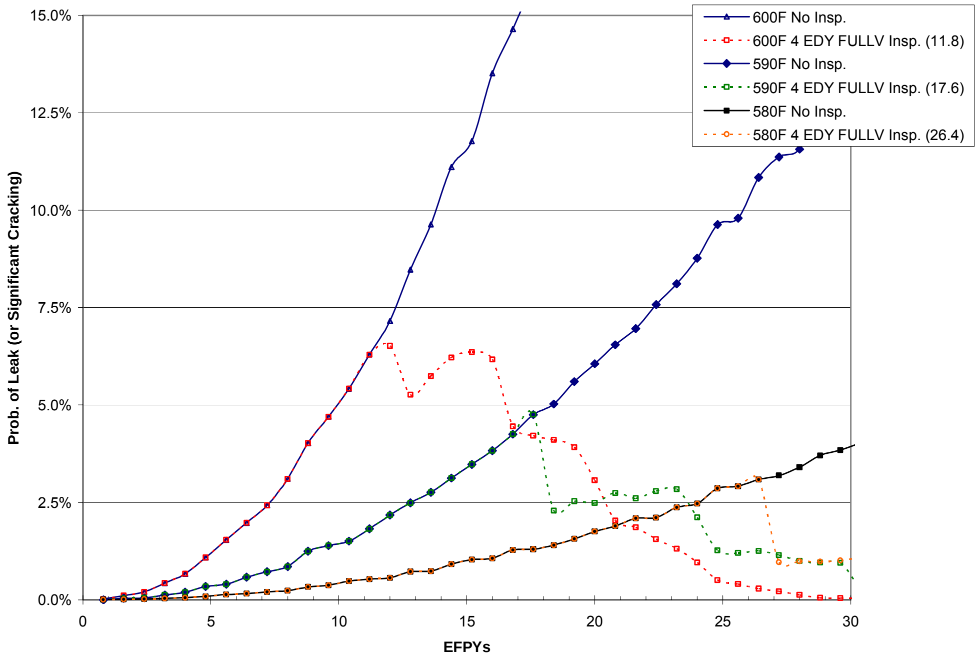

Figure 17
Probability of Nozzle Leakage as a Function of Variations in Top Head Temperature and Inspection Intervals

Parametric Studies of the Probability of Failure of CRDM Nozzles

William J. Shack
Argonne National Laboratory

Abstract

An integrated model for the probability of failure of control rod drive mechanism (CRDM) nozzles by the growth of circumferential cracks leading to net section failure is discussed. The model describes initiation in terms of Weibull probability distributions that are fit to plant data on the occurrence of leakage. Distributions of the probability of failure (ejection) of a nozzle and the probability of failure of a vessel head are computed. Sensitivity studies are used to examine the effect of some modeling assumptions. The expected numbers of leaks, large cracks, and nozzle ejections predicted by the model are compared with corresponding results for 31 operating plants. The model and data show that there is a significant plant–to–plant variability in probabilities of failure or leakage even if differences in head operating temperatures are taken into account.

Introduction

The U.S. Nuclear Regulatory Commission (USNRC) Office of Nuclear Reactor Research is sponsoring work to develop an integrated model for the degradation of CRDM nozzles and reactor heads. Such models are also being developed by the Materials Reliability Program (MRP). These models can provide input to regulatory decisions, e.g., on the degree of “credit” for lower head temperatures that can be given when inspection timing and appropriate intervals for inspection are considered.

In the model, the failure process begins with the development of a leak; the leak is associated with the formation of an initial circumferential crack on the outer diameter (OD) of the nozzle. In reality, the development of the leak and the formation of the circumferential crack probably involve initiation of multiple surface cracks. These cracks grow through the wall and circumferentially to link and form a primary crack, which continues to grow both circumferentially and through the wall. At some stage, the circumferential growth of the primary crack becomes dominant mode of crack progression rather than extension by linking and joining of surface cracks. The extent over the circumference for which it is likely that surface cracks will initiate and the rate that throughwall growth can occur can be modeled. However, at present it is assumed that once leakage to the crevice around the nozzle occurs, a throughwall circumferential crack instantaneously forms over an extent that is large enough that further growth is dominated by the circumferential growth of this crack rather than initiation, linkage, and throughwall growth of surface cracks on the OD of the nozzle. Sensitivity studies have been used to assess the impact of the assumed initial size of the throughwall crack on the results. The model can also be benchmarked by comparing the number of large cracks (165° in circumference) predicted by the model with the number of such cracks observed in service.

Initiation of primary water stress corrosion cracking (PWSCC) in Alloy 600

Following the work of Gorman, Staelhe and Stavropoulos[1] for steam generator tubes, the probability of initiating a leak is assumed to follow a Weibull probability distribution. The effect of temperature is taken into account through an activation energy.

The Weibull cumulative probability is

$$F(t) = 1 - \exp\left[-\left(\frac{x}{\theta}\right)^{b} \right], \tag{1}$$

where θ is the time at which the cumulative probability of a leak is 0.63, and b is the Weibull slope. The Weibull slope b characterizes the rate at which the chance of failure is increasing with time (b = 1 gives a constant failure rate). Ideally, b would be determined from the analysis of failure fractions at different times. Because such data are very limited, most calculations have used a value of 3, which is reasonably consistent with available PWSCC initiation data (primarily obtained in tests on steam generator tubing). The limited data for repeated inspections of CRDM nozzles that are currently available suggest that a higher value of b may be appropriate, and some analyses have been performed with b = 4–6. However, for predicting first failures, a lower value of b is more conservative and b = 3 is used for the calculations presented here.

Estimates of population bounds on the Weibull scale factor θ

The Weibull scale factor θ is approximately the median time for a nozzle to initiate a leak. It is expected to be a strong function of the material microstructure, but will also vary with fabrication procedures such as machining and welding. The range of behavior is described by a distribution of the scale factor, p(θ). The likelihood of the observed numbers of leaking nozzles can be described in terms of a function L:

$$L = \prod_{i=1}^{N} \int_0^{\infty} p(\theta) \frac{N_i!}{n_{f_i}!(N_i - n_{f_i})!} \left\{ W(t_i,\theta)^{n_{f_i}} \left(1 - W(t_i,\theta)\right)^{(N_i - n_{f_i})} \right\} d\theta \tag{2}$$

where $W(t_i,\theta)$ is the Weibull cumulative function for time t_i and shape parameter θ, n_{f_i} is the number of leaking nozzles for plant i, N_i is the total number of nozzles for plant i, and N is the total of number of plants considered. The likelihood function is just the usual binomial probability for n_{f_i} items out of a collection of N_i items averaged over all values of θ.

The distribution p(θ) was determined by maximizing L for the inspection data shown in Table 1. Triangular, log-triangular, Weibull, and lognormal distributions for p(θ) were considered. The integrals were evaluated numerically and the distribution parameters varied to find the maximized solution. The log-triangular distributions gave the best fit.

Table 1 Inspection data for plants with qualified visual and volumetric inspections by March 2003.[*]

Plant	Head Temp °F	EFPYs[a]	EDYs[b]	Nozzles	Leaks/Cracks
ANO 1	602	19.5	19.6	69	8
ANO-2	590	16.8	11.2	81	0
Beaver Valley 1	595	17.2	14.0	65	4
Calvert Cliffs 2	593.7	20.4	15.8	65	0
Cook 1	580	24.8	10.0	79	0
Cook 2	600.7	13.5	13.9	78	0
Crystal River 3	601	15.5	16.2	69	1
Davis-Besse	605	15.7	19.2	69	5
Farley 1	596.5	20.2	17.5	69	0
Farley 2	596.9	17.9	15.8	69	0
Indian Point 2	585.5	14.4	8.0	97	0
Indian Point 3	593.5	20.5	15.7	78	0
Millstone 2	593.9	14.3	11.2	69	3
North Anna 1	600.1	19.9	20.0	65	0
North Anna 2	600.1	19.9	19.0	65	14
Oconee 1	602	20.2	21.9	69	3
Oconee 2	602	21.9	23.7	69	19
Oconee 3	602	20.0	21.7	69	14
Palo Verde 1	592	14.6	10.6	97	0
Palo Verde 2	591.7	14.0	10.0	97	0
Point Beach 1	591.6	20.4	14.5	49	0
Robinson 2	598	22.0	20.3	69	0
San Onofre 2	590.5	22.5	15.3	91	0
San Onofre 3	590.6	22.4	15.3	91	0
Sequoyah 1	580	5.0	1.5	78	0
St. Lucie 1	590.6	23.1	15.7	77	0
St. Lucie 2	595.6	16.7	13.9	91	1
Surry 1	597.8	20.9	19.1	65	6
TMI 1	601	17.4	18.2	69	6
Turkey Point 3	594.4	23.0	18.3	65	0

[a] Effective full power years of operation at the actual operating temperature

[b] Effective degradation years. Equivalent number of operating years at 600°F (315°C)

---

[*] Personal Communication, P. Riccardella, Structural Integrity Associates, to W. J. Shack, May 30, 2003.

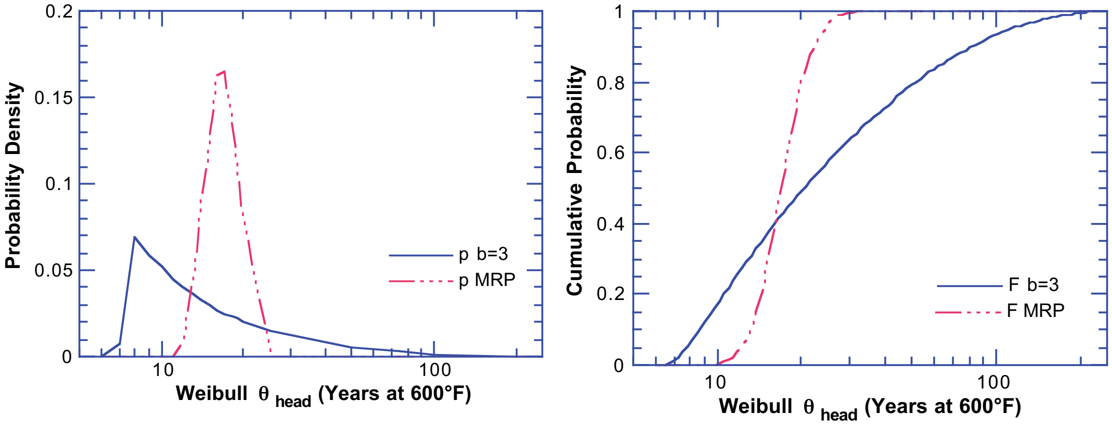

(a) (b)

Figure 1. (a) Probability density functions for the Weibull scale factor for a reactor vessel head with 69 nozzles; (b) Cumulative probability functions for the Weibull scale factor for a reactor vessel head with 69 nozzles. The solid curves are those obtained by maximizing the likelihood L [Eqn (2)]; the chain curve is based on results presented at the public meeting with the MRP on June 12, 2003. For Weibull distributions $\theta_{head} = \theta_{nozzle} / n^{1/b}$ where n is the number of nozzles.

The resulting density and cumulative distributions are shown in Fig.1 along with distributions based on results presented in a public meeting with the MRP on June 12, 2003. The Maximum Likelihood Estimate (MLE) is much broader than the MRP distribution, but the two distributions represent different things. The MLE attempts to represent the entire range of behavior exhibited by the Alloy 600 nozzles in service. The MRP distribution represents an estimate of an "average" value and the uncertainty on that estimate.

The value of upper end of the MLE can be varied significantly with little effect on the value of likelihood. This is physically reasonable. The available operating experience (≈ 20 EDY) provides information about the most susceptible nozzles/heads, but less susceptible materials would have little effect on the operating experience to date. A sensitivity calculation was done to determine a distribution with the same lower bound value as the MLE, but with the other values adjusted to give a likelihood equal to 1/2 the peak value. The resulting distribution is compared with the MLE in Fig. 2.

In the plants in Table 1, 84 leaks and large cracks were observed. For a plant population with the same operating times, temperatures, and number of nozzles as the plants in Table 1, the expected number of leaks are given in Table 2. The industry distribution is not representative of the population (it gives the number of leaks expected if we had 31 plants with the same operating times and temperatures as the plants in Table 1, but with nozzle properties equal to the average of the distribution). The MLE distributions also give values somewhat lower than expected, although not completely unlikely in statistical terms. There are three problems with the approach shown in Eq. (2): it does not account for fact that most heads have more than one heat of material; it represents the average likelihood for a plant with nozzles from the distribution p(θ) rather than a specific value from the distribution; and it is based on

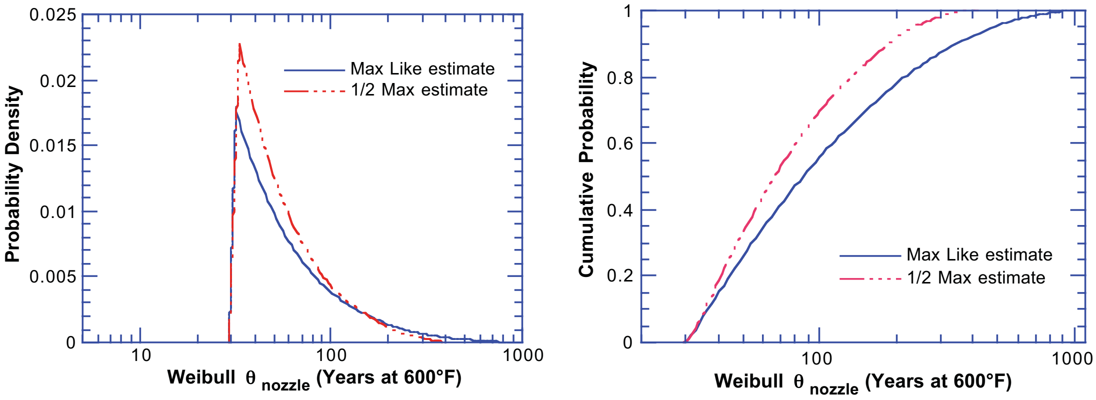

(a) (b)

Figure 2. Comparison of the probability density functions (a) and cumulative probability functions (b) for the Maximum Likelihood Estimate and a sensitivity calculation for the case where the upper end of the distribution has been varied to get an estimate that is one half the value of the maximum.

Table 2 Expected number of leaks in a population with operating times and temperatures as given in Table 1 for different distributions of the Weibull scale factor θ.

Weibull scale factor distribution	Expected number of leaks in population
Maximum Likelihood Estimate	55.3 ± 15.3
1/2 Maximum Estimate	69.7 ± 15.7
MRP 6-03	25.6 ± 2.5

an assumed form of the distribution. Additional work is being done using a Bayesian approach that can avoid some of these limitations, but the calculations in this paper are based on the distributions obtained from Eq. (2).

Crack Growth Rates in Alloy 600 Nozzles

As noted previously, it is assumed that the failure of a nozzle is governed by the circumferential growth of throughwall cracks. Crack growth rates (CGRs) in Alloy 600 are strongly heat dependent. As in the case of crack initiation, this has been associated with different microstructures, but quantitative correlation with microstructural features is difficult, and the relevant microstructural information is not available for most heats in service.

Data on the CGR of Alloy 600 materials relevant to CRDM nozzles (i.e. not SG tubes) have been collected and analyzed in the report Reference 2. The data were fit by heat to a correlation for the CGR $\dot{a}$ of the form

$$\dot{a} = A(K-9)^{1.16} \tag{3}$$

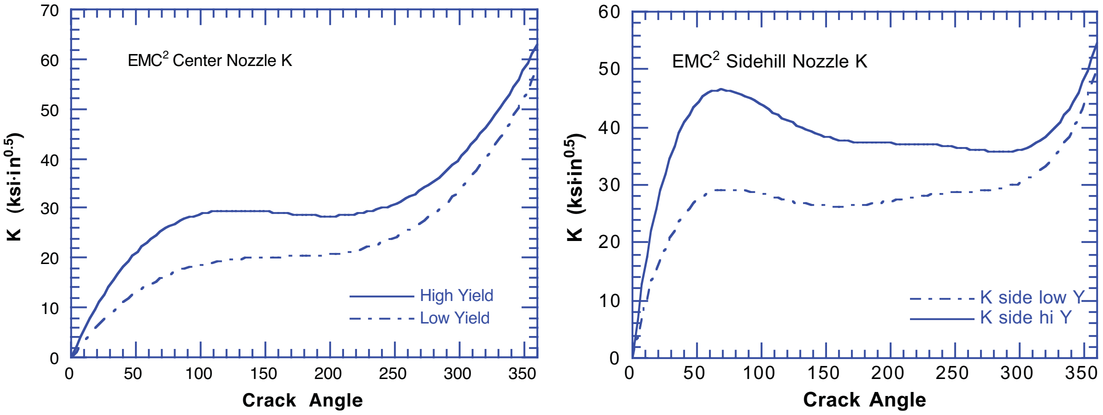

(a) (b)

Figure 3. EMC^2 Stress intensity factor K solutions for (a) center nozzles and for (b) sidehill nozzles.

clear that the values of θ and A should be correlated, few data are available on which to quantitatively base such a correlation, and it appears necessary to use engineering judgment to develop a correlation.

For the present calculations, a variety of uniform distributions have been considered. The leftmost uniform "window" in Fig. 4b appears to be clearly conservative. All the values below the correlated value are cut off, but all the values higher than the correlated value are included with uniform likelihood. The other uniform distributions are centered on the correlated value, but cut off portions of the distribution above and below the correlated value. Windows of width 0.2, and 0.5 are assumed to bound the range of widths that might be expected. The narrower window corresponds to a rationale that the primary reason for variability in initiation is variation in material microstructure. In this case, one would expect a strong correlation between susceptibility to initiation and high CGR, i.e., a narrow window. If, however, fabrication variables such as surface cold work or weld defect structure are important in increasing susceptibility to early initiation, then one might choose the wider window, since these would be less likely to have an effect on the throughwall CGR.

Probability of leakage for a vessel head

The probability of leakage from the head is computed from the probability of leakage for a nozzle. If all nozzles have the same susceptibility to leakage this is just

$$P_{leak} = 1 - (1 - P_{nozzle})^{N} \tag{4}$$

Most plants, however, appear to have multiple heats of material for nozzles. In this case Eq. (4) becomes:

$$P_{leak} = 1 - \prod_{k=1}^{K} (1 - P_{nozzle_k})^{n_k} \tag{5}$$

proposed by Scott[3] where K the stress intensity is in MPa·m$^{1/2}$ and $\dot{a}$ is in m/s. The correlation predicts a "threshold" at K = 9 MPa·m$^{1/2}$, which implies that until a crack is large enough that K is significantly larger than 9 MPa·m$^{1/2}$, the circumferential growth of a crack may not dominate crack extension. Values of the parameter A in the Scott correlation were determined for each of the 23 heats of Alloy 600 nozzle material for which CGR data are available. The values of A in the population of heats in service were assumed to be represented by a log–normal distribution fit to the available sample of 23 heats. The CGR data were normalized to a temperature of 325°C (617°F) using an activation energy for crack growth of 130 kJ/mol (31.0 kcal/mol). The log–mean of the log–normal distribution is –27.34 and the log–standard deviation is 1.02 (with the CGR in units of m/s and K in MPa·m$^{1/2}$). For the case of throughwall cracking in the CRDM, the CGRs are doubled to account for the possibility of a more aggressive chemistry in the crevice region between the nozzle and the low–alloy steel vessel.

Because the infinite tails of the log–normal distribution are unrealistic, a log–trianglar distribution has been used for the both the integrated model developed by the MRP and the studies presented here. Except at the tails of the distributions, the log–normal and log–triangle distributions are almost indistinguishable.

The value of A varies by about a factor of 100 over the entire population of materials. At 316°C (600°F) for a typical K value of 27.5 MPa·m$^{1/2}$ (25 ksi), $\dot{a}$ = 18 mm/y (0.7 in./y) for the worst heat.

Stress Intensity Factor Distributions

Calculations of the probability of failure of a CRDM nozzle require knowledge of the stress intensity factor associated with the nozzle. Until a crack becomes large (> 180°), K is dominated by the residual stresses due to welding, and the axial load on the nozzle due to the pressure load is relatively unimportant. For larger cracks the pressure loads become more important and dominate as the crack approaches failure (≈330°). Because the residual stresses due to welding vary with the yield stress of the material, K is also expected to vary with yield stress.

K values for circumferential cracks depend on the geometry of the nozzle (centerline or sidehill) and the yield stress. K solutions have been developed by Engineering Mechanics Corporation of Columbus (EMC^2) under NRC sponsorship. The solutions as functions of the extent of a throughwall crack are shown in Fig. 3. The EMC^2 high yield stress solutions correspond to a yield stress of 443 MPa (64.4 ksi) and the low yield stress solutions correspond to a yield stress of 258 MPa (37.5 ksi). K solutions for intermediate yield stresses are approximated by linear interpolation between the two solutions. We can define a random variable α, which can be used to describe the variability in K, $K = \alpha K_{low} + (1-\alpha)K_{high}$.

Although both the Weibull initiation parameter θ and the CGR A are statistically distributed, they are not independent variables. The metallurgical factors that make a heat of Alloy 600 susceptible to the initiation of cracking also appear to result in high CGRs once a crack has initiated. One way to visualize the correlation is in terms of a "window" that for a particular value of the initiation parameter θ defines the distribution of the CGR parameter A that is associated with θ. Low values of θ (short times, high susceptibility to initiation) are correlated with high values of A (high CGRs). Some potential correlation "windows" for values of A corresponding to a particular value of θ are shown in Fig. 4b. Although it is

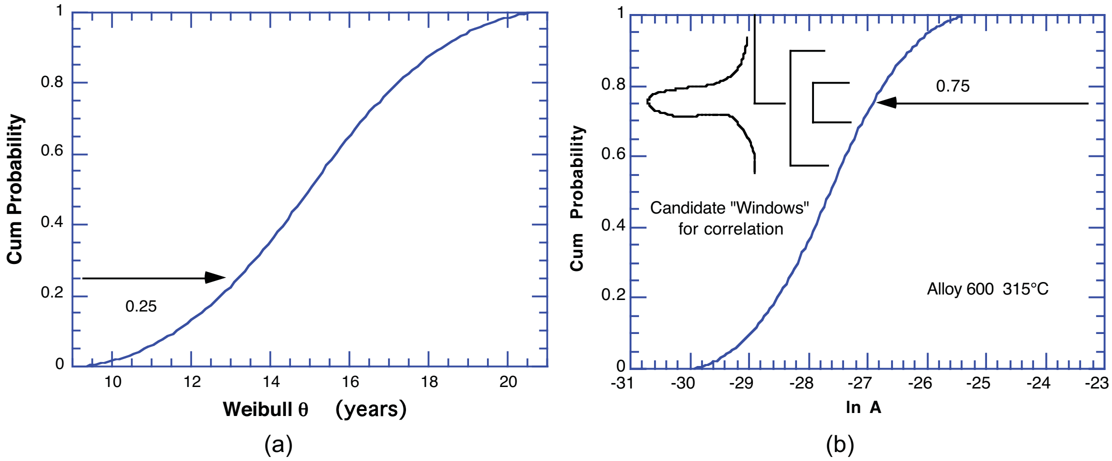

(a) (b)

Figure 4. (a) Representative distribution for the Weibull parameter θ describing initiation of leakage; (b) Candidate "windows" representing the values of A associated with a value of θ.

where K is the total number of heats in the head, n_k is the number of nozzles from heat k, and P_{nozzle_k} is the probability of leakage for a nozzle from heat k.

Table 3 shows the numbers of nozzles per heat from different heats for heads in B&W plants. The number of nozzles per heat is distributed approximately lognormally as shown in Fig. 5a. Such data does not appear to be readily available for other manufacturers. The B&W results have been assumed to be typical and used for the computation of the properties of heads with multiple heats.

Table 3 Number of CRDM nozzles from different heats for B&W reactors

ONS–1	ONS–2	ONS–3	ANO–1	Davis Bessie	TMI–1	CR–3
50	2	1	2	32	11	69
1	4	68	21	5	54	
15	27		7	23	1	
	15		36	9	2	
	7		1			
	12		2			
	2					

Vessel head calculations were done assuming that the head contains from 1 to 7 heats of material and that the number of nozzles per heat was given by the distribution shown in Fig. 5a. The resulting probability of leakage for the head as a function of operating time is shown in Fig. 5b.

The results suggest a high probability of leakage for most plants after 10-15 effective degradation years (EDY)—operating time in years at 600°F (316°C), although there is significant plant–to–variability

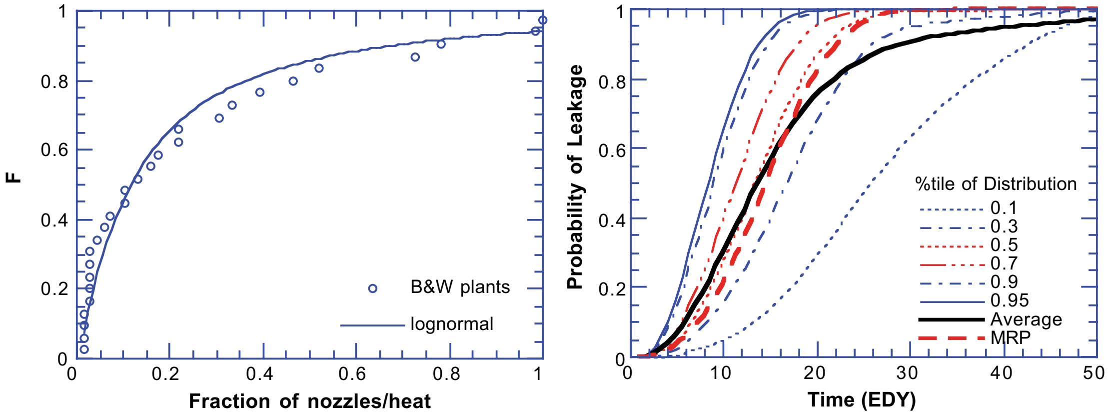

(a) (b)

Figure 5. (a) Cumulative distribution of the fraction of nozzles from a heat for B&W reactors; (b) Cumulative distribution of the probability of leakage of reactor vessel heads as a function of operating time at 600°F (316°C) [effective degradation years (EDY)].

in the probability of leakage. The Weibull scale factor from the MRP 6-03 presentation gives leakage probabilities that are fairly close to the average values for the distribution.

Probability of failure of a nozzle

The probability that a CRDM nozzle will fail, i.e., that a nozzle will fail from growth of a circumferential crack, at a time t_f less than T, $P(t_f < T)$, can be calculated from

$$P(t_f < T) = \int_0^T p(t) P_c(t_f < T - t) dt \tag{6}$$

where p(t) is the probability that a crack will initiate at a time t, and $P_c(t_f < T–t)$ is the conditional probability that a crack which initiates at t will fail at a time t_f less than T. $P_c(t_f < T–t)$ is determined by fracture mechanics analysis. Because it is assumed that a circumferential crack forms immediately on the occurrence of a leak, the probability p(t) is equal to the probability of leakage times the fraction of the leaks that are associated with circumferential cracks. This fraction has been taken as 0.2 in the current calculations, based on the available inspection data. For a given choice of the Weibull scale factor [which determines p(t)] and the yield stress parameter α [which determines the stress intensity distribution and together with the MRP-55 CGR distribution determines $P_c(t_f < T)$], Eq. (6) gives a probability of failure for a nozzle. Monte Carlo sampling from the distribution for the scale factor and from the distribution for α gives the distribution for the probability of failure of a nozzle.

Distributions of the probability of failure for a 600° F (316°C) operating temperature are shown in Fig. 6a for a center nozzle and in Fig. 6b for a sidehill nozzle. The probability of failure for a sidehill nozzle is higher than for center nozzles because of the higher K values, but there is overlap in the distributions. The correlation window for the CGR used for the calculations in Fig. 6 is a presumably

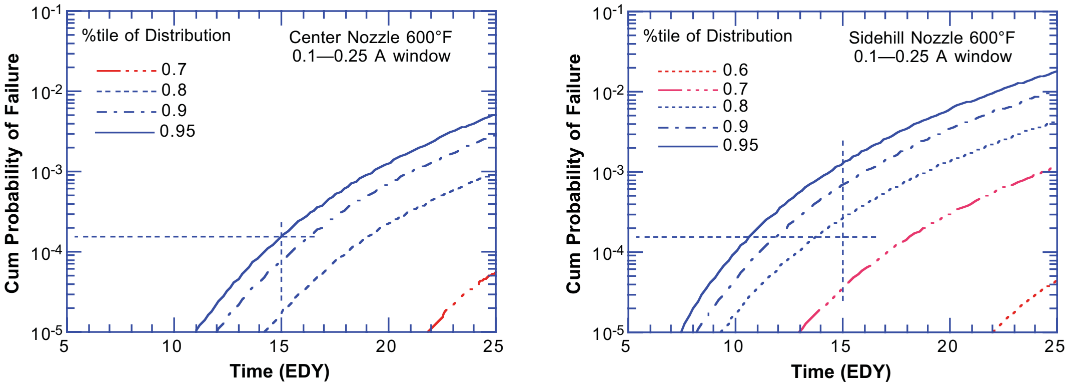

(a) (b)

Figure 6. Probability of failure of (a) center nozzles and (b) sidehill nozzles as a function of operating time at 600°F (316°C). The dotted straight lines in the figures are intended only to facilitate comparison of the figures.

conservative choice where the CGR population sampled from 0.1 below the correlation value for the Weibull scale factor for initiation to 0.25 above that value, i.e., the sample is conservatively biased.

Estimates of the probability of failure of a head

Equation (6) gives the probability of failure for a single nozzle. If all nozzles are from one heat of material then the probability of failure for the head can be easily calculated from the probability of failure of the nozzles

$$P_{f\text{–}head} = 1\text{-}(1\text{-}\ P_{f\text{–}nozzle\text{–}c})^{N_c}\ (1\text{-}P_{f\text{–}nozzle\text{–}s})^{N_s} \qquad (7)$$

where N_c and N_s are the number of center and sidehill nozzles, respectively, and $P_{f\text{–}nozzle\text{–}c}$ and $P_{f\text{–}nozzle\text{–}s}$ are the probability of failure of center and sidehill nozzles, respectively. For multiple heats this can be generalized to

$$P_{f-head} = 1 - \prod_{K=1}^{K} (1 - P_{f-nozzle-c_k})^{N_{c_k}})(1 - P_{f-nozzle-s_k})^{N_{s_k}} \qquad (8)$$

where N_{c_k} and N_{s_k} are the number of center and sidehill nozzles from heat k, respectively, and $P_{f-nozzle-c_k}$ and $P_{f-nozzle-s_k}$ are the probability of failure of center and sidehill nozzles from heat k, respectively.

The probability of failure for the heads is determined by Monte Carlo calculations sampling from the distribution for the number of nozzles per heat and then from the distributions for the probability of failure of center and sidehill nozzles for each of the heats. The number of heats of material and the numbers of nozzles in each heat are assumed to be distributed as shown in Fig. 5a, based on the data for

B&W plants. Because the sidehill solutions are for the bounding angle and are conservative for nozzles with smaller sidehill angles, in the calculations the sidehill region is split into three zones with different average sidehill angles. Interpolation between the probability of failure for the center and sidehill nozzles is used to get approximate values of the probability of failure for the nozzles in the two sidehill zones with smaller sidehill angles.

Results for vessel heads operating at 600°F (316°C) are shown in Fig. 7. Figures 7a, b, and c show the effect of changing the window used to describe the correlation between the CGR and the Weibull scale factor for initiation. The author considers the broader window used for Fig. 7b to be the "best estimate."

Figure 8 compare the results using the maximum likelihood estimate for the distribution of the scale factor (Fig. 8a) and the more conservative 1/2 maximum likelihood distribution (Fig. 8b). The differences are relatively small.

Figure 9 shows the effect of temperature on the probability of failure. Decreasing the temperature does decrease the probability of failure significantly, but there is overlap in the distributions. The 95 percentile at 590°F (310°C) is comparable to the average probability of failure at 600°F (316°C).

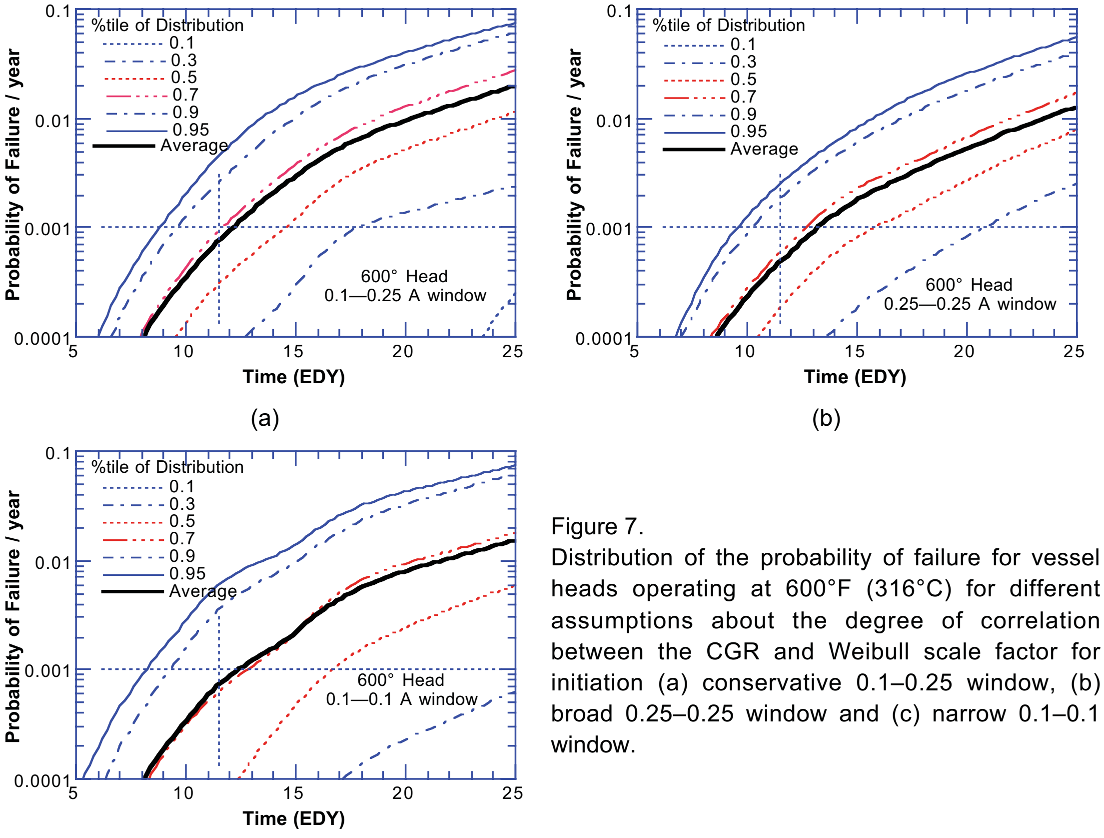

(a)

(b)

Figure 7.
Distribution of the probability of failure for vessel heads operating at 600°F (316°C) for different assumptions about the degree of correlation between the CGR and Weibull scale factor for initiation (a) conservative 0.1–0.25 window, (b) broad 0.25–0.25 window and (c) narrow 0.1–0.1 window.

(c)

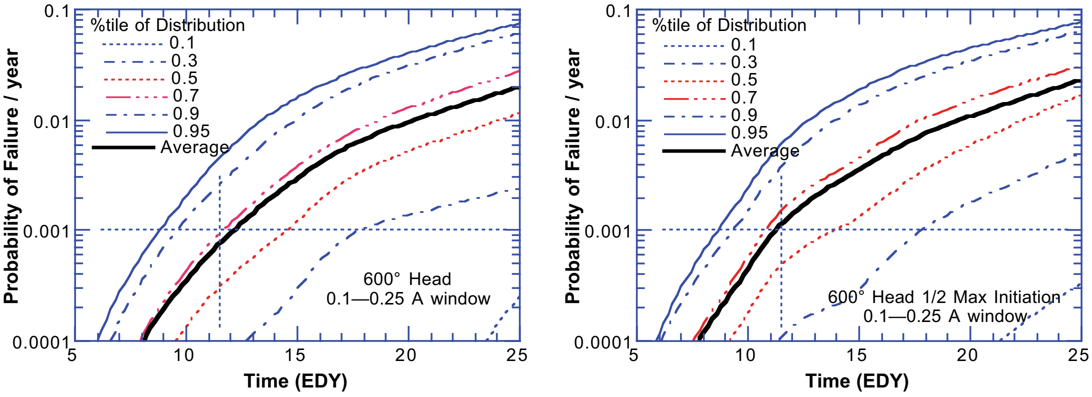

(a) (b)

Figure 8. Distribution of the probability of failure for vessel heads operating at 600°F (316°C) for (a) the maximum likelihood estimate for the Weibull scale factor θ and (b) the more conservative 1/2 maximum likelihood estimate for θ.

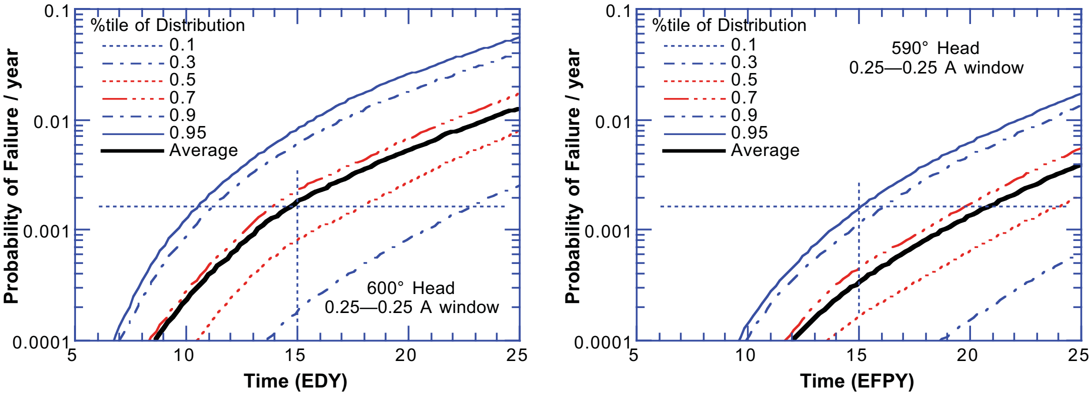

(a) (b)

Figure 9. Distribution of the probability of failure for vessel heads operating at (a) 600°F (316°C) and (b) 590°F (310°C).

The distributions of the probability of failure presented in Figs. 6, 7, 8, and 9 can be interpreted as describing the range of behavior expected in the whole population of nozzles or heads or as the uncertainty in the prediction of the failure of a specific nozzle or head assuming that we know only its operating temperature and the number of years of operation. The distributions are broad, spanning about 3 orders of magnitude at any given time. The results are believed to be conservative — e.g., the true 95th percentile of probability of failure is lower than the estimates presented here.

In practice, for the analysis of a specific plant, we would expect to have additional knowledge, e.g., the plant has operated n years without nozzle leaks or that it had m leaks after n years of operation. This information can be used to update the Weibull scale factor distribution shown in Fig. 2, which was developed to describe the range of behavior possible in the entire population, to get a distribution more representative of the individual plant. For the case of a head with N nozzles from a single heat, the updated distribution $\hat{p}(\theta)$ of the Weibull scale factor after operation for t years with no leaks can be obtained from

$$\hat{p}(\theta) = \frac{\left(1 - W(t,\theta)\right)^{N} p(\theta)}{\int_{0}^{\infty} \left(1 - W(t,\theta)\right)^{N} p(\theta)\, d\theta} \tag{9}$$

where $\hat{p}(\theta)$ is the updated distribution, $W(t,\theta)$ is the cumulative Weibull probability of leakage after t years for a scale factor θ, and $p(\theta)$ is the prior distribution of the scale factor theta. Similarly, if there have been n_f leaks, the updated distribution for θ is

$$\hat{p}(\theta) = \frac{\left\{W(t,\theta)^{n_f} \left(1 - W(t,\theta)\right)^{(N-n_f)}\right\} p(\theta)}{\int_{0}^{\infty} \left\{W(t,\theta)^{n_f} \left(1 - W(t,\theta)\right)^{(N-n_f)}\right\} p(\theta)\, d\theta} \tag{10}$$

where n_f is the number of leaks that have occurred by time t.

Although each element of the model can be assessed for the strength of the associated data base and the degree of conservatism of assumptions associated with it, it is difficult to benchmark the integrated model. One comparison is the expected number of large cracks with the observed number of large cracks. For a plant population with the same operating times, temperatures, and number of nozzles as the plant in Table 1, the expected number of large (165°) cracks and nozzle ejections is shown in Table 4 for different CGR correlation assumptions. Two such large circumferential cracks have been observed in the inspections to date. No nozzle ejections have occurred.

Table 4 Expected number of large cracks and nozzle failure in a population with operating times and temperatures as given in Table 1 for different assumptions about the degree of correlation between the CGR and Weibull scale factor for initiation

Model	165°Cracks	Nozzle Ejections
No Interpolation 0.1–0.25 CGR window	4.1 ± 1.0	1.1 ± 0.53
0.1–0.25 CGR window	2.8 ± 0.7	0.7 ± 0.33
0.25–0.25 CGR window	1.8 ± 0.6	< 0.7

References

1. J. Gorman, R. Staelhe, and K. D. Stavropoulos, *Statistical Analysis of Steam Generator Tube Degradation*, EPRI NP–7493, EPRI, Palo Alto:1991.

2. *Materials Reliability Program (MRP) Crack Growth Rates for Evaluating Primary Water Stress Corrosion Cracking (PWSCC) of Thick–Wall Alloy 600 Materials (MRP–55) Revision 1,* EPRI, Palo Alto, CA, TR–1006695, 2002.

3. P. M. Scott "An analysis of primary water stress corrosion cracking in PWR steam generators," *Proc. NEA/CSNI–UNIPEDE Specialist Meeting on Operating Experience with Steam Generators*, Paper 5.6, Brussels, 16–20 September 1991.

4. P. M. Scott, "Prediction of Alloy 600 Component Failures in PWR Systems," *Proceedings of the CORROSION/96 Research Topical Symposia 1996*, National Association of Corrosion Engineers (NACE), Houston, 1996.

Analysis of Weld Residual Stresses and Circumferential Through-Wall Crack K-solutions for CRDM Nozzles

D. Rudland[1], G. Wilkowski[1] Y.-Y. Wang[1], and W. Norris[2]
1) Engineering Mechanics Corporation of Columbus, Columbus, Ohio USA
2) US Nuclear Regulatory Commission, Office of Nuclear Reactor Research

Summary

The U.S.NRC has undertaken a program to assess the integrity of CRDM nozzles in existing plants that are not immediately replacing their RPV heads. This paper summarizes some of the efforts undertaken on the behalf of the U.S.NRC for the development of detailed residual stress and circumferential crack-driving force solutions to be used in probabilistic determinations of the time from detectable leakage to failure. Three major observations to date are:

- The weld residual stresses (without pressure and at ambient temperature) can produce compressive axial stresses at the root of the J-weld for weld sizes larger than the ASME specification;
- The crack-driving force is a large function of the nozzle yield strength, nozzle-to-head angle, interference fit, and weld residual stress; and
- In many cases, when the crack is made to be perpendicular to the wall of the nozzle, the residual stresses appear to create some crack closure along the crack faces.

Introduction

The occurrence of CRDM nozzle cracking in European PWRs in the early 1990's was limited to the formation of PWSCC axial cracks in the Alloy 600 nozzles. Axial cracks in these nozzles are not a safety concern, but present a situation of primary pressure boundary leakage that is not allowed by the plant technical specification. In early 2001, several circumferential cracks were found in CRDM nozzles in U.S. nuclear power plants. It is speculated that these cracks were formed by PWR water that leaked from axial cracks to the annular region between the nozzle and the head. The circumferential cracks occurred above the J-weld in the Alloy 600 nozzle. Although the pressure-induced axial stresses for full rupture of the nozzle are low, some of the circumferential cracks that have occurred were quite long (i.e., up to 165 degrees in length on the OD surface, but shorter in length on the ID surface). Since the crack sizes were quite large, the possibility of the nozzle being ejected from the RPV head is a significant safety concern. Consequently, the U.S.NRC has undertaken a program to assess the integrity of CRDM nozzles in existing plants that are not immediately replacing their RPV heads. This paper summarizes some of the efforts undertaken to date on the behalf of the U.S.NRC for the development of detailed residual stress and circumferential-crack driving-force solutions for use in the probabilistic determinations of the time from detectable leakage to failure.

The efforts involved in this program to date include determining the J-weld residual stresses for a center-hole nozzle case (where several sensitivity studies were conducted), and for a 53-degree side-hill nozzle geometry. The residual stress modeling was very detailed and included:

- Weld metal solidification;

- Temperature dependency of the stress-strain curves of the weld metal, head material, and Alloy 600 nozzle material;
- Evaluating the effects of the height of the weld, the weld bead layout sequence, the yield strength of the nozzle, interference fit, and operating temperature, and
- Applying hydrotest conditions to the model.

A key aspect of this evaluation involved being able to map the residual stress field from an uncracked-nozzle finite element mesh to a cracked-nozzle finite element mesh. This allows the evaluation of the crack-driving force with 3D stress and strain contributions. Once the stresses are mapped, the model is taken to operating temperature and the design pressure. At the operating conditions, the crack is unpinned and the crack-driving force is determined in terms of J and K (J is first calculated to capture the elastic and plastic components and then converted to K, termed K_{eq}). Because all the stress components are present and the whole head is included in the model, the different modes of crack loading can be determined, i.e., Mode I is crack opening, Mode II is in-plane crack sliding, and Mode III is out-of-plane tearing.

Analysis Matrix

The stress fields in the J-weld region and the adjacent CRDM nozzle are expected to be a function of weld fabrication and RPV operating conditions. To conduct the weld stress analyses, detailed information was first obtained on typical CRDM nozzle designs and welding procedures. An industry survey was conducted to obtain the information. The survey revealed that:

- Different RPV head manufacturers employed different weld design details and fabrication techniques to install the CRDM nozzle into the RPV head.
- The reactor operating conditions (temperature and pressure) vary from plant to plant, and may change with time for a given plant.
- The strength level of the CRDM nozzle, an important variable affecting the nozzle stresses, varies among the nozzle nozzles installed in different RPV heads that are in service.
- Due to the changes in the angle between the nozzle and RPV head and the variations in the weld geometry around the circumference of a nozzle, the location of nozzle in the RPV head may have strong influence on the stress states.

Geometry

To date, only a selected set of welding and geometry conditions were considered to establish the baseline conditions on the effects of fabrication and in-service conditions on the stress states in the CRDM nozzles.

The RVP head geometry analyzed was a Westinghouse design, fabricated by Combustion Engineering for the Pressure Vessel Research User's Facility (PVRUF) at Oak Ridge National Laboratory. Figure 1 shows the basic dimensions of this RPV head. The geometric features and materials surrounding the nozzle penetration are depicted in Figure 2. In the J-weld groove, an Alloy 182 butter layer was deposited on the steel head side, before the groove was filled with multiple passes of Alloy 182 filler metal.

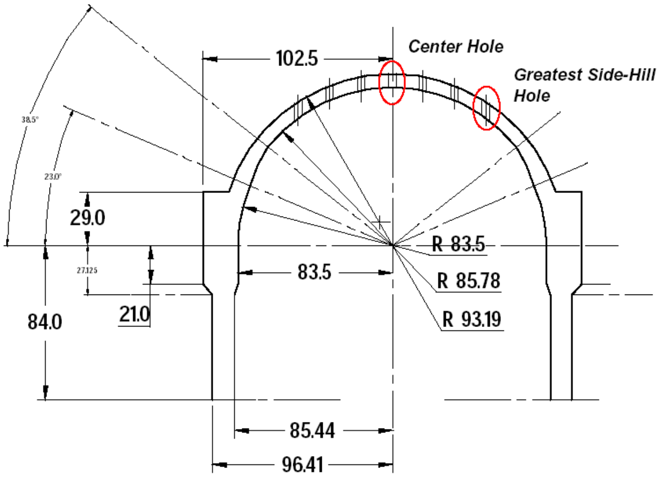

Figure 1 RPV head geometry used in the weld residual stress analysis (length in inches)

The initial analyses were for a center-hole geometry, followed by a more detailed 53-degree angle side-hill geometry. The side-hill nozzle analysis is much more complicated, hence the initial parameters of interest were first explored in the center-hole case. Using the center-hole nozzle, the following factors were investigated:

- Weld size and number of weld passes,
- Weld bead layout sequence,
- Interference fit,
- Yield strength level of the nozzle, and
- Operating temperature of the reactor.

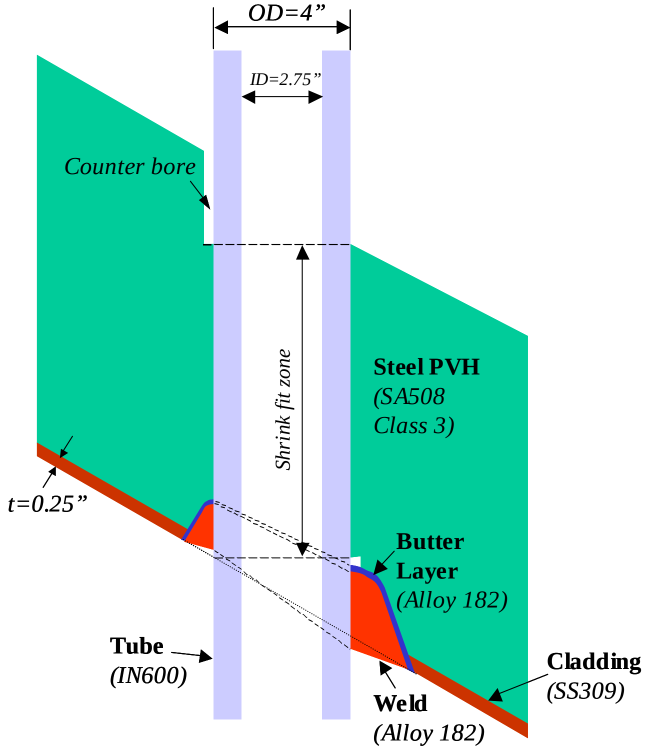

Figure 2 Geometric and material details of a nozzle penetration considered in the residual stress analysis (no counter bore used in center-hole geometries)

The analysis matrix was selected based on the industry survey. Four levels of the interference fit (the difference between the outer diameter of the nozzle and the diameter of the penetration hole) were analyzed for the center-hole location. The 0.2286-mm (9-mil) diametral interference fit corresponded to the greatest anticipated, and the 0.0508-mm (2-mil) diametral interference fit was close to the average. The two nozzle yield strength levels selected for the analyses represented the extremes of the nozzle strength levels from the industry survey. The 13-pass, 20-pass, and 27-pass welds for the center nozzle location had weld areas of 0.4 in^2, 0.56 in^2, and 0.8 in^2, respectively, covering the range of weld height reported by the industry for the center-nozzle location. Based on the center-hole stress analysis results, a 14-pass weld, which was expected to exhibit higher axial stresses at the root of the J-weld, was selected for the side-hill location.

Material Properties

For simulating welding residual stress, material properties over a wide range of temperature are required. Great care was taken to ensure that the material properties used in the weld simulation analysis were as realistic as possible. The material properties necessary for the CRDM weld stress analysis were collected from various sources in the open literature and through data exchanges with industry. In addition, the stress-strain curves for Alloy 182 weld metal [up to 1,255K (1,800F)] and SA-508 [up to 810K (1,000F)] were experimentally determined at Oak Ridge National Laboratory. In particular, for the weld analysis, the ORNL experiments were conducted using solution-annealed weld metal. In simulating the welding fabrication process, a solidification process occurs, and the plastic history is calculated on a pass-by-pass basis. Using as-welded tensile test data in the finite element analysis would produce excessive stresses in the weld metal.

Additionally, the ORNL tests were conducted with a strain rate of 10^{-3} per second, which was much higher than the standard tensile test (in the range of 10^{-5} per second). This strain rate was consistent with the deformation rate in the weld region during welding.

The material properties used for the weld stress analysis included the thermophysical properties (density, specific heat, thermal conductivity, and latent heat of fusion) for the heat-flow analysis, and the mechanical properties (elastic modulus, Poisson’s ratio, true-stress versus true-plastic-strain curves, and thermal expansion coefficient) for the mechanical stress analysis. Except for the density and latent heat of fusion, all other properties were temperature dependent.

Welding Conditions

The J-weld groove geometry used in this study is illustrated in Figure 3. The bottom of the J-weld groove is relatively flat, and transitioned into a 22.5-degree straight opening angle. This particular J-groove shape was a common weld joint design in typical U.S. manufacturer RPV heads that are in operation.

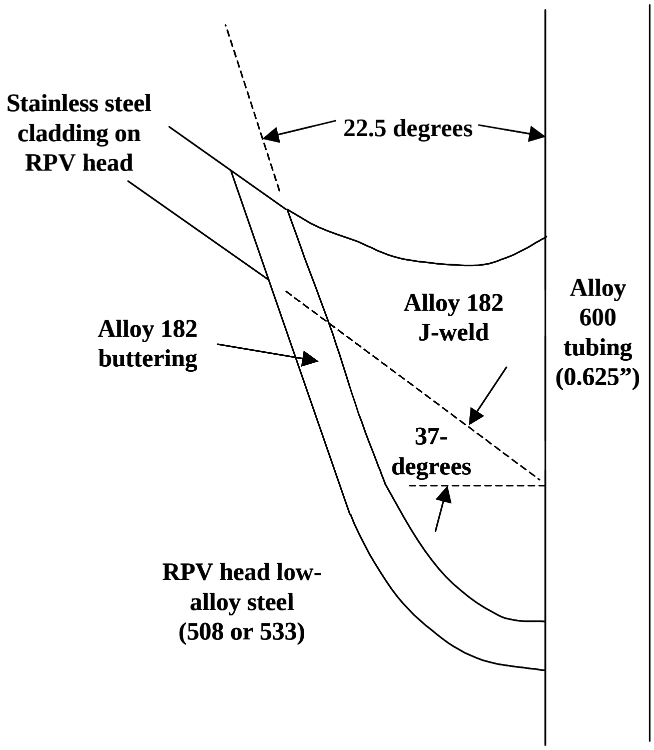

Figure 3 Cross-section of a J-weld at side-hill location

Due to the complex evolution of the groove geometry around the circumference of the CRDM nozzle, manual stick welding (shielded metal arc welding, SMAW) has been the choice of process to make the J-weld. The basic welding parameters used in the analysis were:

- Preheat temperature: 60 F minimum,
- Inter-pass temperature: 350 F maximum,
- Weld progression sequence: vertically from groove bottom to top; horizontally, either from nozzle to head or from head to nozzle,
- Electrode rod diameter: 5/32" maximum, and
- Welding current: 80-105 amps for 1/8" diameter electrode, and 105-140 amps for 5/32" diameter electrode.

Modeling Procedure

The computational analysis consisted of three basic sequential steps:

- <u>Weld Stress Analysis</u>. This analysis determines the stress states resulting from fabrication of the RPV head, hydrostatic testing, and in-service temperature and pressure loading;
- <u>Stress Mapping</u>. This step transfers all solution variables (stress tensor, strain tensors, displacements, and boundary conditions) from weld mesh used in the residual stress analysis to a mesh modeled with an idealized through-wall crack;
- <u>K-Solution Analysis</u>. This step involves applying the service load (pressure and temperature) to the mesh mapped with the weld residual stress, unzipping the

cracked mesh, calculating the K-solution, and curve fitting the K-solutions for use in probabilistic coding.

Weld Stress Modeling Procedure

The finite element simulation followed the actual sequence of events in CRDM fabrication process. For each case, the analysis consisted of five major sequential simulation steps corresponding to the following major fabrication steps:

- Heat treatment of the head and buttered region of the J-weld groove for stress relieving at 1125 F ± 25 F,
- Installing the nozzle into the RPV head by shrinkage fit (head kept at room temperature and nozzle cooled in liquid nitrogen in actual fabrication),
- Welding the J-groove,
- Hydro-testing at 21.5 MPa (125% of the design pressure) at room temperature, and
- Pressure and temperature loading during operation.

The finite element analysis was undertaken using the general purpose code ABAQUS (Version 6.2). A set of user subroutines was used to deal with the special issues associated with welding heat-flow and stress analysis, which cannot be readily handled by the general-purpose commercial FE programs such as ABAQUS.

Welding the J-groove was simulated on a pass-by-pass basis, following the weld pass deposition sequence that would be used in the actual fabrication. A weld pass is activated only when it is deposited. Furthermore, the deformation of the contact surface between the nozzle and the RPV head and the changes in contact area and pressure during the welding process was simulated.

Figure 4 illustrates the overall modeling approach used to simulate the J-groove welding. The formation of the welding residual stress was a result of the thermal-mechanical deformation process during welding. The heat flow and mechanical deformation during welding were simulated using a sequentially coupled approach. The effects of solidification on material constitutive behavior were properly treated with proprietary user subroutines. The various aspects of the modeling approach are documented elsewhere [1-7].

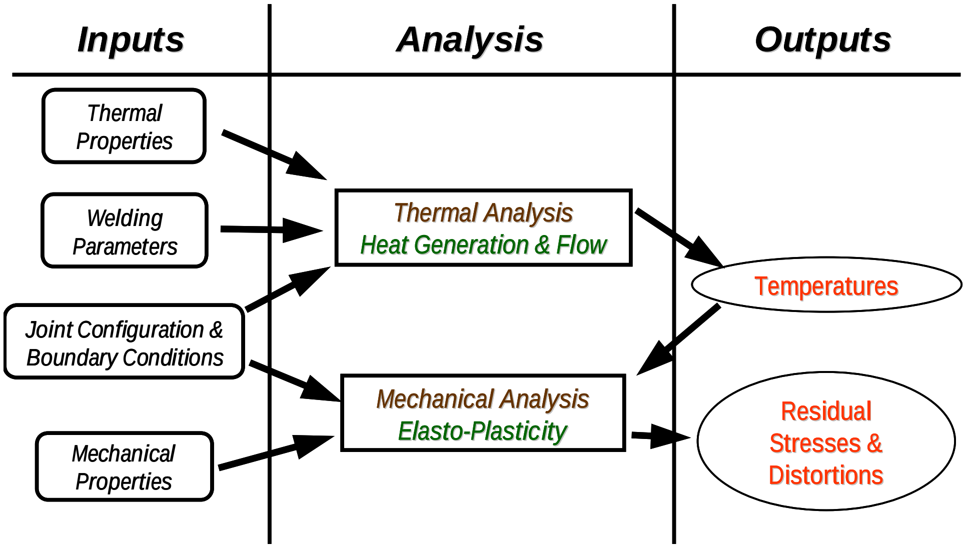

Figure 4 Thermal-mechanical modeling approach for welding residual-stress analysis

For the center nozzle, a combination of an axisymmetric model and a 3D model was utilized. Because of its effectiveness in computational time, the axisymmetric model was used to simulate the nozzle installation process. The final in-service stress distribution was then mapped into a 180-degree section of the RPV head, which was necessary for the fracture mechanics analysis of circumferential cracks.

Figure 5 shows the FE mesh of the axisymmetric model for a 20-pass weld of the center nozzle. Very refined elements were used in the weld metal, HAZ, and the adjacent region where the gradients of temperature and stress were expected high. There were 12 to 16 elements in each weld bead. The average element size in the weld and HAZ region was about 1 mm.

For the side-hill nozzle, the complex geometry of the nozzle penetration could be only simulated with a 3D model. In this study, the nozzle penetration at the greatest side-hill location was model by a 22.5-degree solid section as shown in Figure 6. There are approximately 70,000 nodes and 64,000 8-node linear brick elements in the side-hill model. This model has a symmetry plane through the center of the CRDM nozzle and the head. For simplicity, the counter-bore region was ignored in the finite element model for the side-hill case.

As part of this program, ORNL analyzed the structural compliance differences between a single-hole RVP head and an 81-hole RVP head. The ORNL results revealed that difference in the local structural compliance was negligible. For simplicity in creating the finite element meshes, each finite element analysis case contained only one nozzle penetration, for both the center-hole and side-hill locations.

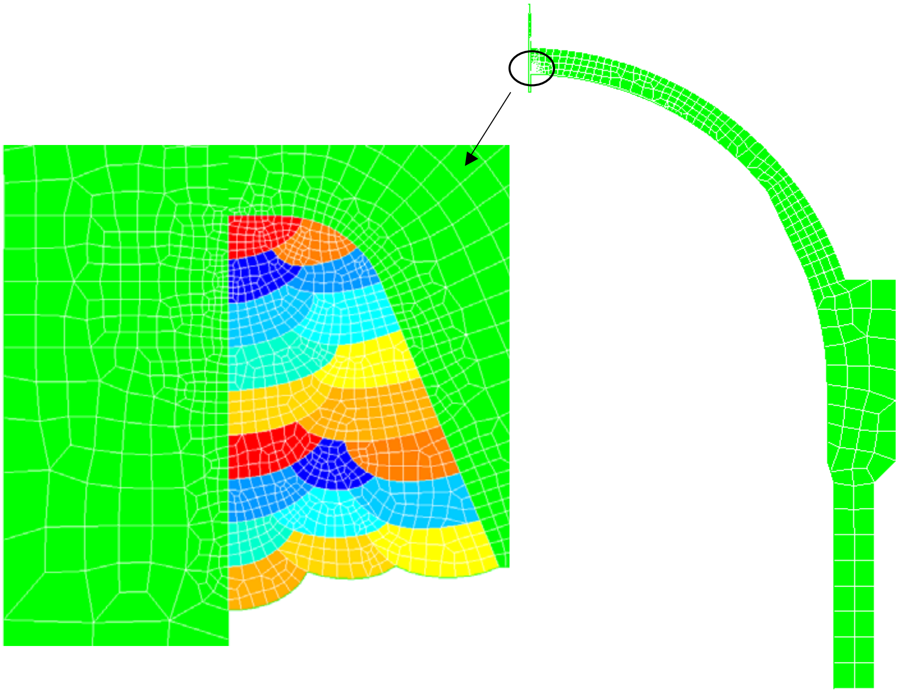

Figure 5 Axisymmetric model used in the baseline case (20 weld passes)

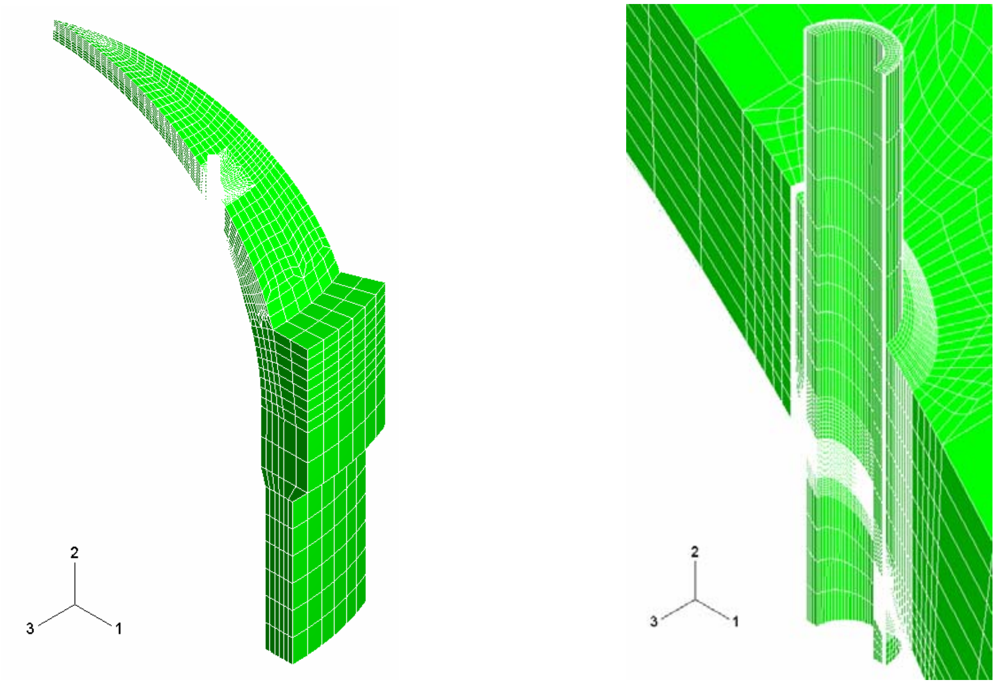

Figure 6 Finite element mesh for the side-hill case

Results and Discussions

Stresses in the J-Weld Region

Center Nozzle Cases

Figure 7 shows the predicted J-weld shape for a 13-pass weld. The corresponding axial and hoop stresses (with respect to the nozzle) are shown in Figure 8. For this particular case, tensile stress develops at the OD surface of the nozzle near the weld root where circumferential cracking was reported. In comparison, the hoop stress in the nozzle is much higher; formation of axial cracks occur with greater probability.

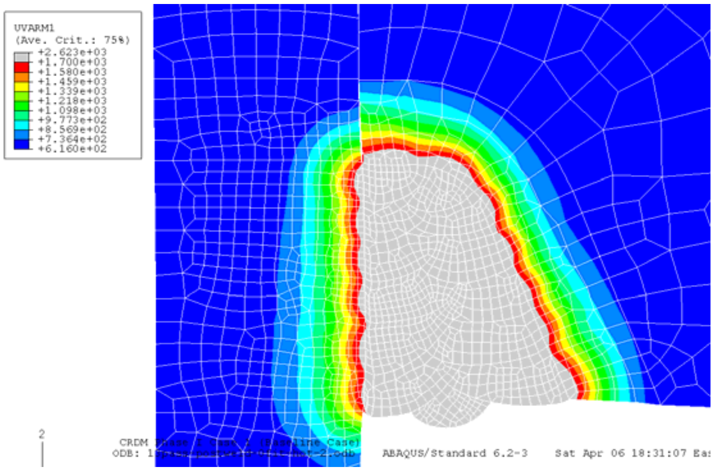

Figure 7 Predicted J-weld shape as depicted by the peak temperature distribution. 13-pass J-weld. Temperature is in Kelvin. Melting temperature: 1,700K.

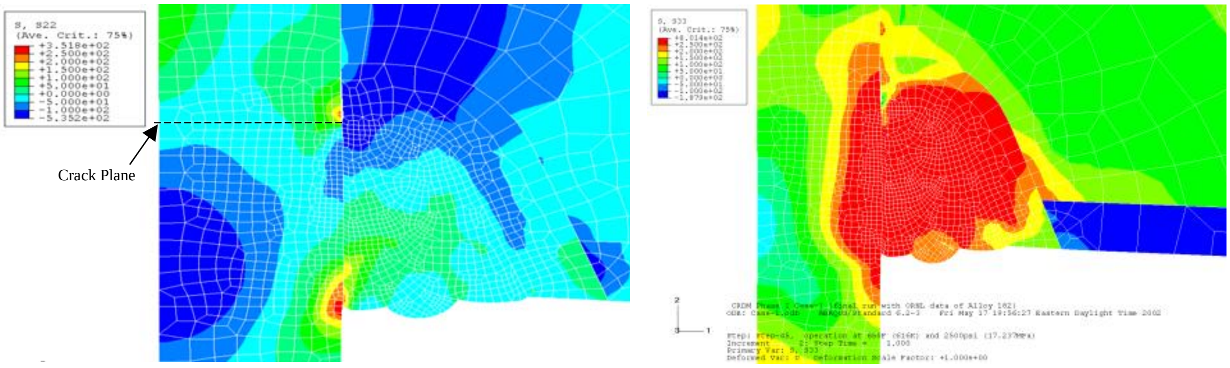

Figure 8 In-service stress distribution of a 13-pass J-weld (Case A). Left: axial stress; Right: hoop stress. 0-mil interference fit. Operating conditions: 650F and 2,500psi. Stress in MPa.

The amount of the weld metal deposited in the J-groove has strong influence on the stress distributions in the Alloy 600. Figure 9 shows the evolution of the axial stresses of a 20-pass J-weld as the welding progresses.

The evolution of the axial stress is quite dramatic. On the circumferential crack plane in the CRDM nozzle located at the root of the J-weld, high tensile axial stress develops on the OD side of the nozzle first. The axial stress then decreases in magnitude and eventually becomes compressive as more weld passes are deposited into the J-groove. The ID side of the nozzle starts with compressive axial stresses, but develops tensile axial stresses as the OD side experiences compression, as a result of force balance in the axial direction across the crack plane.

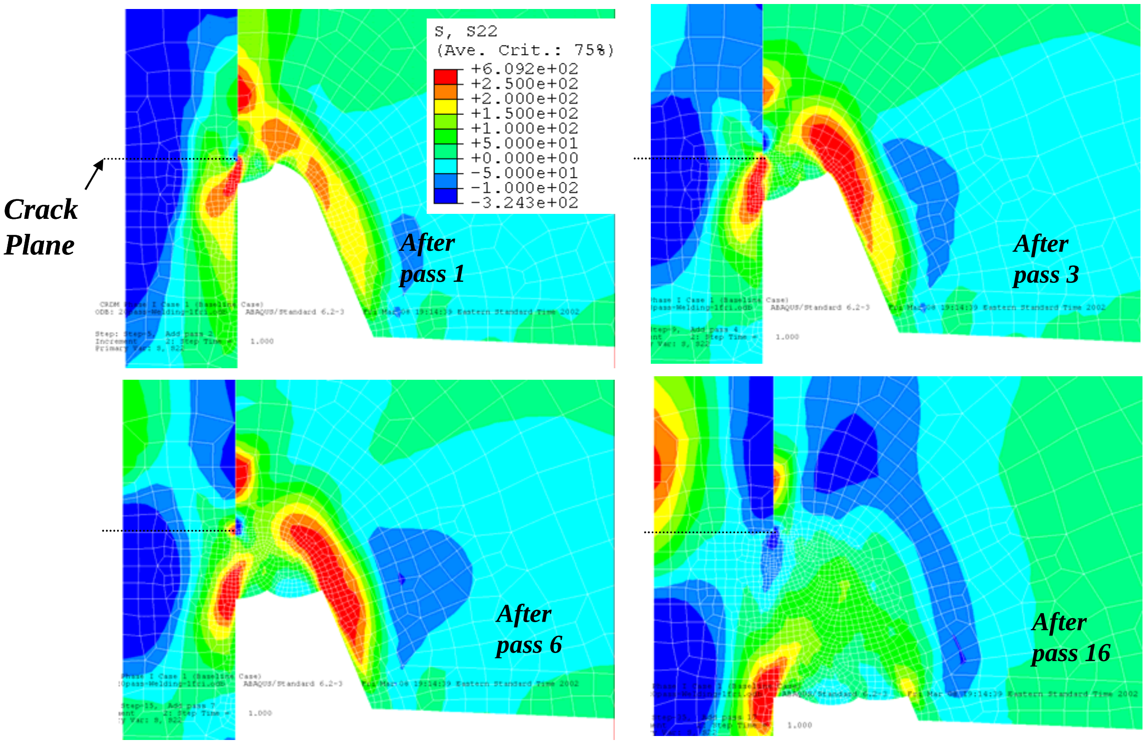

Figure 9 Development of axial residual stress in a 20-pass weld center-nozzle case

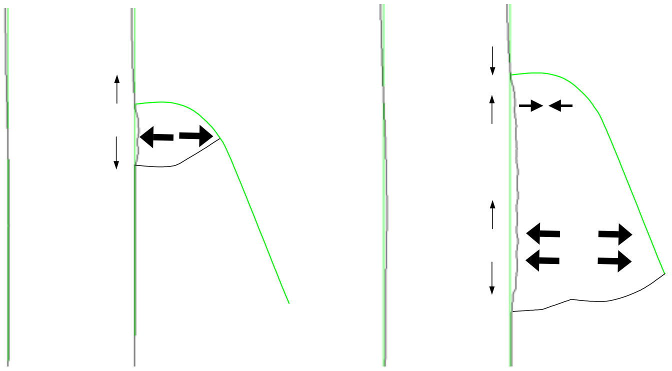

Figure 10 Deformation of the CRDM nozzle under the weld shrinkage force

The above-observed transition of the axial stress could be understood as a consequence of the progressive weld pass deposition and weld metal shrinkage that takes place during welding the J-weld. In essence, the J-weld connects the CRDM nozzle to the RPV steel head. Since the steel head is much stiffer than the CRDM nozzle (in the radial direction to the nozzle), the weld metal shrinkage in the radial direction will pull the nozzle toward steel head as shown in Figure 10. Statically, this is equivalent to the CRDM nozzle subjected to an outward radial force from the J-weld shrinkage, which results in axial bending stress that is tension on the OD side of the nozzle adjacent to the radial force region. When the first several weld passes are deposited, the radial shrinkage force is located near the weld root. The radial shrinkage force from the first several weld passes results in the tensile axial stress in the CRDM nozzle near the J-weld root region. However, as more weld passes are further deposited into the J-groove, the weld passes already deposited will act as a “hinge point” to resist the shrinkage from the weld passes being deposited. The result is that the shrinkage force from the latter passes will “compress” these previously deposited hinge-passes. As additional weld pass are deposited, the accumulation of the compression effect will eventually cause compressive stresses in the root area of the weld.

According to CRDM inspections in 2001 at the Oconnee Nuclear Plant [8], the circumferential crack normally occurs on the OD side of the nozzle. In this regard, a large J-weld where compressive axial stress develops at the weld root area would be beneficial to prevent or slow down the formation of the circumferential cracks.

One must recognize that the existence of axial cracking, particularly the longer ones, could significantly alter the axial stresses at the weld root region, thereby changing the sensitivity of circumferential cracking. One postulate would be that the axial cracks usually initiate near the toe or crown of the weld. The growth of these axial cracks could partially release the shrinkage action of the lastly deposited weld passes. Because of the formation of axial cracks, the compression of the weld root area from the latter weld passes could be reduced and the probability of circumferential cracking could be increased.

Some J-groove designs have a smaller J-groove angle. So for a given weld height, the amount of the weld metal and the compression effects could be reduced. This could be detrimental to the formation of circumferential cracks. This is expected to be an important issue that needs to be further investigated in future studies.

Figure 11 shows the axial and hoop stresses where the nozzle yield strength increased to 65 ksi (444 MPa). The corresponding low yield strength case (37.5 ksi, 260 MPa) is Figure 8. Clearly the tensile stresses at the OD surface of the nozzle next to the J-weld increase with the yield strength level of the nozzle. The increase in the axial stress at the weld root region is particularly noticeable. In this regard, nozzles with higher yield strength would be more susceptible to the CRDM cracking.

Compared with the weld volume/height and nozzle yield strength, the other factors investigated (interference fit and operating temperature) show minimal effects on the stresses under the operating conditions.

Figure 12 shows the direction and magnitude of the maximum in-plane principal stress for a 20-pass weld. Clearly, the principle stress direction in the nozzle cross-section near the root of the weld was not in the longitudinal direction, but was at an angle of about 45-degrees. Since subcritical crack growth is in the Mode I direction (perpendicular to the principal stresses), circumferential cracks may grow at an angle through the thickness.

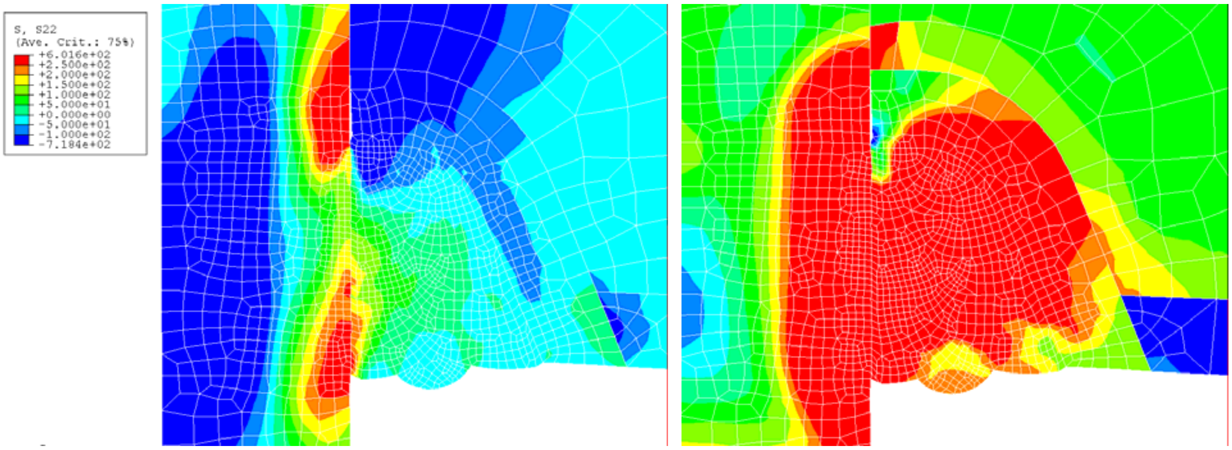

Figure 11 In-service stress distribution of a 13-pass J-weld with high yield strength nozzle (Case G). Left: axial stress; Right: hoop stress. 0-mil interference fit. At operating conditions: 605 F and 2,500 psi. Stress in MPa.

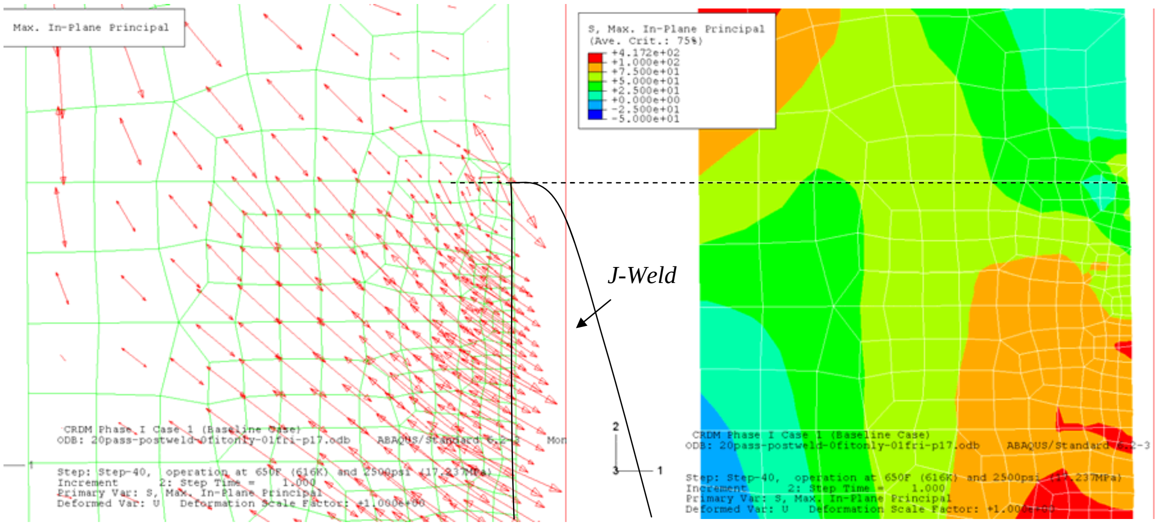

Figure 12 Distribution of maximum in-plane stress in the nozzle near the J-weld root for a center-hole 20-pass weld nozzle

Side-Hill Nozzle Case

Figure 13 shows the axial stress distributions on the symmetric plane and the ID surface of the nozzle in the J-weld region. Figure 14 highlights the axial stresses on the OD surface of the nozzle. Figure 15 shows the longitudinal stress contours at four different sections through the nozzle and the weld. All of these stress contour plots are at 2,500 psig and 605 F. Clearly, there are significant variations of stresses around the circumference of the nozzle. One of the more interesting aspects from this analysis is that the highest longitudinal tensile stress above the J-weld is at the side of the nozzle, not at the uphill or downhill locations. This is believed to be due to the weld sequencing procedure used, which was closer to an actual procedure used by one U.S. Manufacturer.

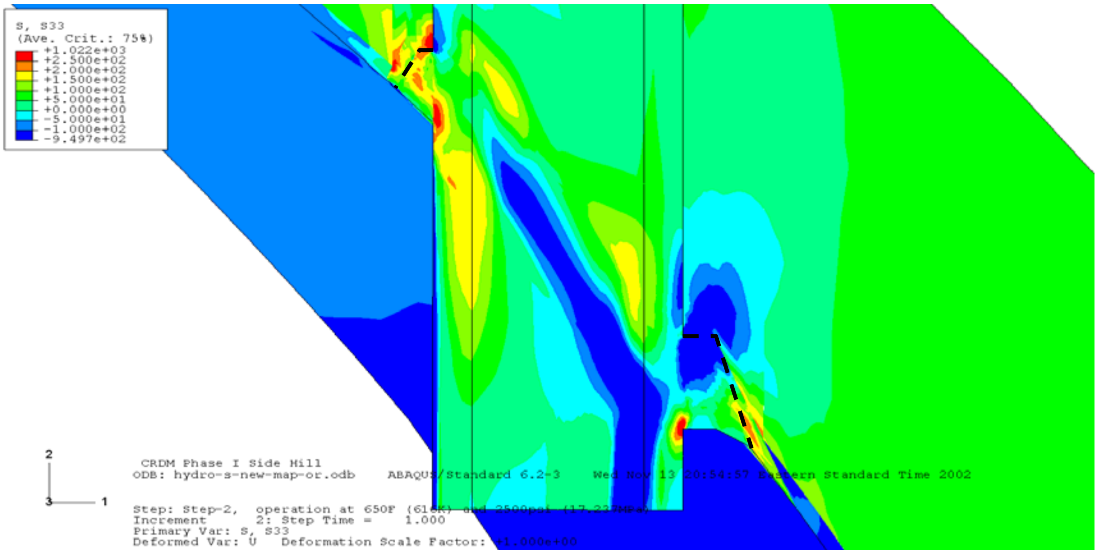

Figure 13 Axial stresses with respect to the nozzle axis
(At operating conditions after hydrotest simulation)

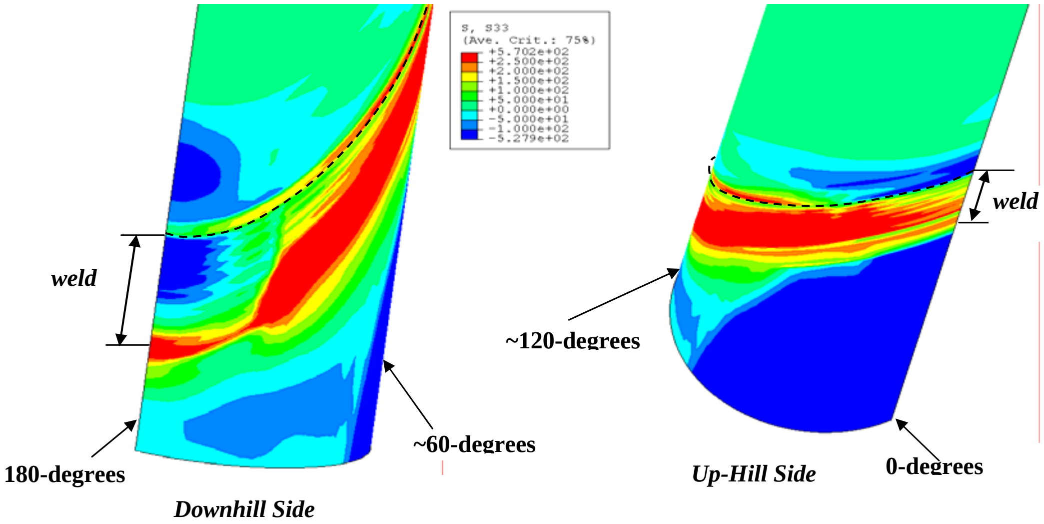

Figure 14 Axial stresses on OD of nozzle (angled views)
(At operating conditions after hydrotest simulation)

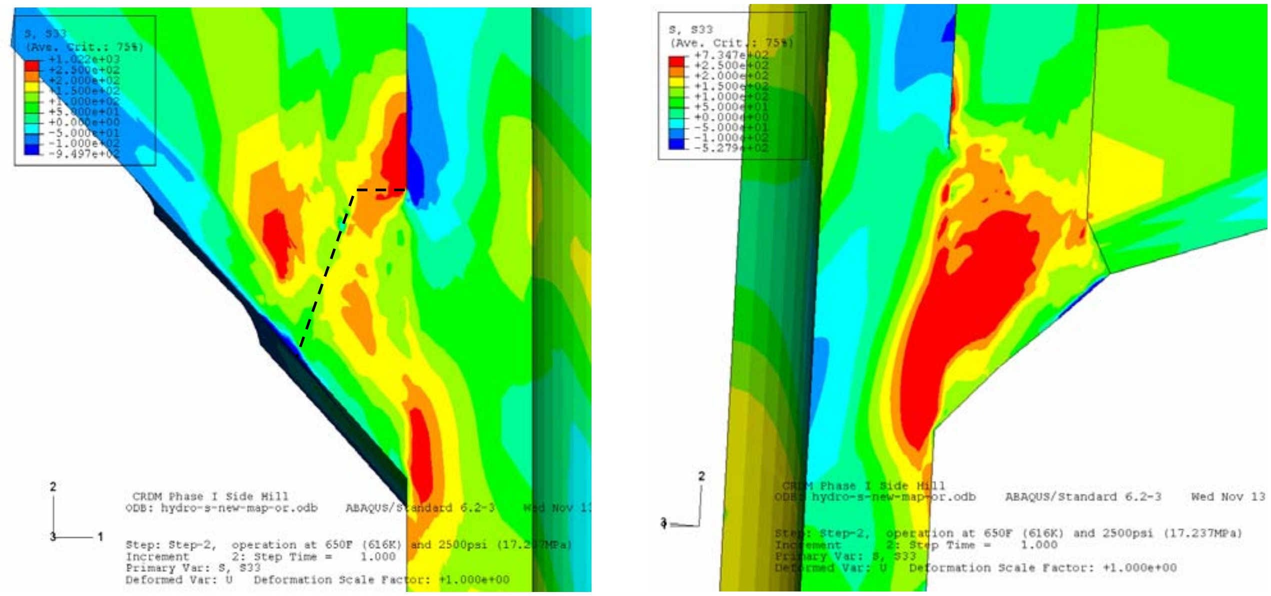

(a) 0-degrees (b) 45-degrees

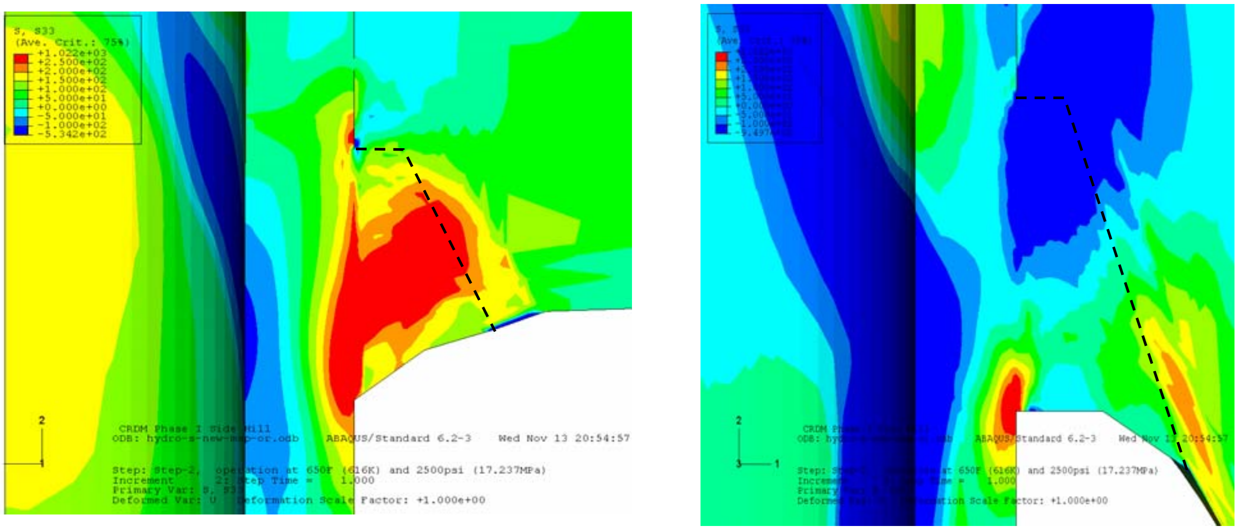

(c) 90-degrees (d) 180-degrees

Figure 15 Axial stress contours at different section locations
(At operating conditions after hydrotest simulation)

Mapping and K-Solution

Once the residual stresses were calculated and the weld metal was allowed to cool to room temperature, the hydrotest pressure (125% of design pressure) at room temperature was applied to the head and then removed. The efforts to develop the crack-driving force for the circumferential crack used the following procedure.

- The entire post-hydrotest residual stress field was mapped to a new FE model that contained a circumferential crack that was pinned closed.
- The model was then taken to operating pressure (2,500 psig) and temperature (560 F or 605 F for cold versus hot heads).

- The crack was then unpinned, and the crack-driving force (K from J) was calculated.
- Since the entire stress field of the head was mapped to the cracked model, all the crack-driving force components (Modes I, II, and III) contributed to the J value.

The J values accounted for plasticity, but the K values for the three different modes were calculated. The steps in this K-solutions analysis are discussed below

Residual Stress Mapping

The full residual stress solution from the weld analysis was mapped directly to new finite element model with a refined crack-tip mesh. The model used was identical to the original finite element model expect for the presence of the refined crack tip mesh. An example of one of the new models for the center-hole and side-hill case is shown in Figure 16. Note that for the side-hill case, the crack is centered on the up-hill side since higher K-values were determined at this location in earlier work by Structural Integrity Associated for the MRP.

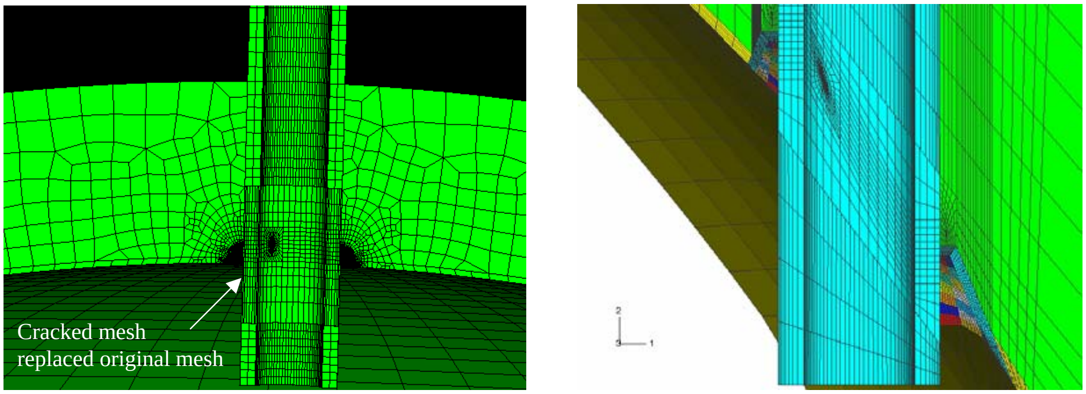

Center-hole Mesh **Side-hill Mesh**

Figure 16 Modified finite element mesh with refined crack tip mesh

The crack was defined as having a front that was perpendicular to the nozzle surface, but followed the J-weld contour around the nozzle. This mapping procedure was done for nozzles with different circumferential crack lengths (about 10 crack lengths per case), which was much more cost efficient that redoing the weld residual stress calculations for each cracked-nozzle case. The stress mapping procedure is relatively new in ABAQUS, and was validated with several test cases.

An example of the weld residual stresses mapped onto the cracked mesh for the center-hole case is shown in Figure 17. The comparison illustrates that the mapping procedure in ABAQUS does a reasonable job in correctly capturing the residual stress state in the original model. However, the courser mesh of the crack-tip model near the bottom of the weld shown in Figure 17 fails to capture some of the complexity of the residual stress pattern in the original model. It is unlikely that this detail has a significant effect on the K-solutions generated.

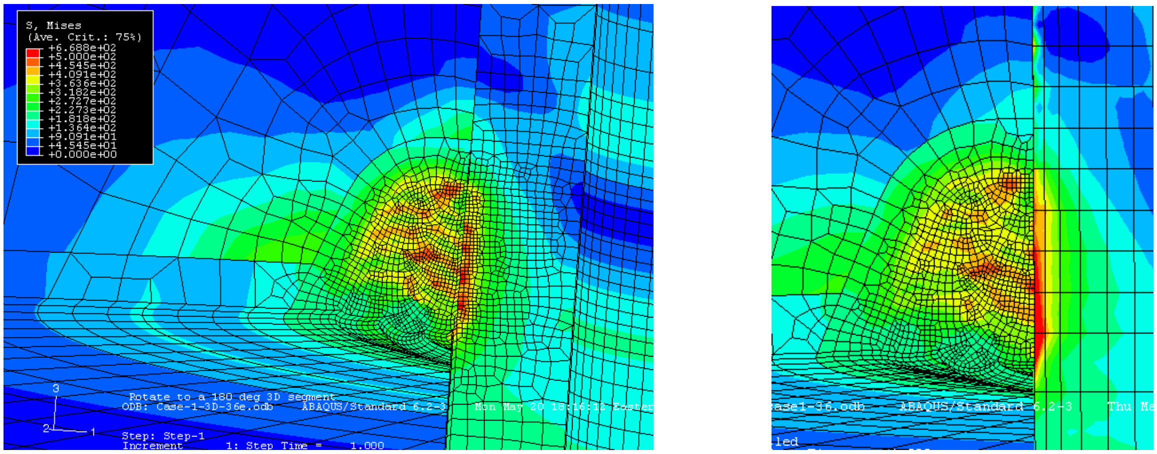

(a) Original (b) Mapped

Figure 17 Comparison of weld residual stress with mapped solution
(at room temperature, with no internal pressure, and prior to hydrotesting)

Parametric Analysis

The following parametric parameters were used in the analyses conducted in this study.

- 10 circumferential through-wall crack lengths per residual stress condition – from 40 to 320 degrees,
- Two nozzle yield strengths – 37.5 ksi (258.6 MPa) and 64.4 ksi (444 MPa),
- Three interference fits – 0, 2, and 4.5 mils (radial interference),
- Two operating temperatures – 605 F and 560 F,
- One design pressure of 2,500 psi,
- Friction between nozzle and RPV hole included a friction factor of 0.1, and
- Center-hole and largest side-hill angle (parametric analyses performed on center-hole model; only base case conditions were run on side-hill model to date.)

The baseline case is defined as the center-hole nozzle with the low yield strength nozzle, 0 mil interference fit and design conditions of 2,500 psi internal pressure and a temperature of 605 F. An example of the results from a 60-degree through-wall-cracked baseline solution for both the center-hole and side-hill cases are shown in Figure 18. As is shown in this figure, there is a modest amount of crack opening, but appears to be a significant amount of Mode III shearing. This effect is prevalent in all of the analyses conducted and appears to be a function of the loading conditions and not the weld residual stresses, which becomes apparent when the K-solutions are studied.

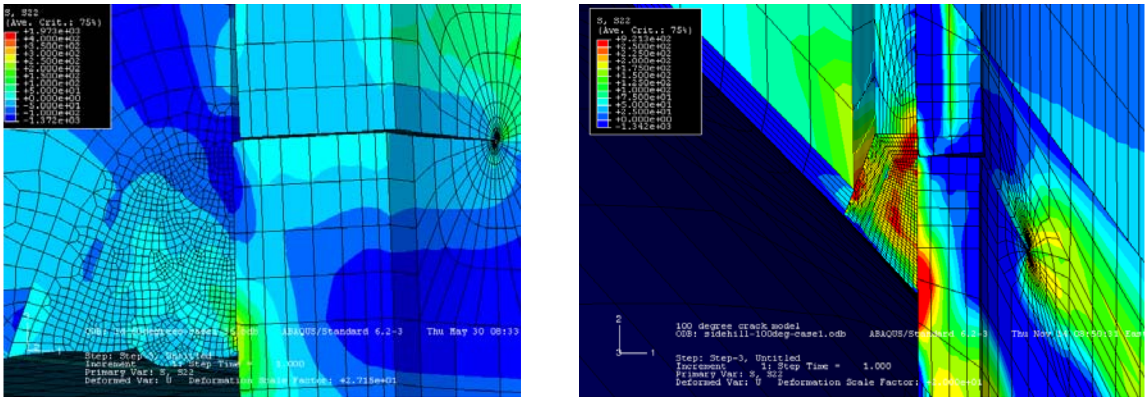

Center-hole Case **Side-hill Case**

Figure 18 Example of baseline case with a 60-degree through-wall crack showing residual and operating stresses in the axial direction of the nozzle

K-Solution Results- Center-hole Case

In all of the analyses conducted, the through-wall crack was set perpendicular to the wall thickness of the CRDM nozzle. Due to the geometry of the structure and the loads applied, the cracks experienced mixed-mode loading. Figure 19 shows the K-solutions for the baseline case with a 100-degree through-wall crack in the center-hole nozzle. At the outer diameter of the nozzle, the Mode I component of K is relatively large, but not dominant. The K_{III} component is a significant portion of the total crack-driving force on this crack. At the ID surface of the nozzle, the K_I component is a very small portion of the total crack-driving force with the K_{II} and K_{III} components dominating.

These results suggest that for subcritical crack growth by mechanisms such as PWSCC or fatigue, the angle of the TWC through the thickness of the nozzle would not be perpendicular to the wall thickness. In fact, since these types of growth mechanisms favor the Mode I type loading; it can be assured that the growth would be angled through the thickness.

Since the cracks analyzed in this study were experiencing mixed-mode loading, the comparisons conducted were made by calculating the J-integral and converting this value to a K_{eq} using the typical elastic relationship.

Upon calculating the J-integral for each crack-tip location along the crack front, it was discovered that the values were path dependent as the crack tip approached the outer diameter surface of the nozzle. This problem is illustrated in Figure 20. To eliminate this problem, a series of modified analyses were conducted to calculate the CTOD at the crack tip through the thickness to find a procedure to extrapolate the path independent values of J to the outer diameter surface of the nozzle. It should be noted that the complex stress and strain fields around this crack tip due to the residual stress fields make it difficult to use the standard correlations between J and Mode I CTOD. A more simplified approach was taken where the CTOD trends observed near the OD of the nozzle were used to make an engineering approximation of the J-integral at the OD of the nozzle.

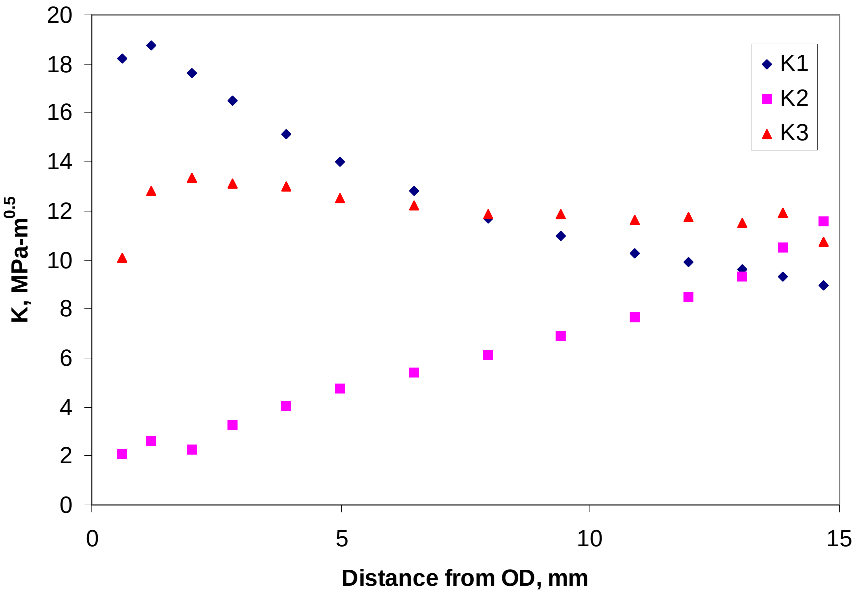

Figure 19 K-solutions for the baseline case with a 100-degree through-wall crack in the center nozzle

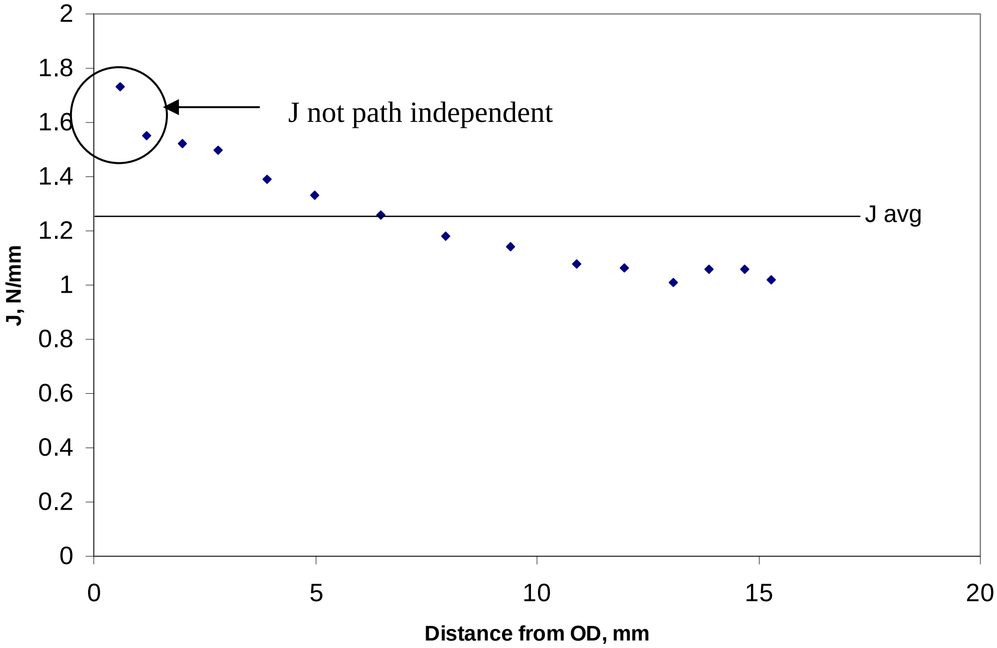

Figure 20 J-integral results for the baseline case with a 100-degree through-wall crack in center-hole nozzle (only path-independent J values used to determine the average J in this figure)

As shown in Figure 21, the CTOD appears to be linear with distance from the point where the J-integral becomes path dependent to the OD of the nozzle. Since the J-integral is directly related to the CTOD, it can be inferred that the J-integral is also linear though this region. Figure 21 illustrates how the J-integral is extrapolated to the OD of the nozzle. From these values, as equivalent K value was calculated by converting the weighted average J to K.

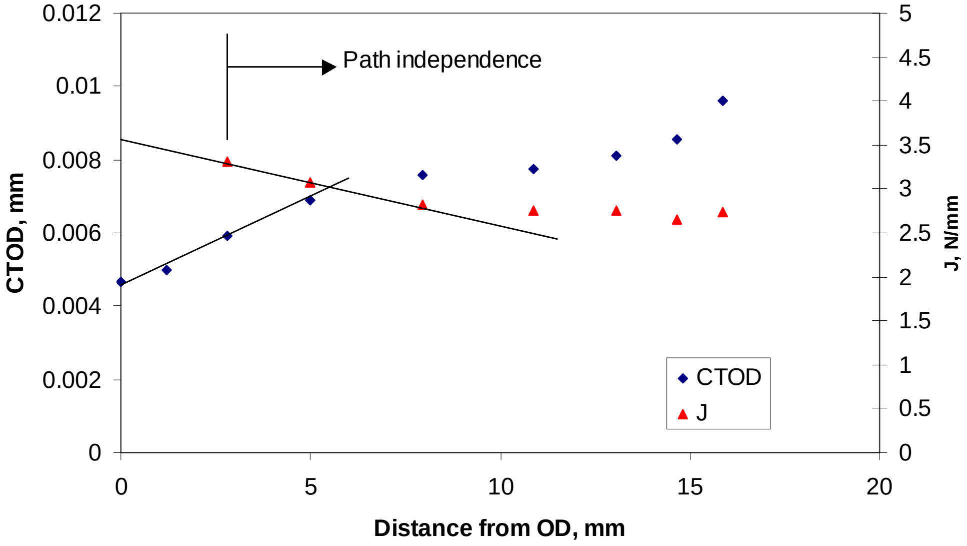

Figure 21 Relationship between CTOD and J at the OD of the nozzle for the baseline case with a 240-degree through-wall crack

The effects of interference fit on the K-solution for the center-hole nozzle are shown in Figure 22. In this figure, three different interference fits were examined. The values of interference fit shown in this figure represent radial interference. Note that the nozzle/head interface was modeled with a coefficient of friction of 0.1. The results from Figure 22 suggest that if the radial interference is less than 2 mils, the effects of the interference fit on the K solutions are very small. However, for the 4.5 mils radial interference case, the K-solution significantly decreases as compared to the baseline solution. In fact, for this interference fit, the K-solution appears to be almost constant for a crack length greater than 30 degrees. It is only for half crack angles greater than 150 degrees that the K-solution begins to increase slightly. The results shown in this figure will be affected by the amount of friction that is present between the nozzle and the head material.

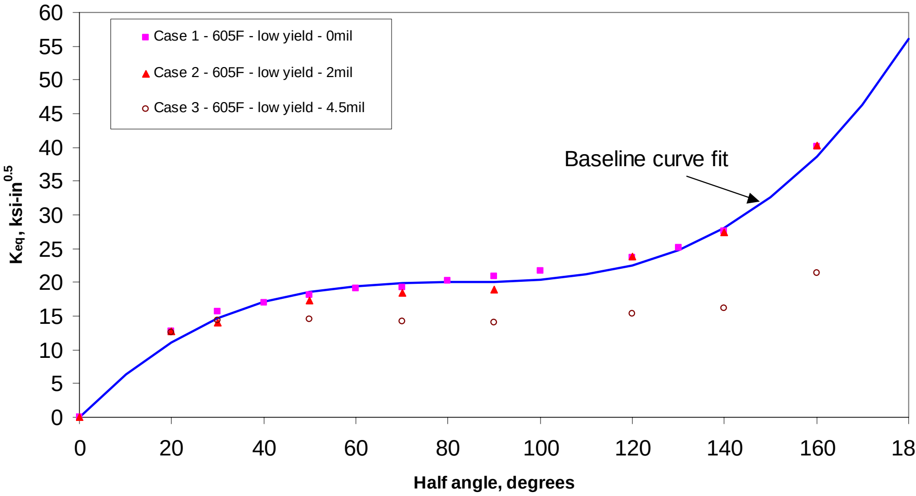

Figure 22 Effects of radial interference fit on the center-hole K-solution

The effects of operating temperature on the K-solution for the center-hole nozzle are shown in Figure 23. In this figure, only one interference fit and nozzle yield strength solution is shown. This figure suggests that for the typical operating temperatures investigated, there is little effect of temperature on the K-solutions for the center-hole nozzle.

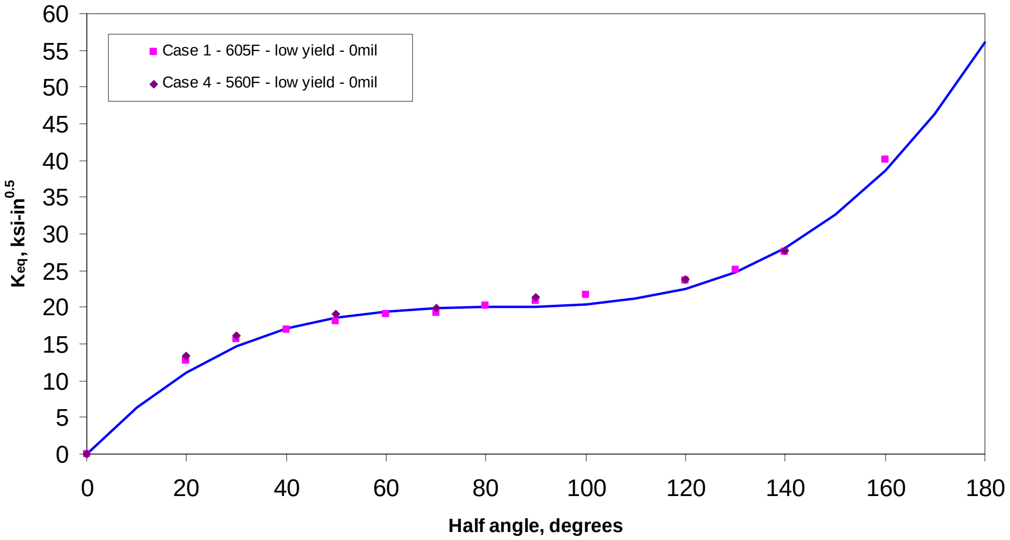

Figure 23 Effects of operating temperature on the center-hole K-solution

In the parametric analyses, two nozzle yield strengths were investigated. These two yield strengths represent the minimum and maximum values reported by EPRI/MRP and others. The effects of increasing the nozzle room temperature yield strength from 37.5 ksi (258.6 MPa) to 64.4 ksi (444 MPa) are shown in Figure 24. For these cases, only one interference fit (0 mils) and one temperature (605 F) were investigated. Increasing the nozzle yield strength significantly increases the K-solution for the center-hole nozzle. The K-solution through the thickness for the higher yield strength nozzle has a very steep gradient with very high K values at the OD surface. This large gradient, when averaged, gives the increase in the K-solution shown in Figure 24.

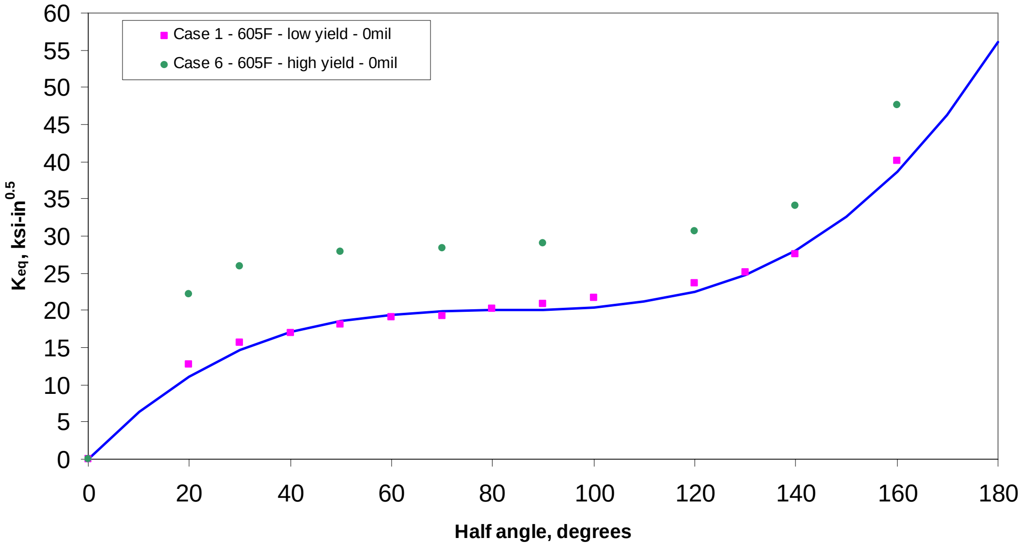

Figure 24 Effects of CRDM nozzle yield strength on the center-hole K-solution

If the average and maximum K values through the thickness are plotted, as shown in Figure 25, the magnitude of the K gradient is illustrated. For the low yield strength case, the difference in K between the maximum and average is approximately 10 percent. However, for the high yield strength case, the maximum K value is more than double the average value through the thickness. Clearly, the difference in weld residual stress due to the difference in yield strength causes large changes in the through-wall crack driving force.

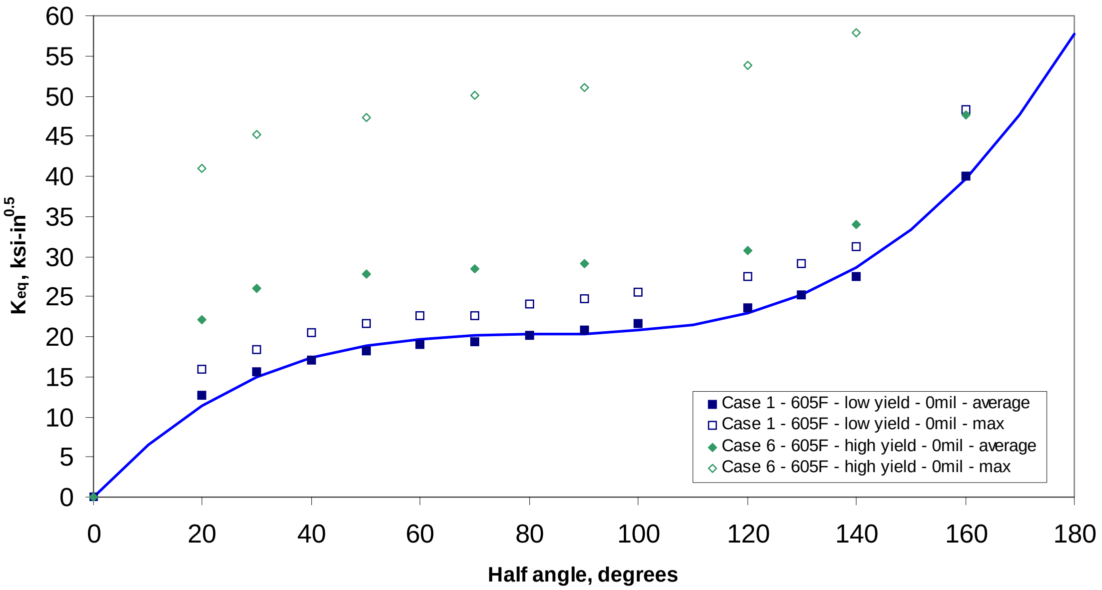

Figure 25 Comparison of maximum and average K solution for the center-hole nozzle

In all of the cases shown above, the residual stress fields described in this paper were mapped onto the cracked mesh to calculate the K-solutions. Additional analyses were conducted without mapping these residual stress fields to determine the true effect of the residual stress on the K-solutions. These results are shown in Figure 26. All cases shown in this figure are for one operating temperature (605 F) and one interference fit (0 mils). The results suggest that there is almost no difference between the baseline residual stress case and the cases run with no residual stress for half crack angles greater than 90 degrees. However, for the low-yield strength case, the K values are slightly higher with residual stress for half crack angles less than 90 degrees. However, by comparing Figure 24 and Figure 26, there is a large difference between the K-solution for the high-yield strength residual stress and no residual stress case.

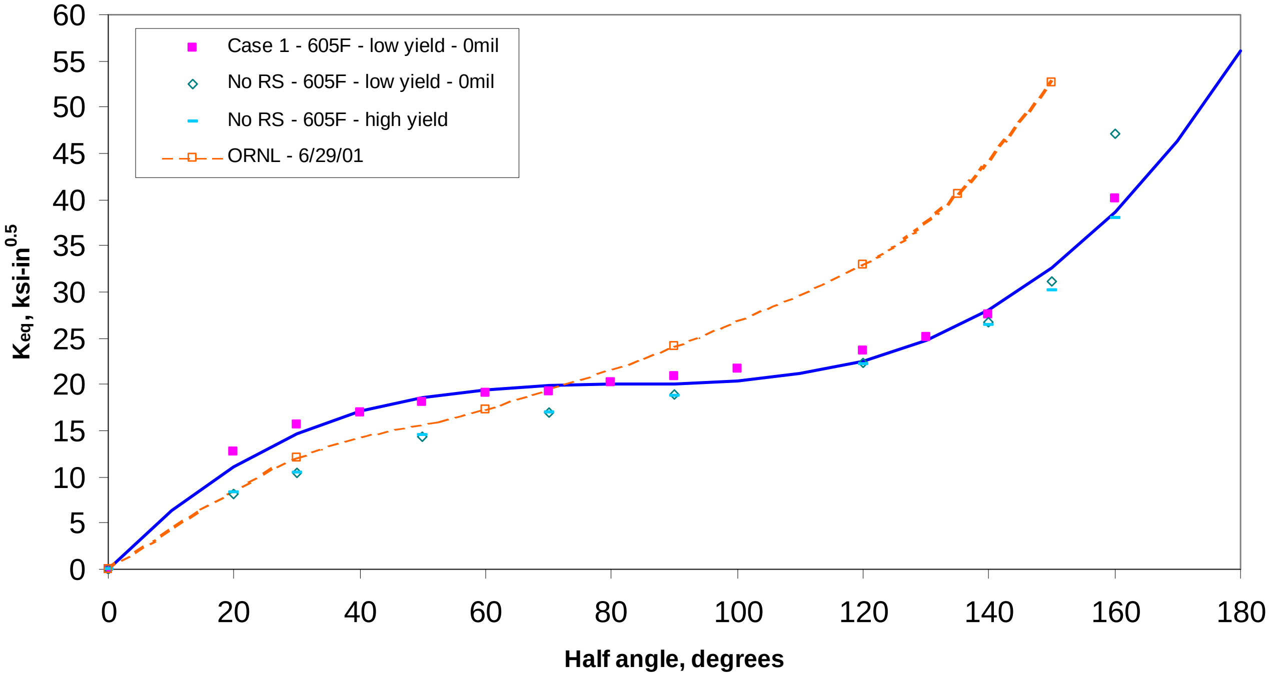

Figure 26 Effects of residual stress on the center-hole K-solution

Also shown in Figure 26 are nozzle-only results computed by ORNL. ORNL restrained the nozzle from radial motion in their nozzle-only solution, which is similar to what the RPV head does to the nozzle in our model with the whole head, except that we included the effects of friction. These results indicate that the ORNL solution matches the nozzle-in-head solution for half crack lengths less than 90 degrees, but for larger angles, the head geometry restrains the nozzle differently (the hole actually becomes tapered through the thickness from the pressure expansion of the head), and the K-solutions decrease significantly.

K solution results – Steepest (53 degrees) side-hill location

For the side-hill nozzle, only the baseline case was analyzed to date. Note that the baseline case consists of the low yield strength tube material, 0-mils interference fit, and 605F operating temperature. The baseline side-hill weld residual stress results were presented in Figure 13 to Figure 15. The K-solutions generated for this case are shown in Figure 27. In addition, similar cases were analyzed but without weld residual stresses. The results in Figure 27 indicate that the K values increase to about 30 ksi-in$^{0.5}$ and remain constant until the crack reached a half angle of approximately 140 degrees at which point it begins to increase. This effect is due to the large J gradient that exists through the thickness in the side-hill model. As shown in Figure 28, for an 80-degree crack, the J value increases from near zero (some crack closure does exist) to approximately 10 N/mm at the ID surface. However, for an 80-degree crack, the J value decreases from 5.5 N/mm at the OD to near zero (some crack closure does exist) at the ID surface. This change in slope of the J values through the thickness cause the average J values (as shown in Figure 27) to remain relatively constant as the crack length increases.

Referring back to Figure 27, without residual stress, the J values are very small until the crack length gets long. Investigation of the deformed shape indicates that crack closure occurs across a large portion of the crack plane, causing very low average J values. As with the center-hole model, the crack closure indicates mixed-mode loading on the crack, which would be eliminated if the crack is modeled at an appropriate angle through the thickness.

In addition, these results can be compared to additional K solutions generated elsewhere as shown in Figure 27. The solid line, sinusoidal solution represents the NRC K-solution developed from a preliminary technical assessment conduct by the U.S.NRC [9]. Solutions for both uphill and downhill K solutions from Structural Integrity Associates (SIA) [10] are also shown for comparisons. The uphill SIA solutions are slightly higher (conservative) than the solution generated in this program.

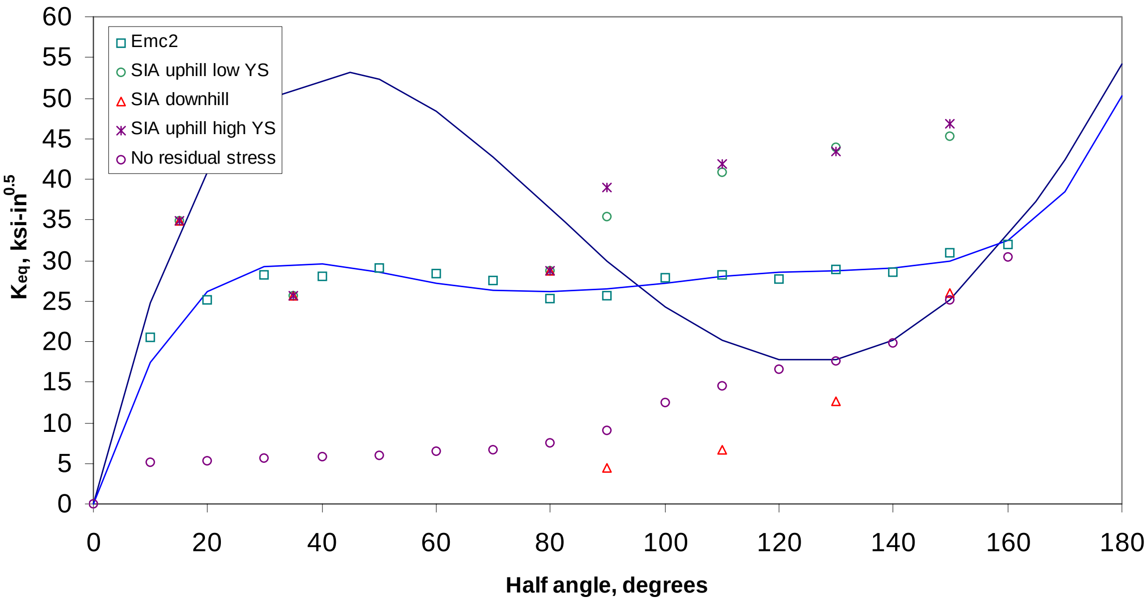

Figure 27 K-solutions for the steepest side-hill baseline case

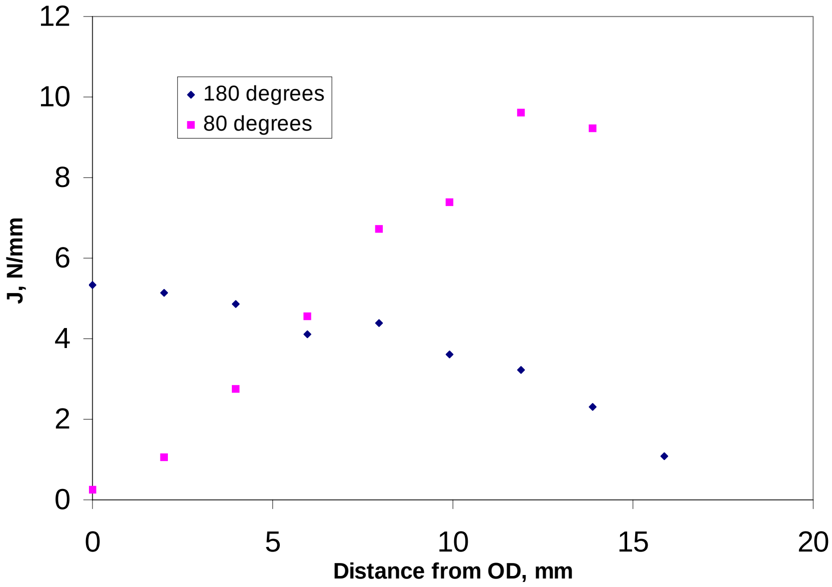

Figure 28 J gradient through the thickness for the side-hill model

Summary and Conclusions

From Weld Stress Analyses

- The as-welded stress states are primarily dependent on the J-weld size, the nozzle strength levels, and nozzle angle.
- There are appreciable differences between the as-welded stress states and the in-service stress state caused by hydro-test and by the pressure and temperature loading from operation.
- The hoop stresses in the nozzle next to the J-weld are high in tension, generally reaching the yield strength level of the nozzle on the OD and extending above and below the J-weld region.
- The axial stress is highly sensitive to the weld height.
- A large J-weld tends to be beneficial for the circumferential crack case as it creates compressive axial stresses at the root of the weld.
- As the J-weld height increases, the hoop stresses on the ID surface of the nozzle increase and the axial stresses at the J-weld root decrease. Hence there may be some optimal design of the J-weld geometry.
- The effects of other fabrication variables such interference fit are secondary to the stress distribution in the J-weld region.
- There are significant variations of stresses around the circumference of the side-hill nozzle, and the weld sequencing used (typical for one U.S. vendor) gave the highest stresses at 90-degrees from the uphill or downhill locations.

From K-solution Results

- The baseline solution consists of the center-hole nozzle with low-yield-strength nozzle material properties, a 0 mil interference fit between the nozzle and the head, an operating pressure of 2,500 psi and a temperature of 605 F.

- The average K values (called K_{eq}) were calculated from J values averaged through the thickness where there was path independence. There was a small plastic contribution with the higher J values.

- The nozzle yield strength has a large effect on the K solution. A high yield strength gave large J gradients through thickness, which increased the average equivalent K as compared to the baseline solution.

- For the center-hole low yield strength cases, residual stress made no difference on the K solutions for through-wall cracks greater than 180 degrees. However, this was not the case for the high yield strength center-hole case. For the side-hill low yield strength case, the residual stresses significantly increased the residual stress.

- A large interference fit (4.5 mils on the radius) decreases the K solutions for the center-hole nozzle, but an intermediate interference fit (2 mil on the radius) has no effect on the K solution.

- The range of operating temperature considered (560 F versus 605 F) did not significantly affect the K-solution for the center-hole nozzle. (Temperature affects the PWSCC crack growth rate, but not the crack-driving force.)

- Due to a sign change in the slope of the J gradient through the thickness for the side-hill case, the average J values did not vary significantly with crack angle for half crack angles between 30 and 140 degrees. Note that the crack was centered on the up-hill side for this case.

- The overall center-hole results are consistent with past ORNL and other industry K values.

- Because the crack was perpendicular to the pipe thickness, there was a significant crack-driving force contribution of the Mode II (in-plane sliding) and Mode III (out-of-plane tearing) components relative to the Mode I (crack-opening) loading. Hence, it is expected that the cracks would actually grow at an angle through the thickness, rather than perpendicular to the nozzle thickness as was modeled in this work.

Acknowledgements

The efforts conducted in this program were sponsored by the U.S.NRC Office of Nuclear Reactor Research. Mr. Wallace Norris is the project monitor. We would like to thank the many other staff of the NRC-RES and NRC-NRR offices for additional support and information needed to conduct these efforts. Additional information was obtained from Ms. Christine King and the MRP/EPRI committee (including Dr. Steve Hunt of Dominion Engineering and Dr. Peter Riccardella of SAI who conducted similar analyses for the EPRI/MRP group). The Framatome Inc. Lynchburg group also assisted in providing some critical design and weld fabrication procedures.

In addition, we would like to thank Mr. Paul Williams and Dr. Richard Bass of ORNL for the complimentary analysis of the effects of single versus multiple holes in an RPV head. Additionally, Dr. Randal Nanstad at ORNL provided the annealed weld metal stress-strain curves at a variety of temperatures and at loading rates comparable to weld solidification loading. Finally, the authors would like to thank Dr. Zhili Feng and Mr. Rick Wolterman for their efforts to this program while employed at Emc^2.

References

1 Z. Feng, X. Wang, C. R. Hubbard, and S. Spooner, "A FE Model For Residual Stresses In Repair Welds," *Residual Stresses in Design, Fabrication, Assessment and Repair,* ASME PVP-Vol.327, 119-125, 1996.

2 Z. Feng, Y. Y. Zhu, T. Zacharia, R. J. Fields, P. C. Brand, H. J. Prask and J. Blackburn, "Modeling And Validation Of Residual Stress Distribution In A HSLA-100 Disk," *Proc. 4th Int. Conf. on Trends in Welding Research,* (eds., H.B. Smartt, J. A. Johnson and S. A. David), ASM International, 105-110, 1995.

3 Y. Shim, Z. Feng, S. Lee, D. S. Kim, and C. L. Tsai, "Determination of Residual Stresses in Thick-section Weldments," *Welding Journal*, 72(9):305s-312s, 1992.

4 B. Taljat, T. Zacharia, X-L. Wang, J. R. Keiser, R. W. Swindeman, Z. Feng, and M. J. Jirinec, "Numerical Analysis of Residual Stress Distribution in Nozzles with Spiral Weld Overlay," *Welding Journal,* 77(8) 328s-335s, 1998.

5 S. S. Babu, B. W. Riemer, M. L. Santella and Z. Feng, "Integrated Thermal-Microstructural Model to Predict the Property Gradients in Resistance Spot Steel Welds," *Sheet Metal Welding Conf. VII*, Paper # 5-3, Detroit, MI, Oct. 13-16, 1998.

6 Z. Feng, and W. Cheng, "Comparison of 2D and 3D Residual Stress Predictions in Girth Welds of Pipes," 80th AWS Annual Convention, St. Louis, April 12-15, 1999.

7 Z. Feng, R. A. White, E. Willis, and H. D. Solomon, “Development of Compressive Residual Stresses in Underwater PTA Welds,” *9th Int. Symp. On Environmental Degradation of Materials in Nuclear Power Systems — Water Reactors*, (Ed. F. P. Ford, S. M. Bruemmer, and G. S. Was), TMS, 757-764, 1999.

8 McIlree, A. R. “PWR Materials Reliability Program, Interim Alloy 600 Safety Assessments for US PWR Plants (MRP-44NP) Part 2: Reactor Vessel Top Head Penetrations,” TP-1001491-NP, Part 2, Interim Report, Electric Power Research Institute, May 2001.

9 Preliminary Staff Technical Assessment For Pressurized Water Reactor Vessel Head Penetration Nozzles Associated With NRC Bulletin 2001-01, "Circumferential Cracking Of Reactor Pressure Vessel Head Penetration Nozzles," November 2001.

10 Riccardella, P.C., “Probabilistic Fracture Analysis of CRDM Nozzles,” Presentation given at NRCRES-MRP Alloy 600 Meeting, Washington DC, May 22, 2002.

Welding Residual and Operating Stress Analysis of RPV Top and Bottom Head Nozzles

J. Broussard and D. Gross
Dominion Engineering, Inc., Reston, VA

Abstract: Residual stresses due to welding in RPV top head nozzle penetrations have been predicted using finite element analysis since the early 1990's. While the analyses were originally targeted at calculating nozzle stresses, the finite element methods have been extended to model a number of different aspects of RPV head penetrations. Both top and bottom head penetrations have been modeled, and the effects of J-groove butter weld deposition and subsequent thermal stress relief of the top head are now included in the analytical model. Development work has recently been completed to integrate a fracture mechanics model into the welding residual stress model. This has allowed for the prediction of crack tip stress intensities in the presence of welding residual stresses that include the effects of stress relaxation and redistribution due to the presence of the crack. This paper presents some of the modeling techniques used in these recent analyses, and some key results obtained.

DEVELOPMENT OF RPV HEAD STRESS ANALYSIS MODEL

DEI has been developing and refining welding residual and operating stress models since the early 1990s. As shown in Figure 1, the models were originally developed for analysis of pressurizer heater sleeve PWSCC. The model was applied to CRDM nozzles in 1991 after leaks were discovered at Bugey 3. In 1994, EPRI report TR-103696, *PWSCC of Alloy 600 Materials in PWR Primary System Penetrations*, included a description of the models and initial validation efforts. The model was further refined during the 1997-2003 time frame and used for analysis of specific nozzles and for parametric industry group studies. At present, the model has been expanded to a number of new applications, including:

- Input to root cause failure analysis of CRDM nozzles, pressurizer heater sleeves.
- Analysis of repairs.
- Analyses of RPV bottom mounted instrument nozzles.
- Analyses to determine stress intensity factors for use in fracture mechanics analyses.
- Transient analyses for input to fatigue calculations.
- Inputs to strategic planning models.

MODEL DESCRIPTION AND VALIDATION

The welding residual stress models have been developed using ANSYS software. Figure 2 shows a typical CRDM nozzle model. The geometries include factors such as the nozzle, interference or clearance fit of the nozzle in the vessel, counterbores at the top and/or bottom of the interference fit region, weld buttering, and the J-groove weld. The models are developed using parametric input parameters to allow different configurations to be developed efficiently. The need for parametric inputs is illustrated by Figure 3 which shows the range of weld cross section areas encountered in CRDM nozzles.

Multi-pass welding is analyzed using a stepwise approach. Each welding pass is added sequentially using the ANSYS element birth feature. After adding the material a thermal analysis is performed to determine the temperatures in the weld metal and adjacent base metal as the weld cools. The thermal analysis results are used as input to the structural analysis where the weld shrinks and gains strength as it cools. The Alloy 600 nozzle is assumed to have strain hardening properties while the weld is assumed to be elastic-perfectly plastic. All analyses are performed using temperature dependent material properties.

A typical analysis consists of several load steps, including:

- Deposition and stress relief of the buttering material (if used).
- Installation of the nozzle into the vessel with the actual interference or clearance fit.
- Application of the J-groove weld in multiple passes.
- Hydrostatic testing conditions that serve to reduce the peak stresses.
- Operating pressure and temperature conditions.

The model has been validated by several methods. The initial validation work is reported in EPRI report TR-1036596, *PWSCC of Alloy 600 Materials in PWR Primary System Penetrations*. Validations to date include:

- Correlation with measured nozzle lateral deflection and ovality for pressurizer heater sleeves, CRDM nozzles and bottom head instrument nozzles.
- Correlation with reported crack locations and orientations for pressurizer heater sleeves, CRDM nozzles, bottom head instrument nozzles, and pipe butt welds.
- Correlations with x-ray and strain gauge hole drilling residual stress measurements for CRDM nozzle and pressurizer heater sleeve mockups.
- Comparison of material properties and predicted stresses with models prepared by other organizations such as Engineering Mechanics Corporation of Columbus (EMC^2).

ANALYSIS RESULTS FOR RPV TOP HEAD NOZZLES

Figure 4 shows axial and hoop stresses near the J-groove weld on the uphill side of a typical CRDM nozzle. The analyses show that the stresses are higher on the OD of the nozzle than the ID and that the hoop stresses exceed the axial stresses at high stress locations. On this basis, one would expect that the cracking would be predominantly axial and on the OD of the nozzle at the toe of the J-weld. This is consistent with the field inspection results in Table 1 where 60% of the cracks found have been axial and located on the OD of the nozzle near the J-weld. As shown in Table 1, the next most prevalent type of crack has been axial cracks on the ID surface of the nozzle. Again this is consistent with the stress results in Figure 4.

While Figure 3 shows that there is a range of design weld geometries, field inspections by UT have shown that the actual as-built welds can differ significantly in size from the as-designed case. For calculations performed in support of root cause failure analyses, the finite element models are adjusted to represent the as-built geometry. Analysis of actual oversize welds has shown an interesting phenomenon. If the weld extends farther along the nozzle due to a larger size fillet, the stresses at the toe of the weld can be lower than for the as-design case. This results from the fact that high stresses are the result of a J-weld between the nozzle and the rigid vessel head where weld shrinkage pulls the nozzle radially outward creating high stresses. When the fillet extends out along the nozzle, it is not constrained to the same extent by the head thereby resulting in lower stresses at the weld toe.

ANALYSIS MODELS FOR RPV BOTTOM HEAD NOZZLES

Figures 5 and 6 show how the basic finite element model has been modified to represent Westinghouse and B&W design bottom head instrument nozzles. The Westinghouse nozzles are typically welded into the bottom head and stress relieved with the head. The B&W nozzles were originally designed and fabricated with a small diameter extension to the lower internals. However, early flow testing showed excessive vibration and the nozzles were modified by cutting off the small diameter portion inside the vessel head and welding on a larger diameter nozzle. The finite element analysis model shown in Figure 6 includes all of these steps. Analysis results for these nozzles have been used to aid in root cause failure analysis and for strategic planning purpose.

FRACTURE MECHANICS ANALYSIS WITH RELIEF OF WELDING RESIDUAL STRESS

Development work has recently been completed to integrate a fracture mechanics model into the welding residual stress model. The objective of this approach is to be able to account for relaxation of the welding residual stresses as cracks grow in length. Figure 7 shows a typical model with a 180º crack above the J-groove weld and Figure 8 shows the effect of the crack in reducing axial stresses.

The fracture mechanics module calculates the J-integral using numerical volume integration. This approach captures the effects of Modes I, II & III crack opening displacements. The J-integrals are averaged across the nozzle wall and the equivalent stress intensity factor (K) is calculated from the J-integral using the expression:

$$K_{eq} = \sqrt{\frac{J_{avg} E}{1-\upsilon^2}}$$

Figures 9 and 10 show average crack tip stress intensity factors for four elevations relative to the top of the J-groove weld for cracks centered at the downhill and uphill sides of the nozzle respectively. Figures 11 and 12 show a comparison of these predictions relative to other references sources. It should be noted that the results are similar to results obtained by EMC^2, and reported in NUREG/CP-0180.

Since the new module is based on custom software to calculate the J-integral rather than using the ANSYS elements for linear elastic fracture mechanics, test cases were run to validate the J-integral calculation:

- The first validation case was for a circumferential crack in an axially loaded pipe from EPRI report NP-6301-D, *Ductile Fracture Handbook*, (Zahoor). The model for this case is shown in Figure 13 and involved a mean radius to thickness ratio of 10. The analysis results in Table 2 show agreement within 10% between the two models.
- The second validation case was for a through-wall crack in a finite width plate. This model is considered to represent the case of CRDM nozzles without welding residual stresses given the constraint conditions for CRDM nozzles in the head. Figure 14 shows the model for a

center cracked panel from Rook and Cartwright, *Compendium of Stress Intensity Factors*, (Her Majesty’s Stationary Office, London, 1976.) Calculations were performed assuming a large h/b, and the axial stress remote from the crack was calculated assuming the axial pressure loading, including the pressure loading on the crack face. The equations for the crack tip stress intensity factor are:

$$K_0 = \sigma\sqrt{\pi a}$$

$$\frac{K_I}{K_0} = \frac{1 - 0.5\frac{a}{b} + 0.326\left(\frac{a}{b}\right)^2}{\sqrt{1 - \frac{a}{b}}}$$

The results plotted in Figure 14 show good agreement for the case of large flaws where the welding residual stresses have been relaxed by crack growth.

PLANNED FUTURE DEVELOPMENT

The finite element analysis model described in this paper will continue to be used for the purposes described earlier, and will be extended to address issues such as crack opening displacement in the presence of residual stress fields to serve as input to leakage rate calculations. Work is also planned to calculate crack tip stress intensity factors for cracks initiating in J-groove welds. The model will continue to be validated and benchmarked against laboratory and field measurements and analyses performed by others.

Table 1
Correlation of Crack Location and Orientation with FEA Predictions

		No. of Indications on the Nozzle ID	No. of Indications on the Nozzle OD	*Total*
No. of Axial Tube Indications		112	224	*336*
No. of Circumferential Tube Indications	**Above Weld**	0	7	*7*
	Weld Elevation	0	12	*12*
	Below Weld	6	10	*16*
	Total	*118*	*253*	*371*

Notes
1. 498 Indications in the Database (as of 09/2003).
2. Craze Cracking/Shallow Cracks are not Included.

		% Indications on the Nozzle ID	% Indications on the Nozzle OD	*Total*
% Axial Tube Indications		30%	60%	*91%*
% Circumferential Tube Indications	**Above Weld**	0%	2%	*2%*
	Weld Elevation	0%	3%	*3%*
	Below Weld	2%	3%	*4%*
	Total	*32%*	*68%*	*100%*

Notes
1. 498 Indications in the Database (as of 09/2003).
2. Craze Cracking/Shallow Cracks are not Included.

Table 2
Comparison of Stress Intensity Factors for Axially Loaded Pipe

Crack Length	K_I Calculated Using Zahoor[1]	K Calculated per FEA Model Test Case
30¯	2.9 ksi√in	2.9 ksi√in
80¯	6.6 ksi√in	7.1 ksi√in
130¯	12.7 ksi√in	13.6 ksi√in
180¯	24.0 ksi√in	26.5 ksi√in

Figure 1
Development of RPV Head Nozzle Stress Analysis Model

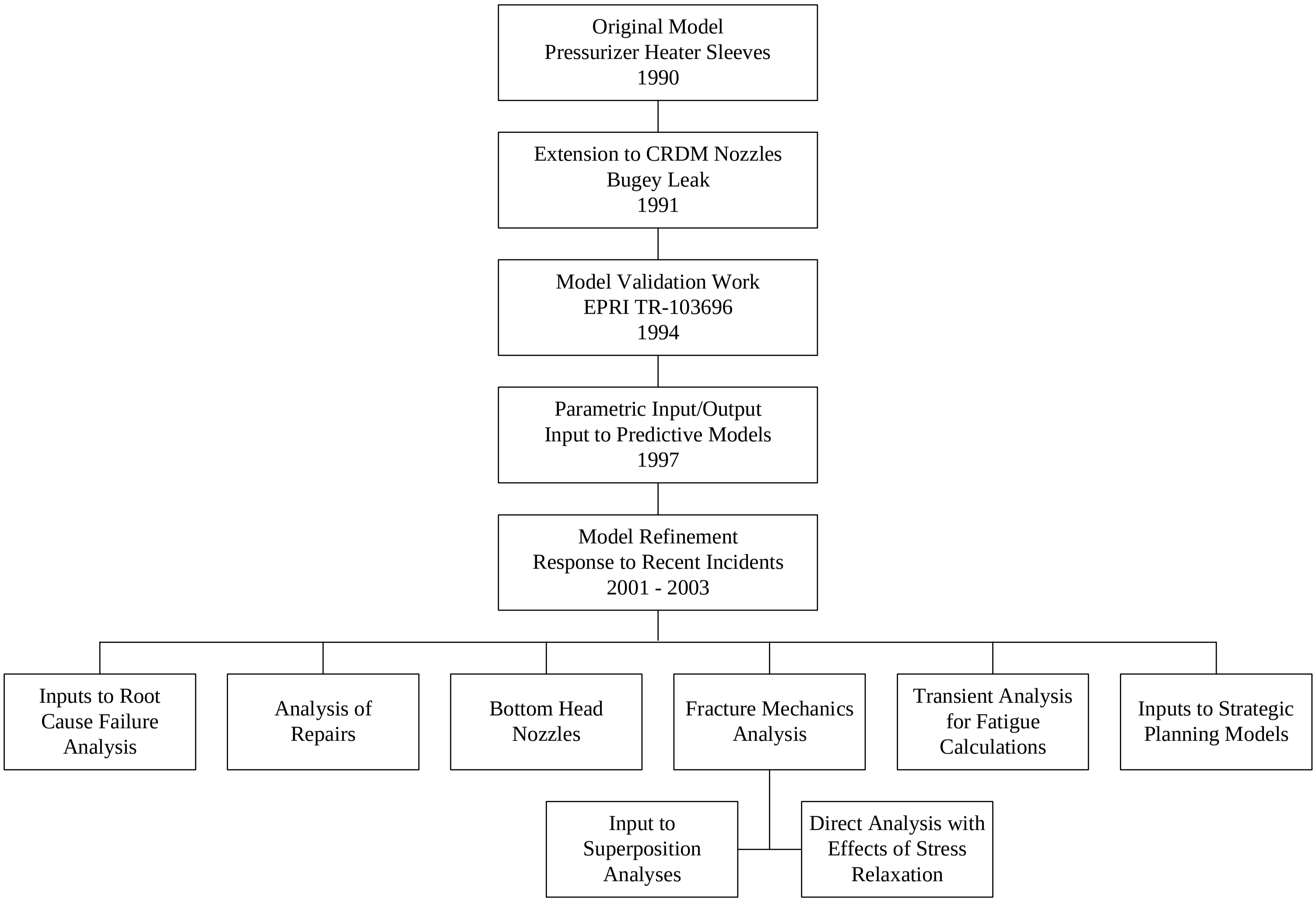

Figure 2
Typical CRDM Nozzle FEA Model

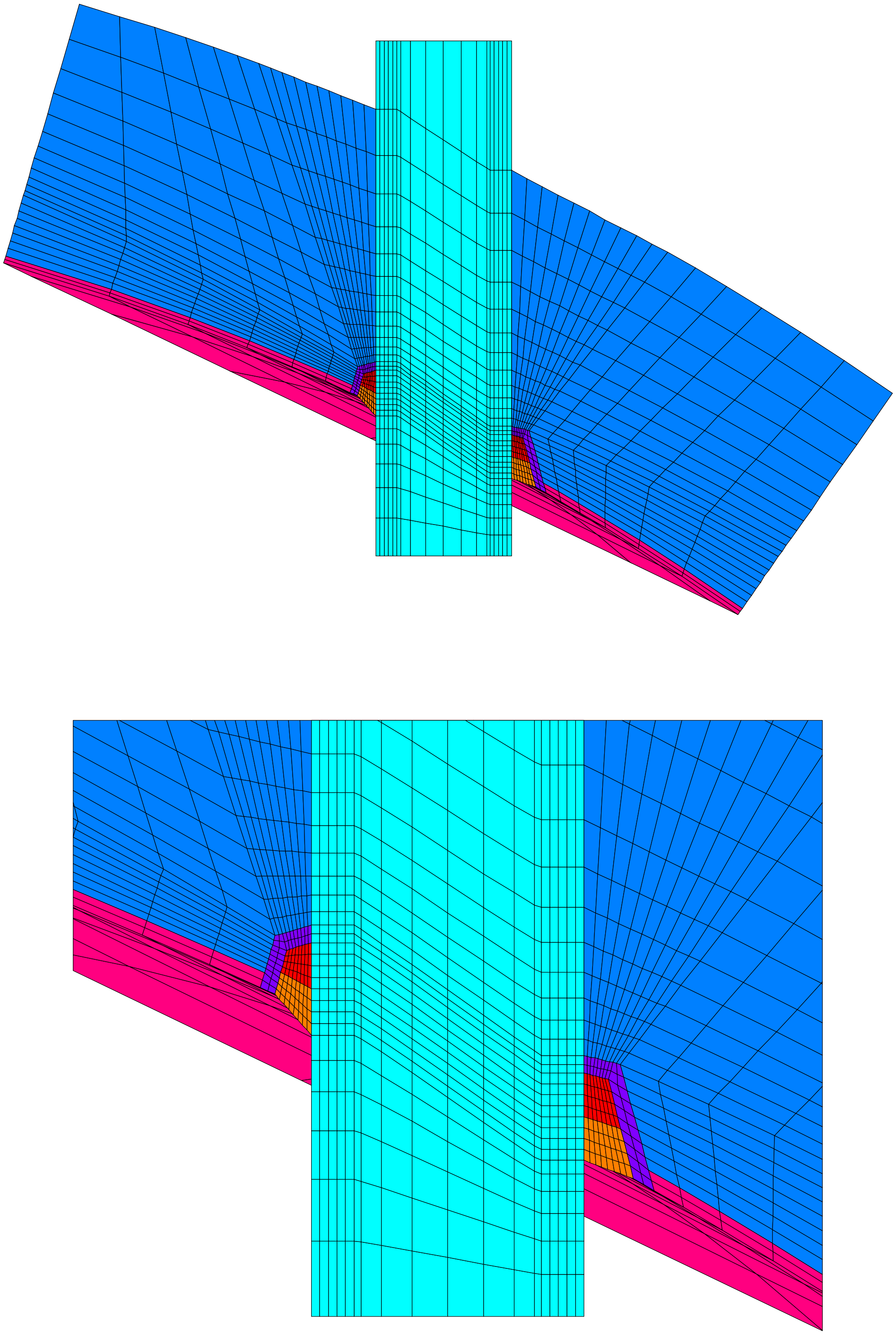

Figure 3
Range of RPV Head CRDM and CEDM Nozzle J-Groove Weld Geometries

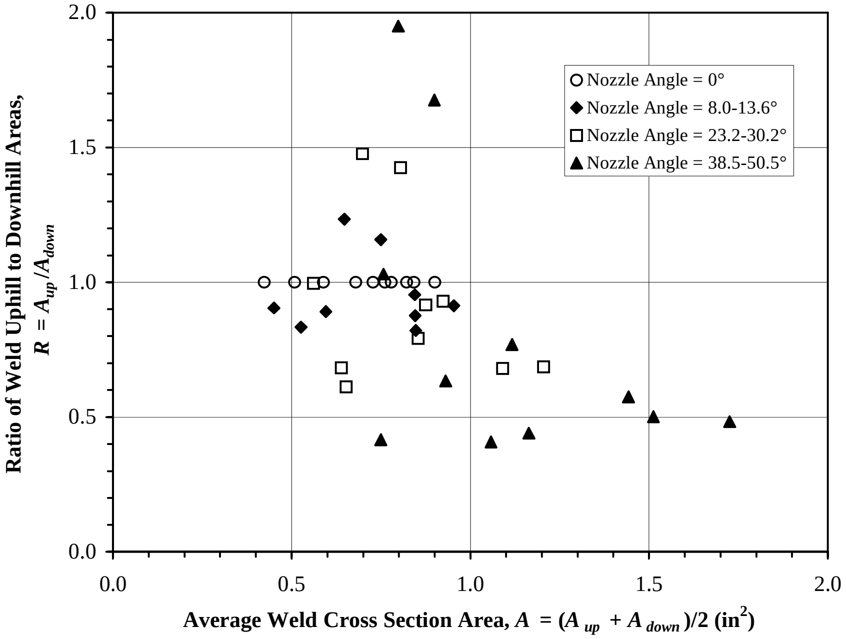

Figure 4
Typical Hoop and Axial Stresses at CRDM Nozzle Uphill Location

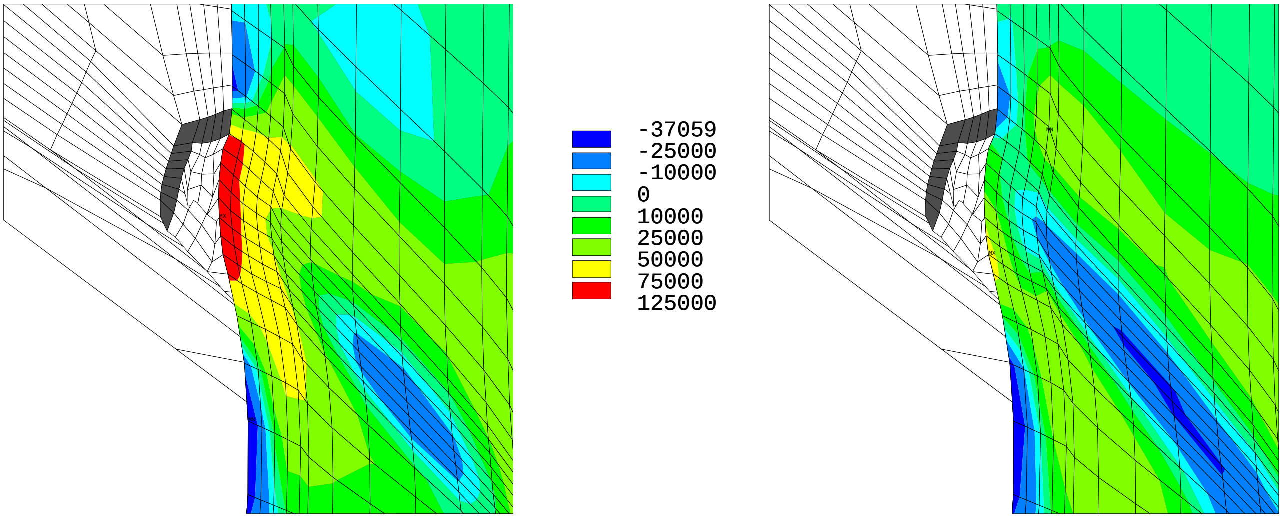

Hoop Stress **Axial Stress**

Figure 5
Typical Westinghouse Design Bottom Mounted Instrument Nozzle

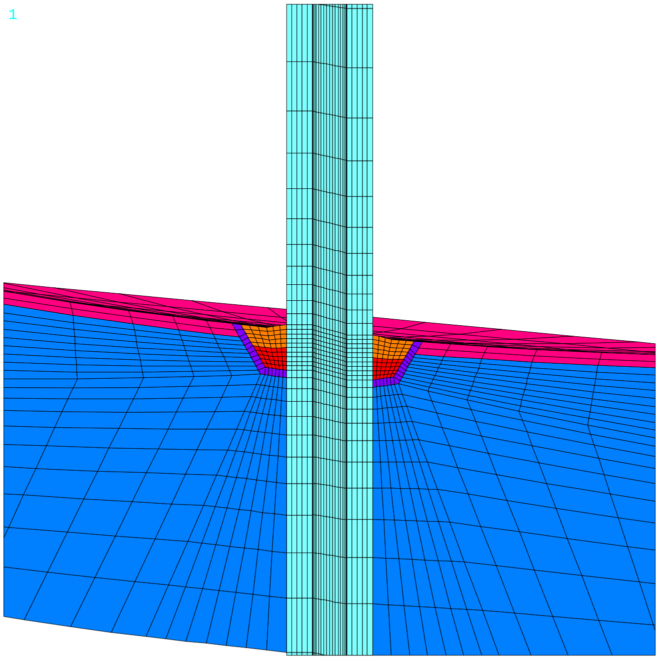

Figure 6
Typical B&W Design Incore Monitoring Instrument Nozzle

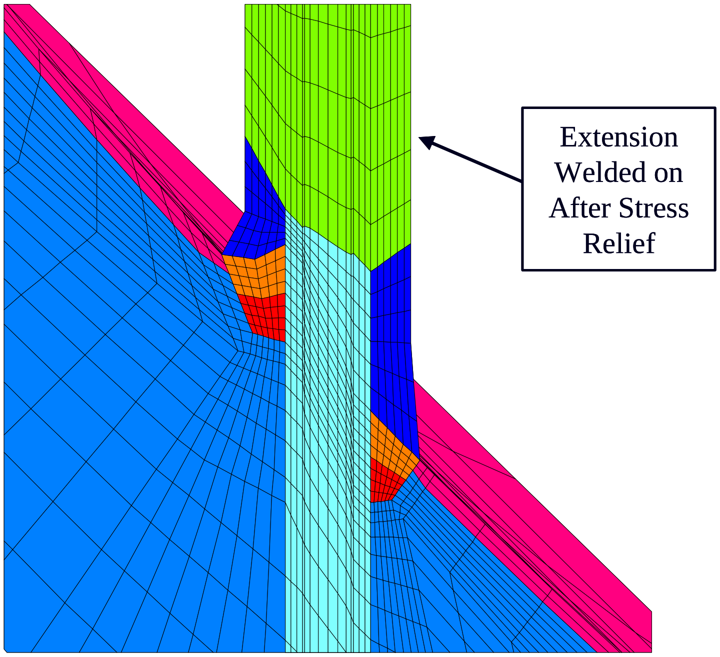

Figure 7
Fracture Mechanics Model

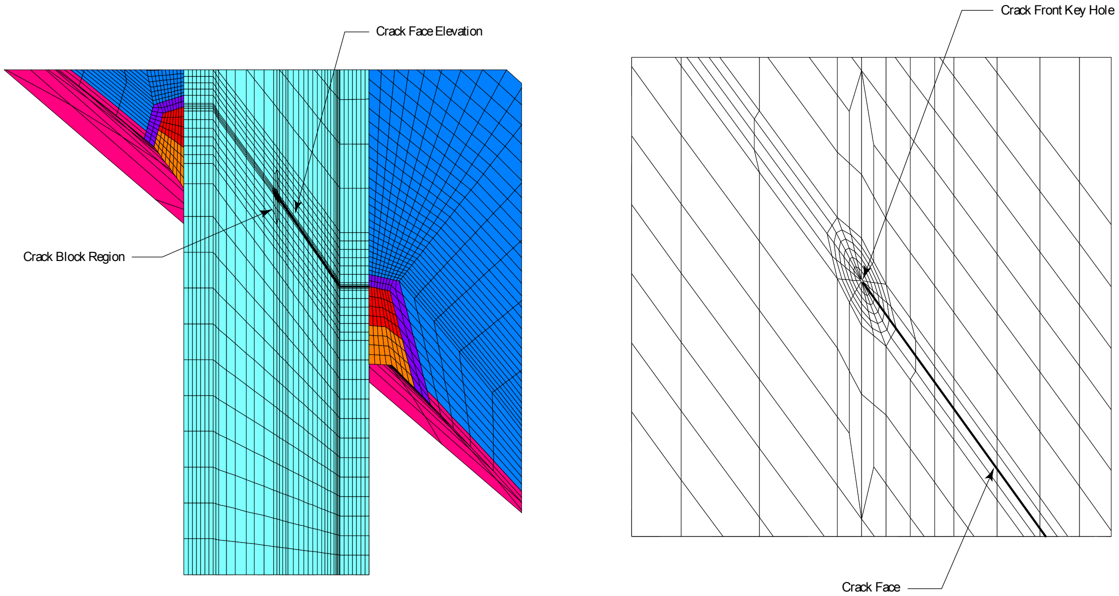

180° Downhill Centered Crack

Crack Mesh Detail

Figure 8
Relief of Axial Stress with Crack Growth for Typical CRDM Nozzle

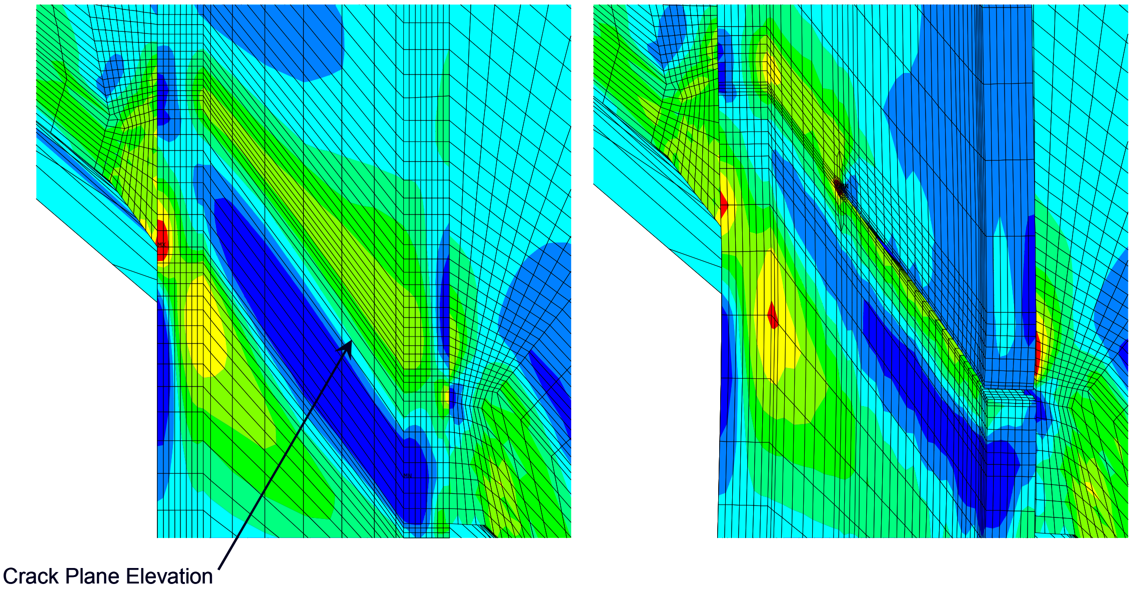

Figure 9
Typical Stress Intensity for Through-Wall Circumferential Cracks – Downhill Centered Cracks

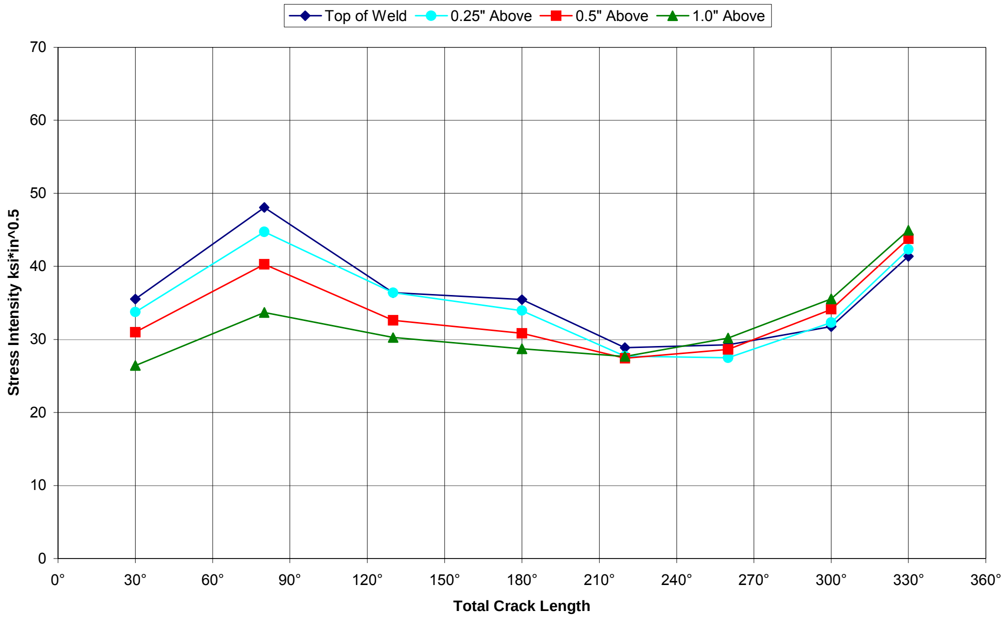

Figure 10
Typical Stress Intensity for Through-Wall Circumferential Cracks – Uphill Centered Cracks

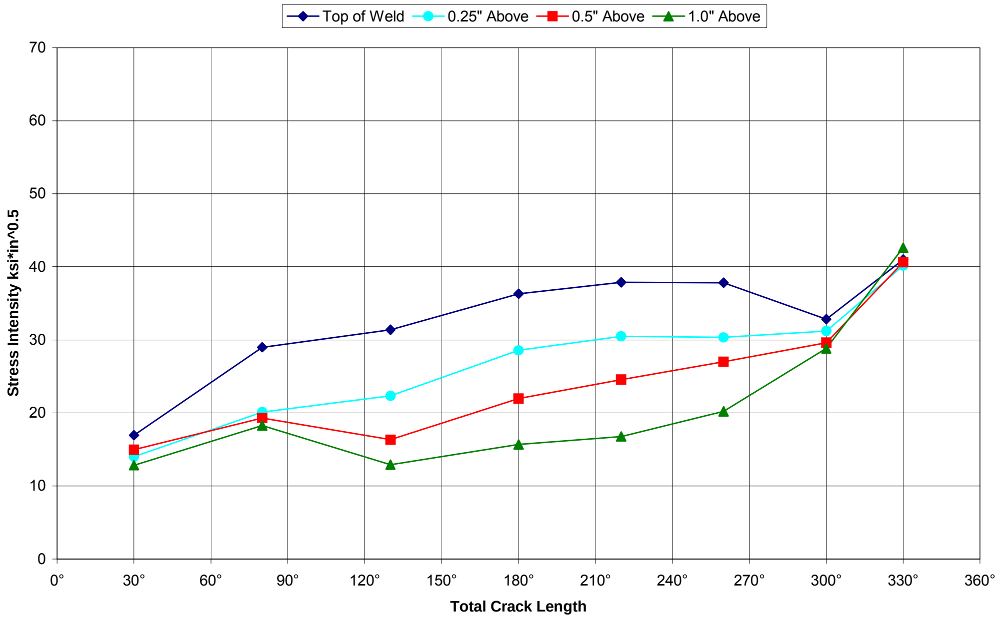

Figure 11
Comparison of Stress Intensity Results – Downhill Centered Cracks

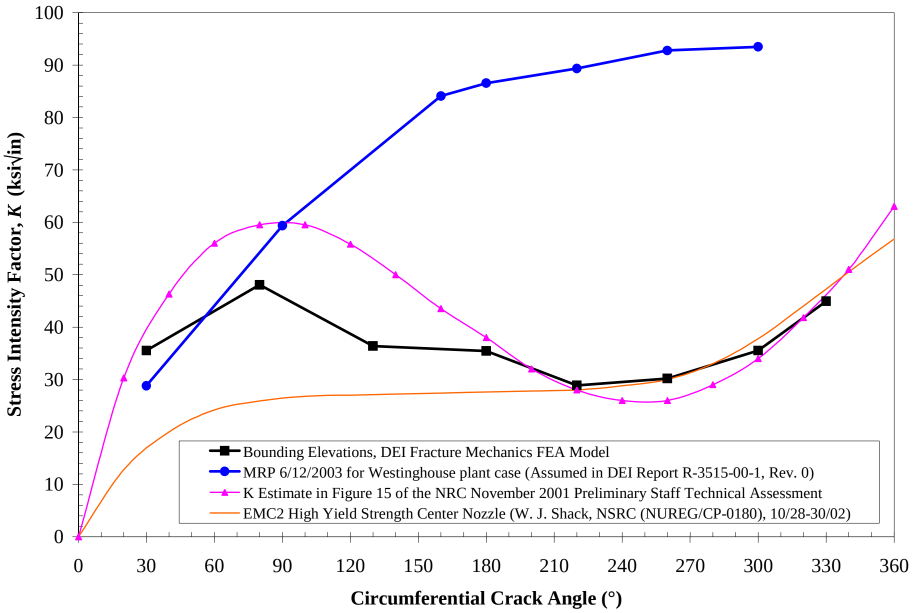

Figure 12
Comparison of Stress Intensity Results – Uphill Centered Cracks

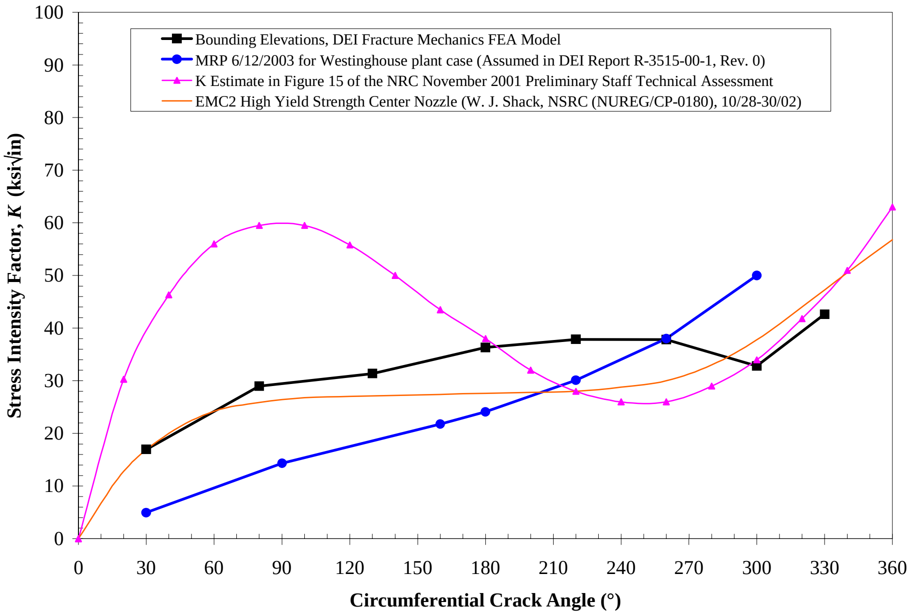

Figure 13
Stress Intensity Model Verification – Pipe with Axial Tension

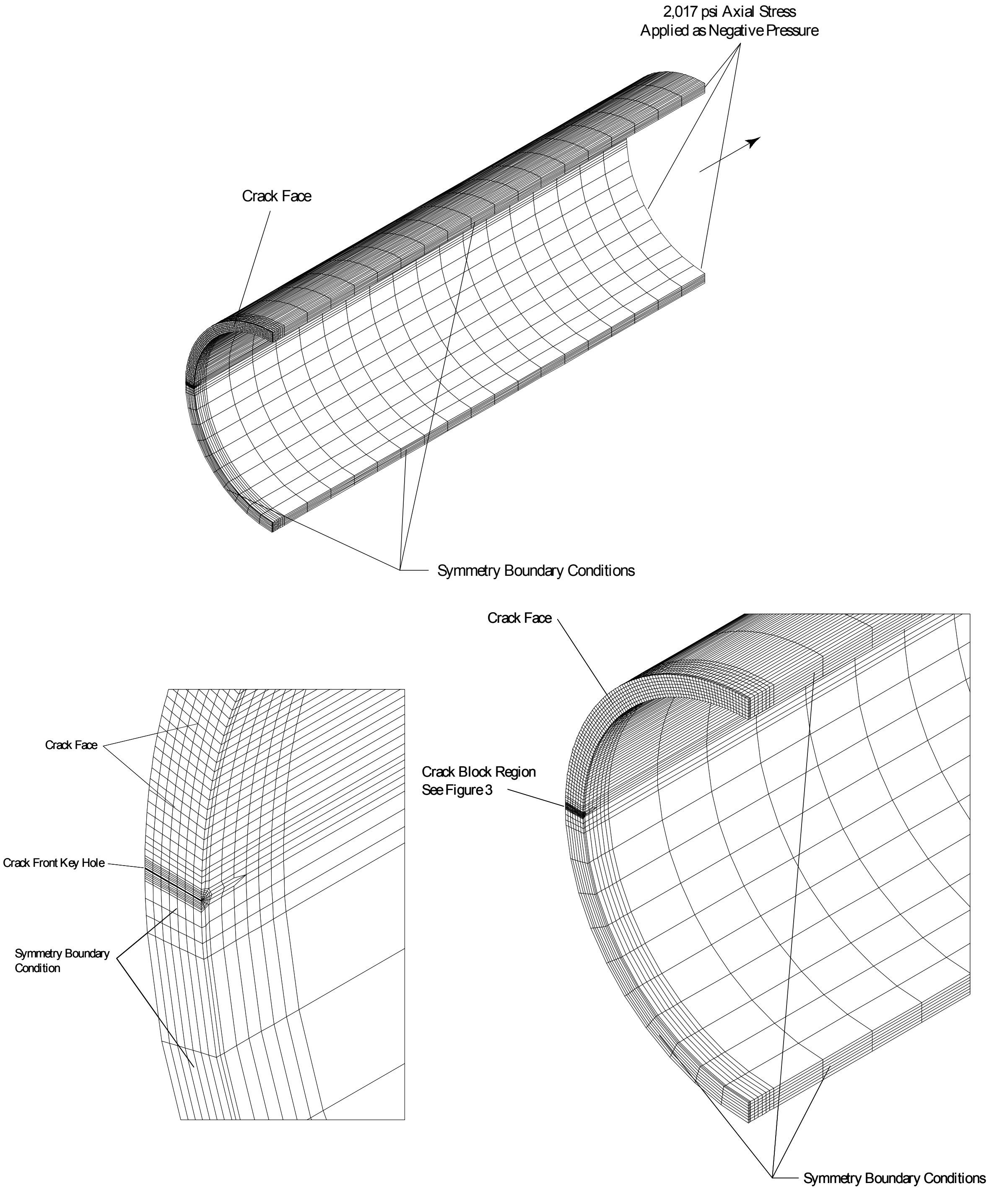

Figure 14
Stress Intensity Model Verification – Through-Wall Center Crack in Plate

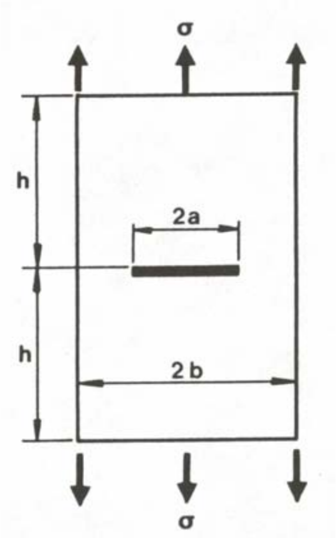

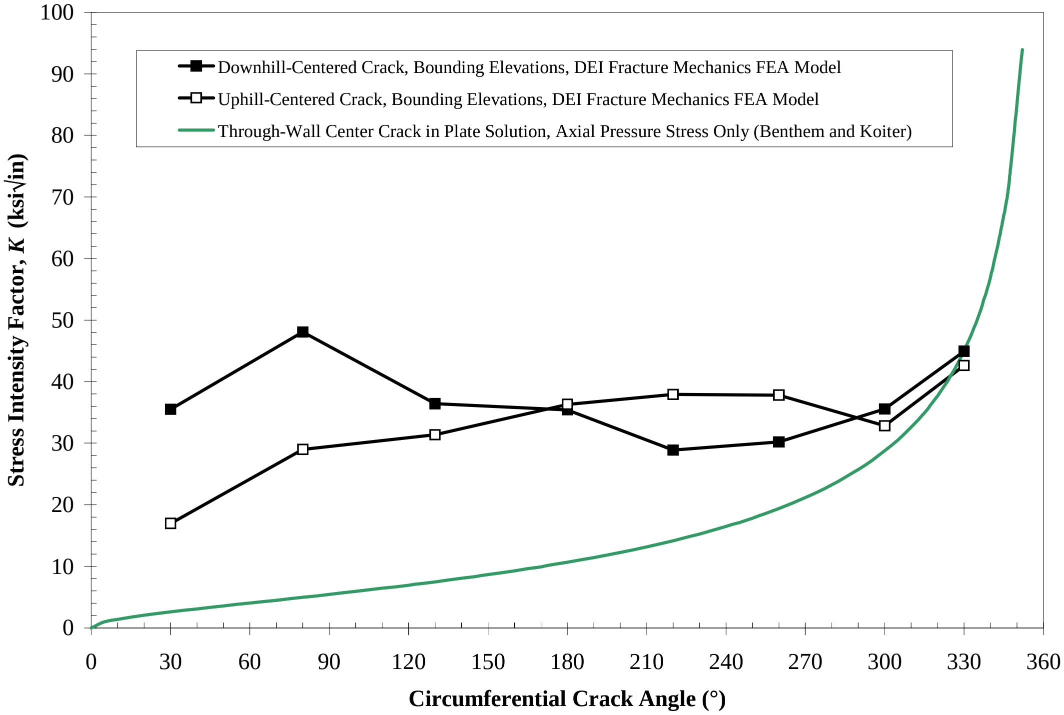

PREDICTING THE FIRST FAILURE

Roger W. Staehle
Adjunct Professor, University of Minnesota
22 Red Fox Road
North Oaks, Minnesota
55127
USA

ABSTRACT

Predicting the earliest failures from a set of components or subcomponents, where these are due to corrosion, is the subject of this discussion. The earliest failures may occur substantially earlier than the mean value. For example, in a heat exchanger with 10,000 tubes the first tube to fail occurs at 1/10,000 or 0.0001 probability. The first tube to fail is important where the loss of fluid or some contamination may significantly contaminate the environment on the other side of the tube. When this first failure occurs relative to the mean depends on the nature of the statistical dispersion of the data. In terms of Weibull statistics the slope of the dispersion of data in linearized coordinates is given by the shape factor (or Weibull slope), β. Typical values for β range from 1.0 to 4.0. At a value of $\beta = 4.0$ the first failure in 10,000 occurs about an order of magnitude in time earlier than the mean. At a value of $\beta = 1.0$ the first failure in 10,000 elements occurs about 10^{-4} of the time of the mean; this means that the first failure would occur in about half a day for a mean time-to-failure of 10 years. Thus, such an early failure would not be due to a bad heat or operator error. It would be part of the natural statistical processes by which failures occur. What value of β applies depends on the nature of the failure process. If the failure process is dominated by surface processes, β tends to be near unity. If the failure process is dominated by the accumulation of reactants or the diffusion or migration of species, the β will be greater than unity and may be in the range of 4.0. Thus, the physical process that controls the damage tends to control the dispersion of data. Complexities associated with calculations and associated micro-processes are discussed. Factors affecting the dispersion of data are identified and described.

INTRODUCTION

The purpose of this discussion is to identify characteristics and an approach to assessing the occurrences of the first and early failures in components and subcomponents. This discussion is concerned mainly with failures that occur by corrosion, but the ideas are broadly applicable.

The approach, which is described here, is based on a framework that uses a standard statistical distribution together with evaluating its parameters with knowable dependencies on primary variables such as temperature and stress.[1,2,3,4,5,6,7,8] This approach illustrates the credibility of failures that occur much earlier than the mean time to failure. It also emphasizes that a dispersion of failure data is inherent even with the best controlled materials and conditions of experiments. This approach does not involve developing a quantitative expression for the dispersion of data from first principles. Such an approach has never been achieved for any application, and the complexity of such an approach may not justify the investment. Using an empirical approach, as described, here provides adequate credibility and is more efficient.

Developing a statistical framework for predicting and organizing data is part of the "corrosion based design approach" (CBDA) that has been extensively discussed.[5] The subject of statistical definition is one step in the CBDA.

The terms, "component" and "subcomponent," as used here refer, for example, to a turbine and its blades, a steam generator and its tubes, or a car motor and its valves.

Failures of multiple components or subcomponents never occur at the same time; they occur over time. These failures are said, then, to be distributed. On the other hand, results from experimental work to characterize the performance of these components are usually measured as a mean or average value. A mean value of the time-to-fail for some material or component is often thought to be some kind of characteristic of the design life. Often, to account for early failures, it is customary to draw an envelope around data and assume that this accounts for the range of failures. If the mean value of data is used for prediction, then it implies that the application is satisfied with 50% of the components failing. If the envelope approach is used based on some limited number of specimens, then there is little insight to the circumstances for occurrences of early failures.

Of greatest interest is not when 50% of elements occur; rather, of greatest interest is when the first failures occur. When does the first tube fail? When does the first turbine blade fail? When does the first leak occur? Answering such questions and identifying such objectives as well as developing an approach to understand and predict first failures is the main topic of this discussion.

Most often, when failures occur early, i.e. earlier than predicted by testing that produces mean values, they are ascribed to “bad heats,” “defective materials,” “sloppy workmanship,” “impurities in the environment,” or “operator error.” Such explanations are rarely the correct interpretation. More often, early failures are the natural result of an early statistical occurrence where the early failure is simply part of the expected distribution of failure times in a set of components or subcomponents.

Interest in first failures also comes from those who think that properly repeated experiments should give the same answer. In fact, the results from testing, even under the most rigorous conditions, inevitably produce variable results. Failure data are inherently variable.

There are inherent complexities in predicting the earliest failures. The main objective here is to emphasize the importance of earliest failures and demonstrate that such predictions are accessible. Complexities include the problems of multiple step processes such as pitting first and SCC second, the stepwise microprocesses involved in modes such as SCC, the integration of initiation and propagation of the modes, the mathematical problems of evaluating the statistical parameters, obtaining numerical expressions for complex contributions such as metallurgical structure, and finally specifying the variability of environments as these need to be inserted into the variables included in statistical parameters. While these complexities need to be acknowledged and ultimately dealt with, identifying the practical reality of first failures and an at least empirical approach to evaluating them provides an important first step as it is described here.

Approaching the question of predicting and understanding the occurrence of the first failure requires understanding the framework in which the first failures can be understood. For this purpose the use of Weibull statistics is discussed first. The next step is relating the statistical parameters, the space, shape, and location parameters, to the primary variables of pH, potential, species, alloy composition, alloy structure, temperature and stress. Then the various implications and approaches are discussed.

APPLICATION OF WEIBULL STATISTICS

The application of various statistically-based fitting procedures for modeling failure data has been extensively discussed[9,10,11,12,13] although these methods are not widely used in corrosion. Usually, statistical models are chosen for their goodness of fit, and any one of these distributions is judged to be correct when it gives the best fit usually as judged by a least squares, or similar, criterion. However, for the present purpose of describing the earliest failure, the Weibull statistics usually gives the best fit for corrosion and many data for failure of materials; therefore, the Weibull distribution is used here for illustration. The purpose of this discussion is not to evaluate the best distribution; it is rather to illustrate the problem of early failures.

Important relationships in the Weibull distribution are shown in Eqns. (1) to (7). Eqn. (1) is the probability density function, *f(t)* (pdf); the pdf gives the probability of failure in any time interval, *dt*. Eqns. (2)-(4) describe the cumulative distribution function *F(t)* (cdf) and give the cumulative fraction failed as a function of time. The cdf is the integral from zero to *t* of the pdf, as shown in Eqn. (2) and as evaluated in Eqn. (3). The cdf is most often used in the linearized form shown in Eqn. (4) which results from taking the double logarithm of both sides. The reliability, *R(t)*, shown in Eqn. (5) is the cumulative probability of elements not failing and is 1-*F(t)*. The hazard function, shown in Eqn. (6) and (7) *h(t)*, (hf) is the probability of failure given that no failures have yet occurred. Eqn. (8) gives the total probability taken as the product of the separate cumulative probabilities; Eqn. (8) indicates that the total reliability, $R_T(t)$, is the product of reliabilities of various contributions, $R_i(t)$. Figure 1 illustrates the patterns of the pdf, cdf, and hf as a function of time for various values of the shape parameter, β.

$$f(t) = \left[\frac{\beta}{(\theta - t_o)^{\beta}}\right](t - t_o)^{\beta - 1}\exp\left[-\left(\frac{t - t_o}{\theta - t_o}\right)^{\beta}\right], t > t_o \qquad (1)$$

$$F(t) = P\left\{t' \le t\right\} = \int_0^t f(t)dt \qquad (2)$$

$$F(t) = 1 - \exp\left[-\left(\frac{t - t_o}{\theta - t_o}\right)^{\beta}\right] \qquad (3)$$

$$\ln\left[\ln\left(\frac{1}{1 - F(t)}\right)\right] = \beta\left[\ln(t - t_o) - \ln(\theta - t_o)\right] \qquad (4)$$

$$R(t) = P\left\{t' > t\right\} = \int_t^{\infty} f(t)dt = 1 - F(t) = \exp\left[-\left(\frac{t - t_o}{\theta - t_o}\right)^{\beta}\right] \qquad (5)$$

$$h(t) = \frac{f(t)}{1 - F(t)} \qquad (6)$$

$$h(t) = \left(\frac{\beta}{\theta - t_o}\right)\left(\frac{t - t_o}{\theta - t_o}\right)^{\beta - 1} = \frac{\beta}{(\theta - t_o)^{\beta}}(t - t_o)^{\beta - 1} \qquad (7)$$

$$F_T(t) = 1 - \left[1 - F_1(t)\right]\left[1 - F_2(t)\right] \bullet\bullet\bullet \left[1 - F_n(t)\right] \qquad (8)$$

where:

t = Time
t_o = Location parameter, sometimes called, erroneously, the "initiation time."
θ = Scale parameter or the Weibull characteristic which is evaluated at $t = \theta$ where the probability is 0.632.

β = Shape parameter or often called the “Weibull slope” as is evident when the linearized version in Eqn. (4). β is also called the “dispersion.”
$f(t)$ = Probability density function, pdf
$F(t)$ = Cumulative distribution function, cdf
$F_T(t)$ = Total cumulative probability
$F_i(t)$ = Cumulative probability for the ith element
$R(t)$ = Reliability
$R_T(t)$ = Total reliability
$R_i(t)$ = Reliability of ith element
$h(t)$ = Hazard function

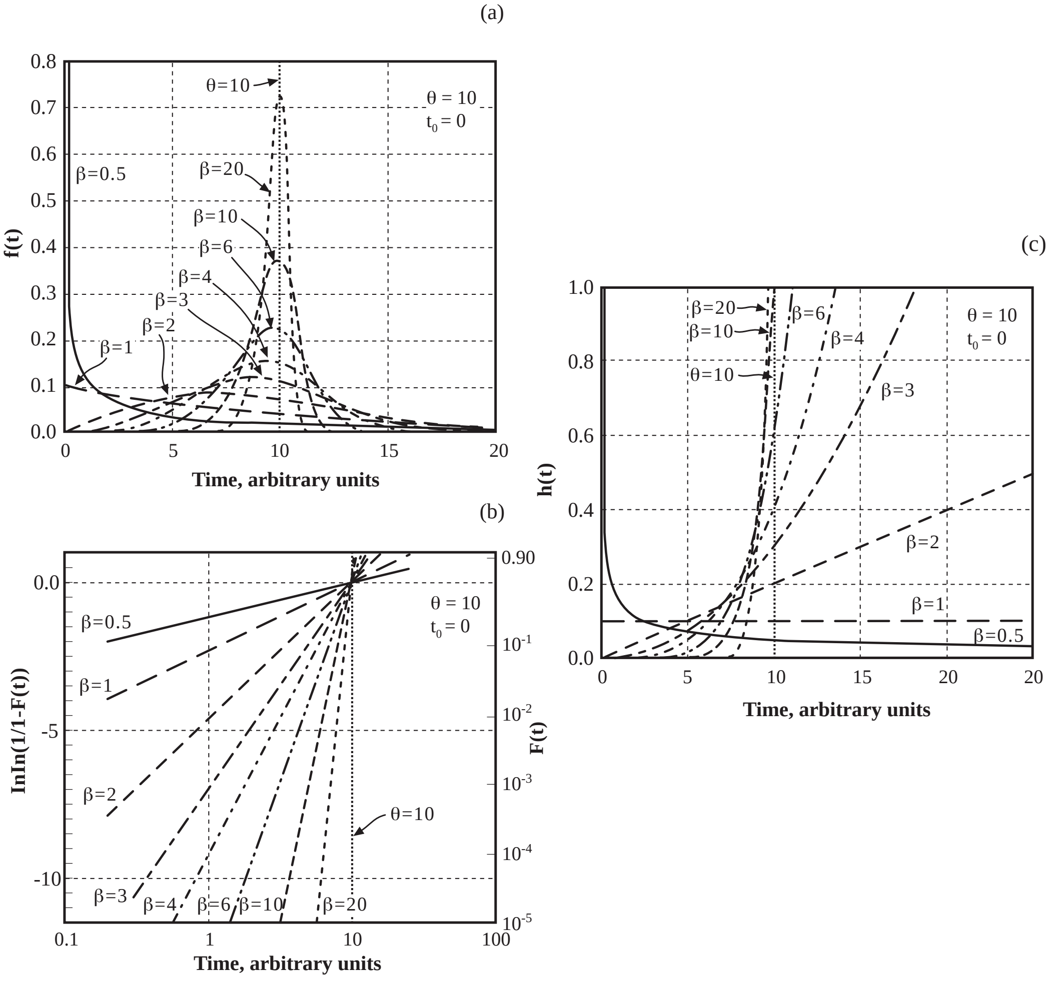

Figure 1 (a) $f(t)$ vs. time for constant θ. (b) F(t) vs. time for constant θ. (c) $h(t)$ vs. time for constant θ.

In the past Eqn. (4) was often evaluated without using t_o and referred to as a "two parameter fit;" however, with the availability of computer programs, such as WinSmith,[14] such simplifications are not necessary.

The significance of the statistical parameters is illustrated with the cdfs plotted in Figure 2a where values of β=1.0 and 4.0 are shown together with selected values, which are shown as dotted horizontal lines, for the probability. A failure probability of 10^{-4} is identified. This corresponds to the failure of one element, e.g. a tube, in a group of 10,000. Such a probability is relevant to heat transfer equipment such as heat exchangers. A failure probability of 10^{-3} is illustrated and corresponds to the first failure in a group of 1000 and might also correspond to a smaller heat exchanger with fewer tubes. A failure probability of 10^{-2}, one in 100 or 1%, is indicated, which may correspond to turbine blades. A failure probability of 10^{-1}, one in 10 or 10%, is often the probability at which a machine, such as a heat exchanger, is replaced since loosing 10% of capacity is not acceptable; whereas, losing the first turbine blade is catastrophic. A failure probability of 0.5 is the mean and corresponds to the average probability of failures such as might be found in a set of experiments. Certainly, failing 50% of any of the elements in operating equipment would hardly be acceptable.

Also, in Figure 2a are drawn two examples of shape parameters, β, with values of 1.0 and 4.0. These are typical of values observed in engineering practice as well as in laboratory experiments and are used here to illustrate some important properties of β. When $\beta = 1.0$ the first failure in 10,000 tubes would occur at about 10^{-4} of the mean time-to-failure. This means that, for a mean time of 10 years, the first failure would occur in about 9 hours. On the other hand, for a β=4.0 the first failure at a probability of 10^{-4} occurs in about 10^{-1} of the mean time, and the first failure in 10,000 elements would occur in about 1 year. Thus, the value of β exerts an important influence on the occurrence of the first failure. Since both of these cases are observed in practical applications, the implications of the value of β is significant to prediction. An essential question here, then, is what controls the value of β. Figure 2b shows the times for first failures with various numbers of elements but with three slopes. Here, again, the importance of the value of β is evident.

The meaning of β is illustrated also in Figure 1c where the hf is shown. When β=1.0, the hf is unity and is independent of time. This means that failure is random in space. When β=1.0, the Weibull expression of Eqn (1) reduces to an exponential function. This result gives the Poisson equation. When β=4 the hf is initially zero and remains low for values to about $\theta/2$ and then hf increases rapidly.

The application of the Weibull distribution to corrosion in water cooled nuclear plants is illustrated in Figures 3 and 4. Figure 3 correlates the results from SCC that have occurred in welds of stainless steel piping in BWR nuclear plants based on the work of Easton and Shusto.[15] Values of β are in the range of unity; and, following the expectation identified in Figure 2, the values of θ are in the range of 5.53×10^6 and 2.6×10^8 hours for large and small pipes, respectively. Figure 4 is based on corrosion that occurs in a steam generator of a PWR.[16] Here, multiple locations of corrosion are identified at each cycle. These individual results are then aggregated according to Eqn. (8) to give values of $F_T(t)$. In general, the average slopes are in the range of β=4.

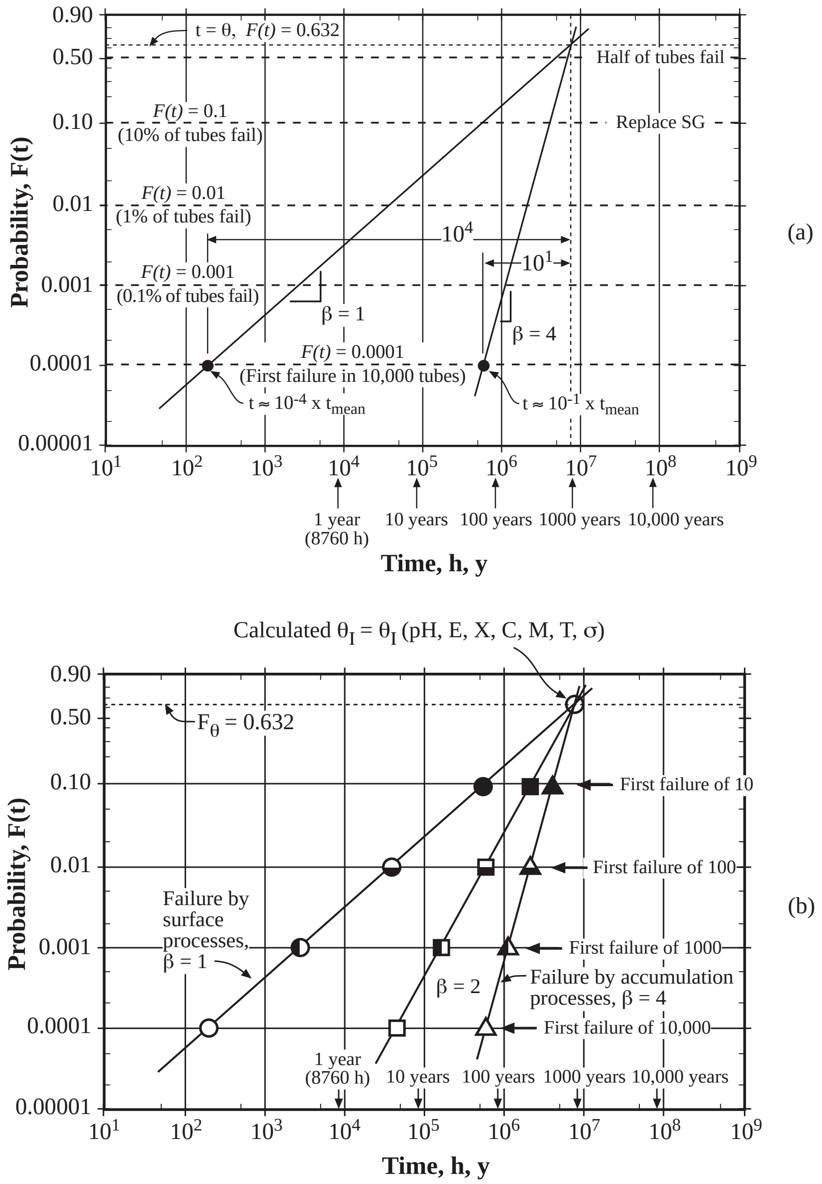

Figure 2 (a) Cumulative distribution function (correlation without physical foundation). (b) Schematic view of probability vs. time for a calculated θ and three options for slopes within the range of engineering experience. Locations of the earliest failures noted for various populations according to the three examples of β.

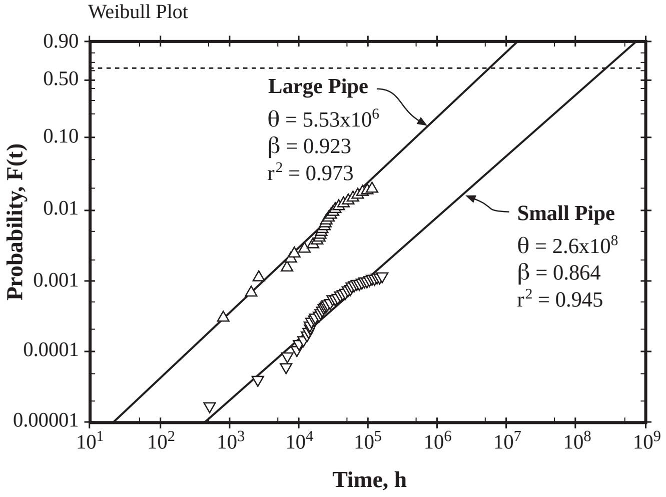

Figure 3 Probability vs. time since startup for SCC failure of welded stainless steel pipes from piping used in boiling water nuclear reactors (BWR). "Large pipe" refers to 4 inch diameter. "Small pipe" refers to 2 inch diameter. From Eason and Shusto.[15]

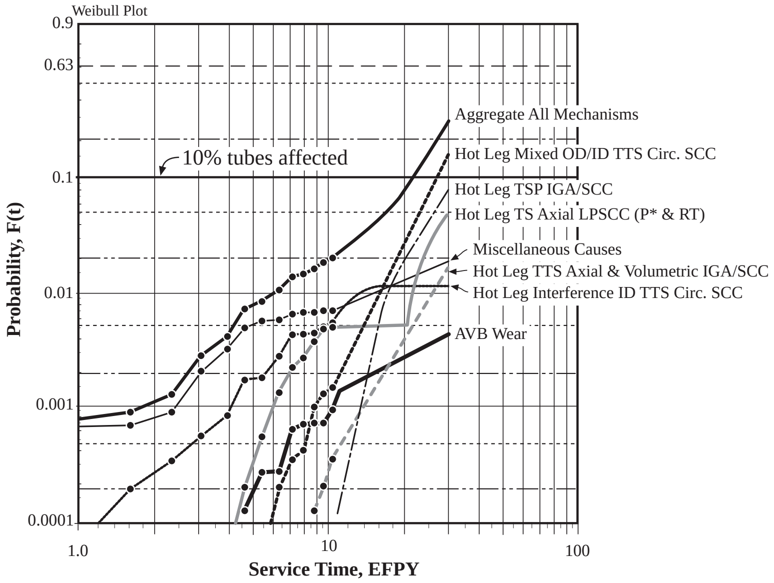

Figure 4 Probability vs. equivalent full power years (EFPY) for failures of tubing from a set of SGs in the Ringhals -4 PWR. Designations: TTS = "top of tube sheet." TS = "tubesheet." Circ. SCC = "circumferential SCC." P* = special location where SCC is not serious. RT = "roll transition." AVB = "antivibration bars".[16]

Akashi and Nakayama[17] have shown for testing of sensitized stainless steel at 30-80°C in multiple experiments the value of *β* tends to be in the range of unity as shown in Figure 5.

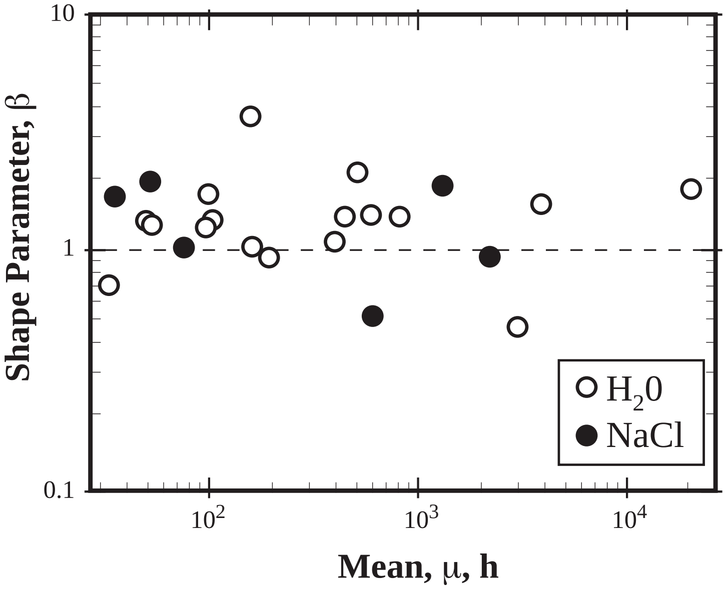

Figure 5 Shape parameter, *β*, vs. mean failure time, μ, in terms of the Weibull distribution for experiments performed in pure water and NaCl solutions using sensitized stainless steel in the presence and absence of surface crevices in the temperature range of 30-80°C. Adapted from Akashi and Nakayama.[17]

Figures 3-5 illustrate practical cases where the values of *β* for many corrosion data occur in the range of 1 to 4.

USUAL APPLICATION OF STATISTICAL CORRELATIONS

Statistical correlations are most often used to characterize a data set or to estimate the future of an emerging data set. For example, in Figure 6 a sequence is shown whereby a first data point is plotted and provides a bases for initial correlations. The slope of possible correlations is based on prior experience. With additional data points as shown in Figure 6b, confidence in the slope increases. At some point, depending on the number of data points and prior experience, as shown in Figure 6c, it is possible to estimate when a failure condition is imminent. For example, in Figure 4, the failure condition occurs at 10% of the tubes plugged. Figure 4 shows that 10% of failures would occur in about 20 years. Thus, there is ample time to prepare for replacing the SG unit.

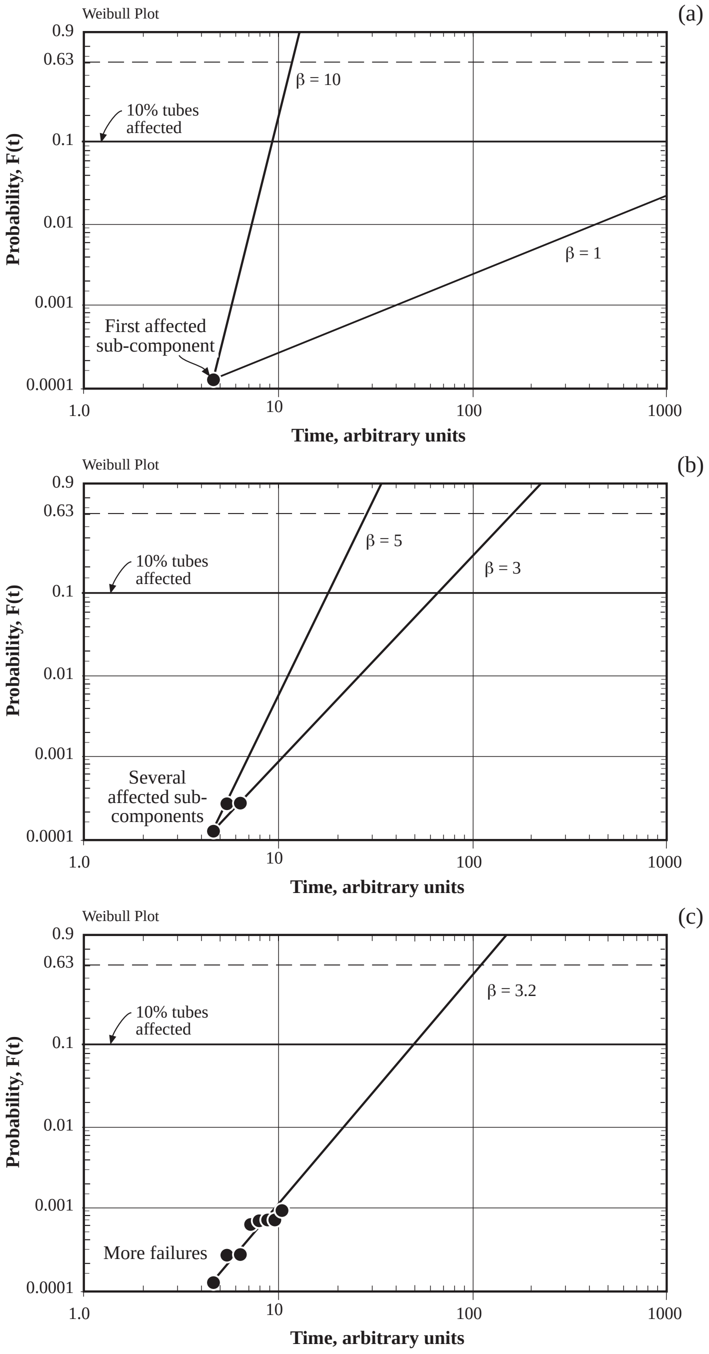

Figure 6 (a), (b), (c) Schematic Weibull plots for cdfs and the evolution of failure points together with expected slopes for prediction.

In the case of the sequence shown in Figure 6 the statistical correlation is used simply to characterize the data and to project forward progressively improved predictions. Slopes are chosen for initial and progressive estimates based on prior experience.

However, the sequence of Figure 6 is not predicting the first occurrence of failure; this sequence is only characterizing data as they evolve. A variety of statistical distributions could be tried here until one provides the best fit to the emerging data. Which distribution is optimum becomes progressively more apparent as additional data are obtained, and the fitting of several possible statistical distributions is examined.

The discussion here is aimed toward predicting the time of the first failure; this is not the same as providing a chronicle of how failures evolve. However, such past data provide useful insights into predicting first failures.

MODES AND SUBMODES: THEIR DEPENDENCIES ON PRIMARY VARIABLES

In this discussion what is to be predicted is the first or early failures of a specific set of modes or submodes of corrosion. For convenience, the occurrence of SCC is used, and Figure 7 illustrates the array of primary submodes of SCC for Alloy 600 in the mill annealed condition (Alloy 600MA). Here, the submodes illustrated are alkaline SCC (AkSCC), low potential SCC (LPSCC), acidic SCC (AcSCC), and high potential SCC (HPSCC). There are other submodes of SCC for Alloy 600MA, but Figure 7 is adequate for this discussion. Figure 4 shows the occurrence of some of these submodes as they occur on primary and secondary sides of a steam generator of a PWR.

As discussed by Staehle[3,4] all submodes of corrosion can be described by the primary variables of potential, pH, species, alloy composition, alloy structure, temperature and stress. The general roles of these primary variables are shown in Figure 8. The general functionality of these primary variables is also illustrated although these details depend on the submode.

Each submode then depends differently on the primary variables. The differences in dependencies among the four submodes in Figure 7 is evident from the well-defined differences in respective locations with respect to pH and potential.

These dependencies of the submodes on primary variables, as indicate briefly in Figure 8 by the vignettes, is clearly based on mean values of data. These are not statistical although some data have been statistically correlated when they were obtained. Such data, by themselves, provide no information on the occurrence of first failures.

It should also be noted that the data obtained for the four submodes and illustrated in Figure 7 relate mostly to initiation processes and not to propagation although for tubes the SCC being described is dominated by initiation.

The problem considered in this discussion is how the data from the seven primary variables can be included in the statistical framework in such a way that the occurrence of first failures can be predicted.

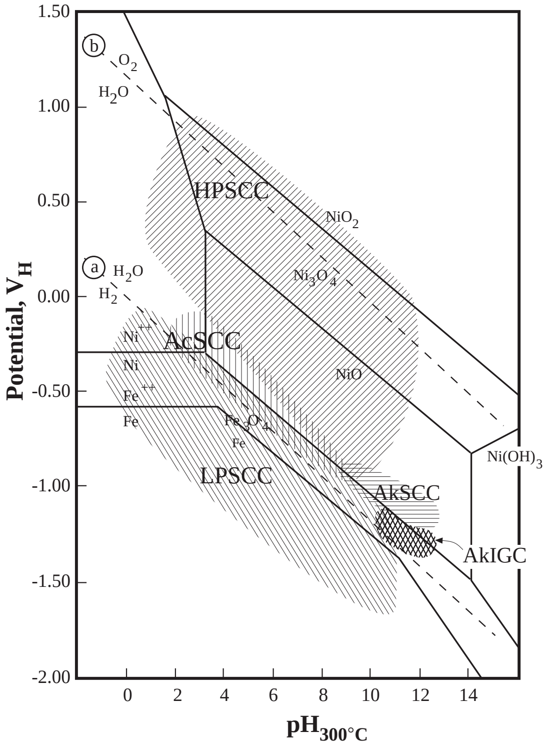

Figure 7 Major submodes of SCC and IGC for Alloy 600 in mill annealed conditions in the range of 280˚to 350C in aqueous solutions. Regions of SCC shown with respect to thermodynamic boundaries for iron and nickel species in water. Regions of SCC submodes shown are based on published experimental data. LPSCC = “low potential SCC.” HPSCC = “high potential SCC,” MA = “mill annealed.” P = “pure water.” C = “contaminated.”

PHYSICAL MEANING OF STATISTICAL PARAMETERS

The primary avenue by which early failures can be predicted involves developing physical meaning for the statistical parameters θ, β, and t_o. This is essentially a correlation approach. However, developing statistical distributions from any kind of approach with first principles to describe the submodes in Figure 7 would not only be exceeding time-consuming but of doubtful validity.

The approach taken here involves two main steps: selecting a statistical distribution and evaluating the statistical parameters with existing correlations for the primary variables. The details of this approach have been described by Staehle.[3,4,6]

There are obvious problems and complexities in the approach describe here; these are identified and acknowledged. However, what is described here are the central ideas and the possibility of predicting early failures.

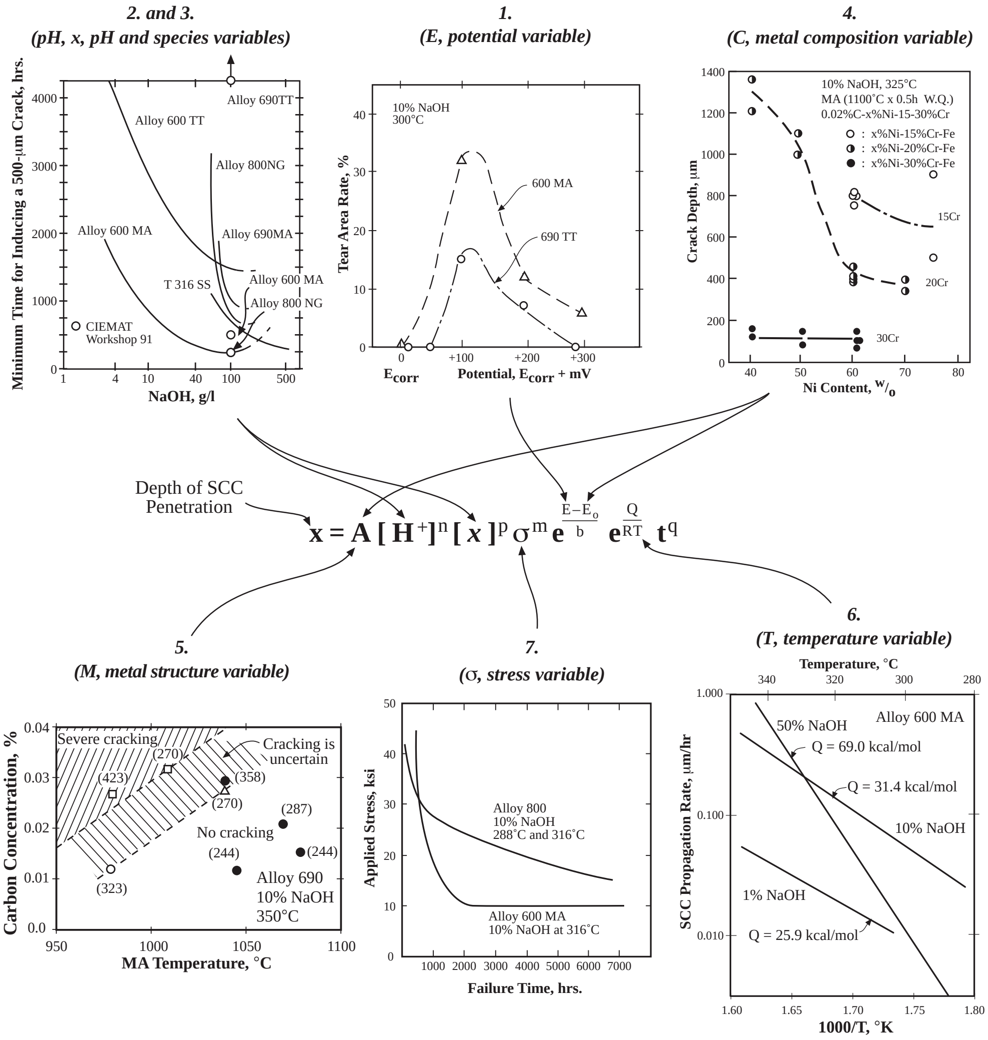

$$x = A\,[H^+]^n\,[x]^p\,\sigma^m\,e^{\frac{E-E_o}{b}}\,e^{\frac{Q}{RT}}\,t^q$$

Figure 8 General relationship of penetration of SCC as a function of primary variables. Examples of patterns for the primary variables from AkSCC are shown adjacent to the equation. (1) From Suzuki.[18] (2 &3) The original curves of Berge and Donati[19] were redrawn, and data were added by McIlree.[20] (4) From Nagano et al.[21] (5) From Vaillant et al.[22] (6) From Jacko.[23] (7) From Wilson et al.[24]

Modeling stepwise processes

Developing statistical models for corrosion processes must consider multiple segments associated in general with initiation and propagation, e.g. for SCC or corrosion fatigue. Figure 9 identifies nine specific segments that have been identified for SCC.[5] To develop a model based on first principles, each of these stages would have to be modeled, and the overall probability of perforation or failure would result from the concatanation of these partial probabilities.

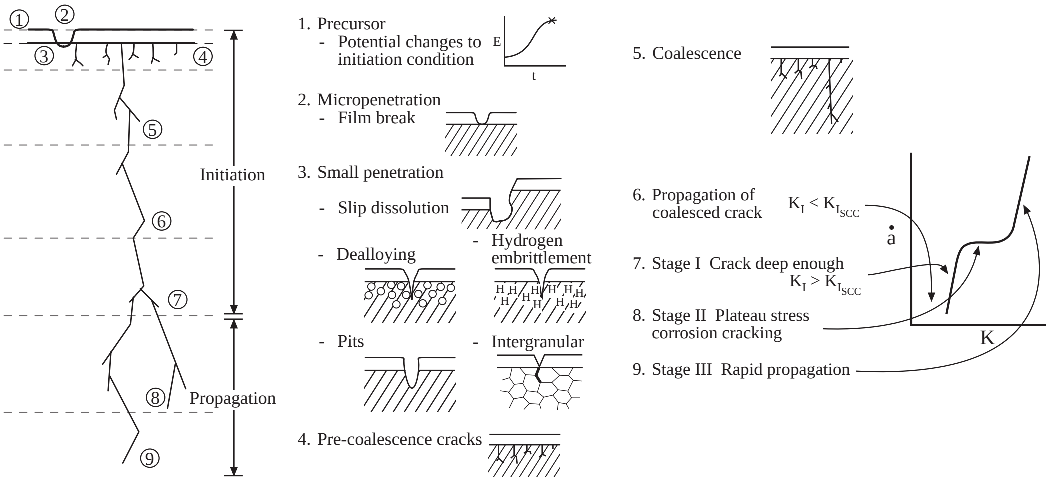

Figure 9 Nine sequential segments of SCC. Practical transition from initiation to propagation shown. Protective film adjusts to the environment.

While a model developed for all the segments in Figure 9 would be rigorous, it may also not be readily achieved. Generally, in considering SCC, it is conventional to consider initiation and propagation processes more generally as shown at the right of the set of segments in Figure 9. While these two stages include substages and thus are not physically explicit, two segments are about as much as can be handled in modeling. Further, broadly, initiation and propagation have characteristics that permit integration on a practical scale.

The fact that initiation and propagation can be integrated as well as considered separately is shown in Figure 10. Here, the experimental bases for the two stages are shown. Experiments to quantify initiation usually utilize statically loaded specimens with smooth surfaces. Data from these experiments produces a threshold stress as shown in Figure 10a. Data from pre-cracked specimens produce a $K_{I_{SCC}}$ as shown in Figure 10b. Threshold stresses from studies of initiation plot in Figure 10c as horizontal lines, and the locus of points for $K_{I_{SCC}}$ plot as lines with a –1/2 slope. The intersection of these lines identifies that transition between initiation and propagation. For example, a threshold stress of 100 MPa and a $K_{I_{SCC}}$ of 5 MPa m$^{1/2}$ intersect at about 800 μm, and this marks the transition from initiation and propagation.

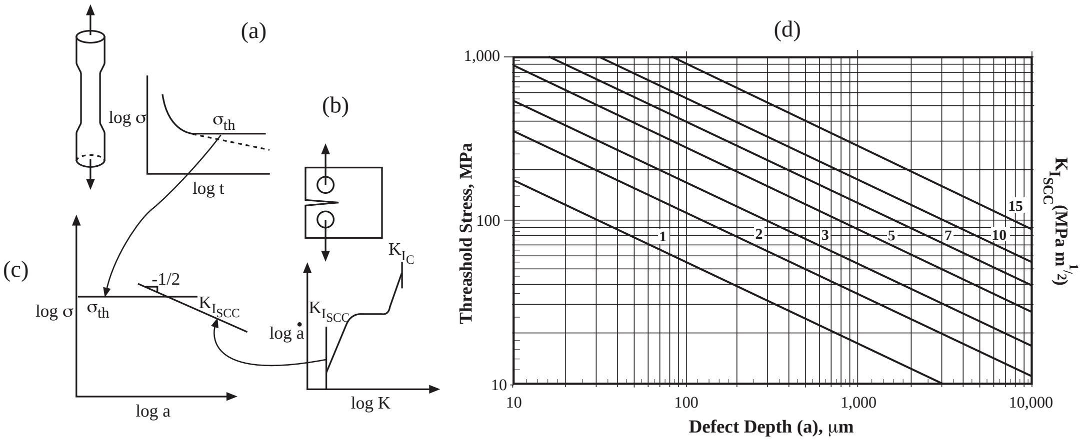

Figure 10 (a) Method for determining the dependence of initiation vs. stress. (b) Method for determining the value of $K_{I_{SCC}}$ involving crack velocity and stress intensity. (c) Schematic integration of (a) and (b). (d) Quantitative matrix for determining depth at which the transition from initiation to propagation occurs.

To develop a reasonable prediction for the first failure, it would be necessary to develop expressions for both initiation and propagation. Such a complexity is not described here.

Developing a quantitative expression for corrosion fatigue might follow a similar pattern as that associated with Figure 9. Perhaps, in some cases pitting may be more dominant in the early stages. This pitting would also have to be modeled in a statistical format.

Metallurgical variability

Illustrative of the variability of alloys are the data in Figure 11 from Scott.[25] The bars in this figure correspond to successive heats of Alloy 600MA produced at the same site at consecutive times. Thus, data from Figure 11a refer to failures that occurred on the primary side, presumably via LSPCC; the data in Figure 11b refer to failures on the secondary side that probably occurred as a result of several different submodes. The heights of the bars indicate the fraction of tubes from each heat that sustained damage. The number at the top of each bar shows the number of tubes from that heat used in the respective steam generators.

Despite the similarities in the history of the tubes, i.e. the same bulk environments in the SGs and the same source of the heats, large variability in the performance of the tubes is observed. In some cases no failures occurred and in others 5-40% of the tubes failed. There is no explanation for such variability.

Environmental Variability

The general equation for SCC shown in Figure 8 describes the dependencies of submodes on the seven primary variables. However, these variables, themselves, are distributed and sometimes not readily knowable. How they should enter an expression for describing first failures is not clear. For example, temperature is often readily measurable and may occur over a relatively narrow but distributed range. Stress is less knowable, especially at a surface that contacts the external but local environment. Stress is certainly broadly distributed.

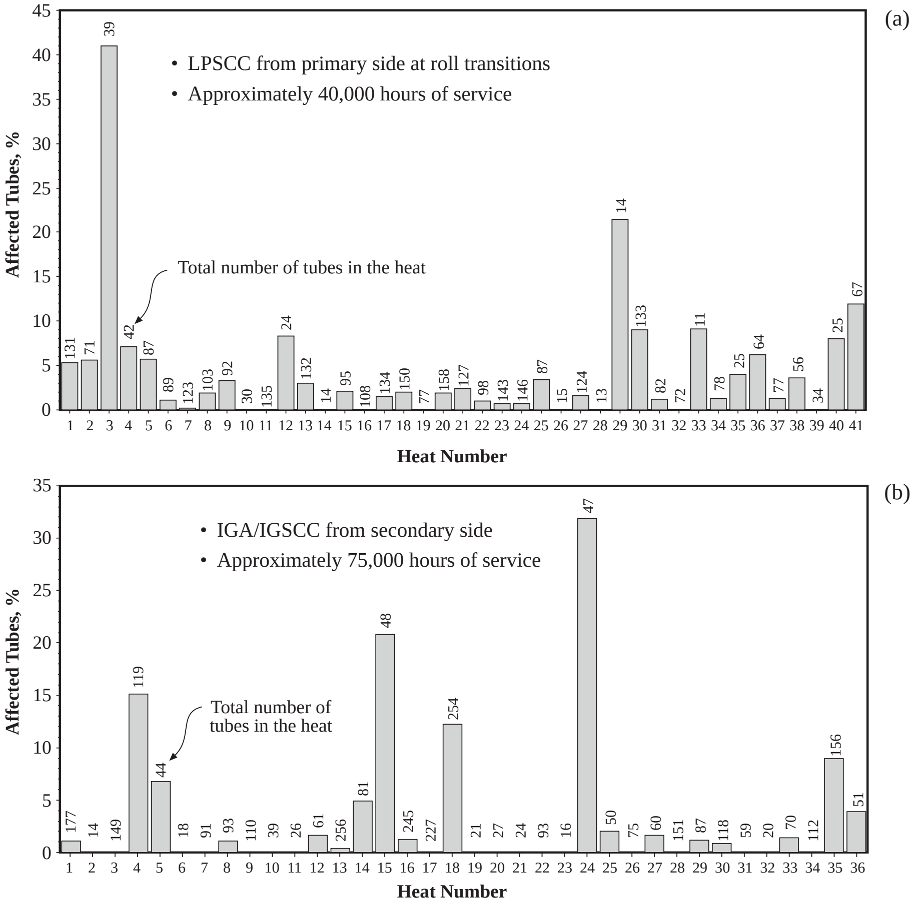

Figure 11 (a) Percent of tubes affected by LPSCC from the primary side of a PWR steam generator vs. heat number determined at roll transitions after approximately 40,000 hours of service. Primary surface temperature at this location is about 310°C. Environment is primary water as identified in Figure 4. (b) Percent of tubes affected by IGA and IGSCC vs. heat number from the secondary side of a PWR steam generator in heat transfer crevices after approximately 75,000 hours of service. Adapted from Scott.[25]

The main chemical variables of pH, potential, and species are unquestionably distributed, and also not readily knowable. For example, Figure 12 shows the state of environments inside a heated crevice from a tube support of a steam generator from a pressurized water nuclear reactor. This is a complex and dynamic system. Despite about thirty years of work, there is no quantitative model nor empirical definition of the species that occur on surfaces. A more detailed view of this condition based on direct observation is shown in Figure 13,[27] which shows the distribution of species and compounds in one of these crevices after a tube was removed from a heated crevice. Qualitatively, it is clear that the localized environment that occurs on the surface of the adjacent tube cannot be readily predicted.

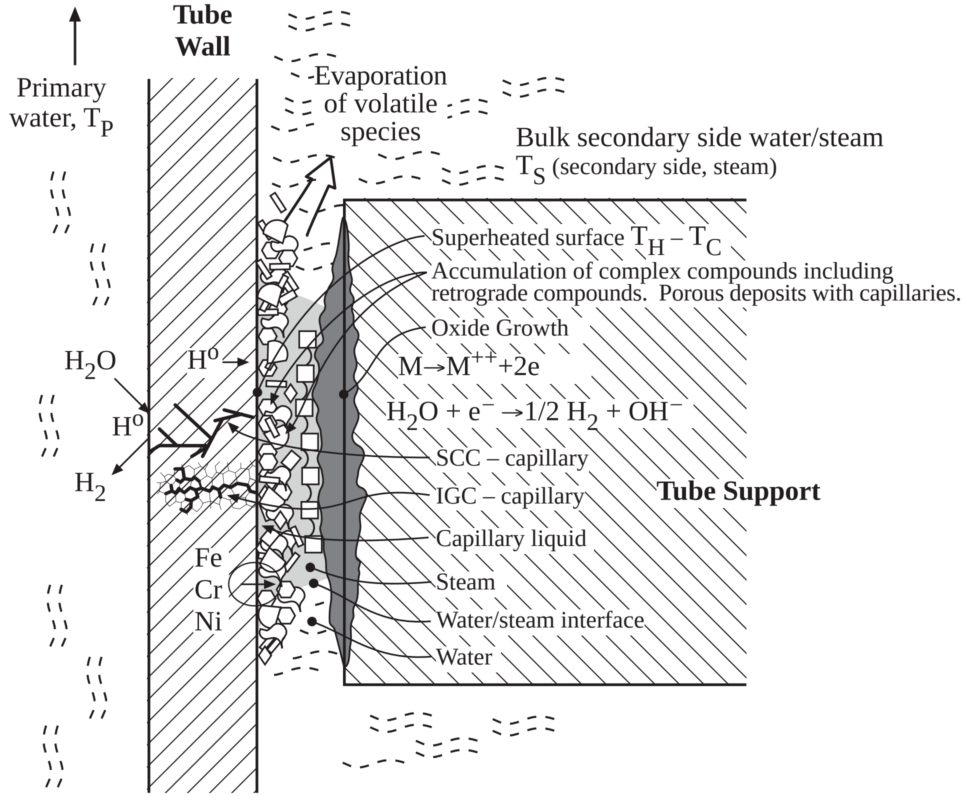

Figure 12 Schematic view of heat transfer crevice at a tube support. From Staehle.[5]

Defining the local environment that actually produces corrosion is not often approached aside from the problem of specifying its distributed nature. Often, many engineers assume that the local environment on surfaces is the same as the bulk environment, a judgment that is not supported by the observations in Figures 12 and 13. The general problem of specifying environments is discussed by Staehle.[5,26] The properties of local environments on surfaces also change with time.

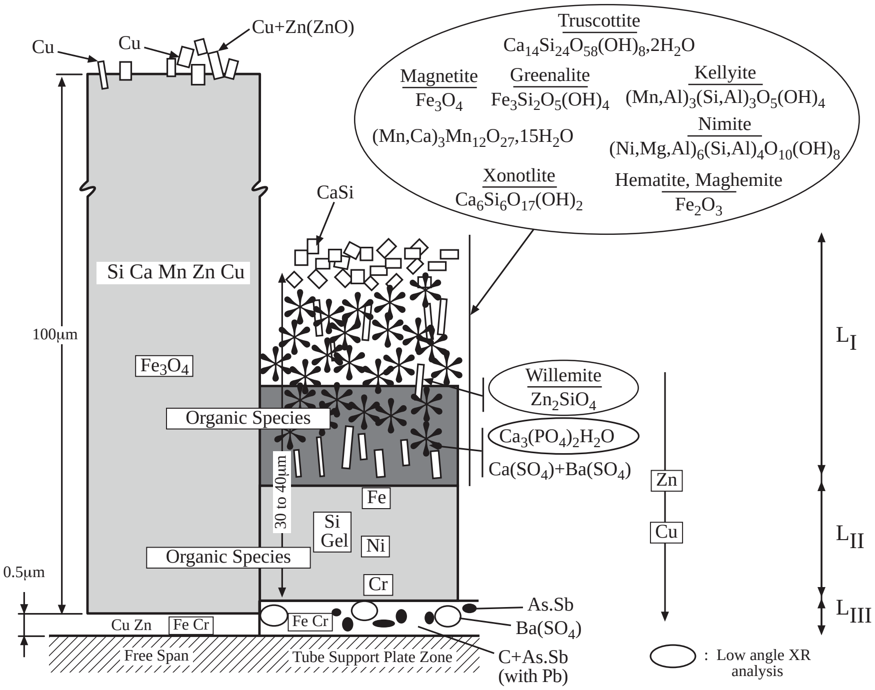

Figure 13 Schematic view of OD tube surface from TSP 2 showing adjacent regions from inside the tube support plate and outside in the free span. The condenser was brass, and morpholine was used for water conditioning. 65,952 operating hours were achieved by the time this specimen was removed. From Sala et al.[27] Taken from St. Laurent B-1 according to Cattant et al.[28] ©1996 NACE International.

SPECIFYING THE CONNECTION BETWEEN STATISTICAL PARAMETERS AND PRIMARY VARIABLES

Correlation of Statistical Parameters with Primary Variables

The core of predicting the first failures in the framework of this discussion is based on connecting the primary variables shown in Figure 8 with the statistical parameters shown in Eqns. (1) to (7). This connection has been described in detail by Staehle,[3,4] and regular dependencies have been identified as shown in Figures 14, 15, 16, and 17.

Figure 14 shows the three statistical parameters plotted versus 1/T for the LPSCC of Alloy 600 MA. Data from both sets of data, Figures 14a and 14c, show similar patterns from two different investigations. In this case β is proportional to the stressor, which is temperature. Figures 15 and 16 show the dependence of the three statistical parameters on stress. Figure 15 shows results for HPSCC for Type 304 stainless steel from investigations in laboratories in the United States and in Japan. Again, the data for the statistical parameters are similar; but, here, the trend of β is inverse to the stressor, which is stress. On the other hand, Figure 16 shows the effect of stress for specimens of Type 304 stainless steel exposed to boiling $MgCl_2$, and the general trend of β is proportional to the stressor, which is stress. Thus, here, in the case of stress, two different trends for the effect of stress on β are shown. Parenthetically the values of β, as shown in Figure 16, show a producable peak. While the origin of this peak has not been studies, it seems to relate to a yield condition such as the flow stress. Figure 17 shows the dependence of statistical parameters for the SCC of Type 304 stainless steel on the concentration on chloride. For the lower concentrations β increases with concentration; and for the higher concentrations β decreases with concentrations.

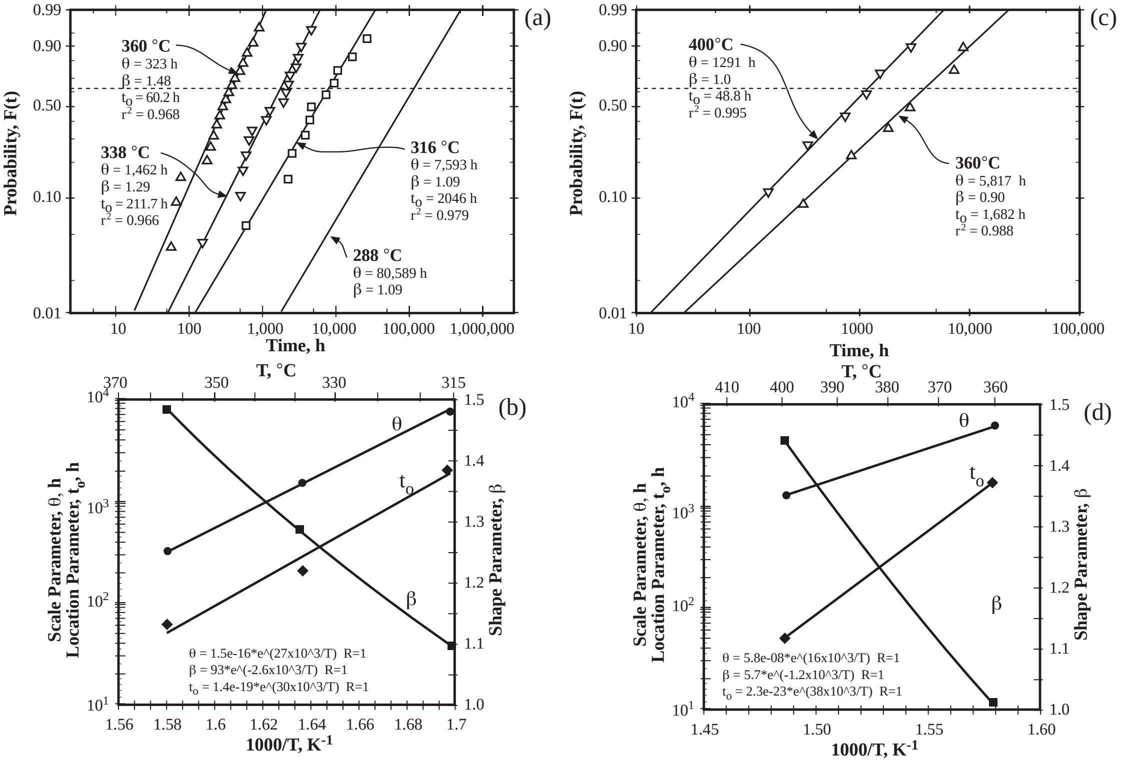

Figure 14 LPSCC of Alloy 600 MA. (a) Probability vs. time to fail by LPSCC for a temperature range of 288 to 360°C for testing in high purity deoxygenated water containing a hydrogen concentration of 10-60 cc H_2/kg H_20. From Webb.[29] (b) Correlation of data in (a) for θ, β, t_o vs. 1/T. (c) Probability vs. time to fail by LPSCC in high purity water and steam for 360 water and 400°C steam with 1 psia hydrogen in the former and 11 psia steam in the latter. From Jacko.[30] (d) Correlation of data in (c) for θ, β, and t_o vs. 1/T.

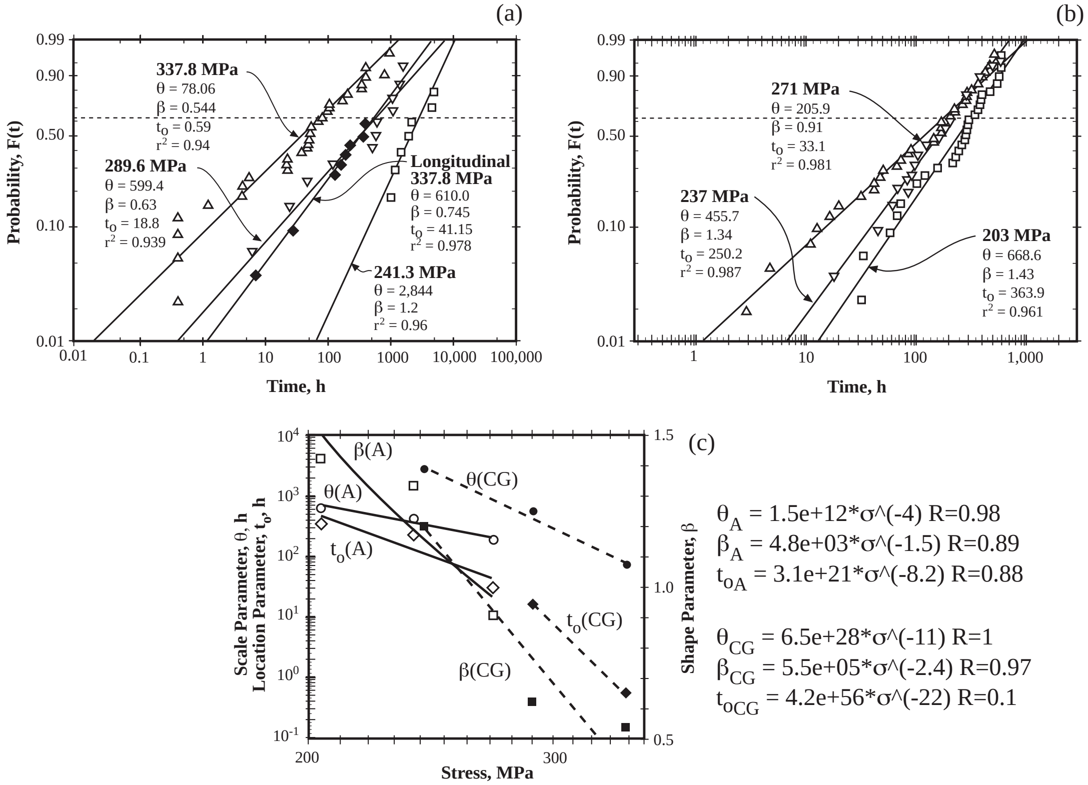

Figure 15 a) Probability vs. time for sensitized Type 304 stainless steel tested at 288°C in high purity oxygenated water. From Clark and Gordon.[31] (b) Probability vs. time for sensitized Type 304 stainless steel tested at 288°C in high purity oxygenated water. From Akashi and Ohtomo.[32] (c) Weibull parameters vs. stress from both the Clark and Gordon (CG) (dotted lines) and Akashi (A) (solid lines) distributions.

Approaches to relating the statistical parameters to primary variables is discussed in subsequent sections.

The Space Parameter, θ

Figures 14 through 17 indicate that the space parameter is essentially the mean value of data. Thus, it is reasonable to evaluate the space parameter as the mean value possibly adjusted for the fact that the value of θ is specified at a probability of 0.632 rather than the mean of 0.5.

The Location Parameter, t_o

Data in Figures 12 through 15 indicate generally that t_o is generally in the range of 0.1θ. For the present purposes, such an evaluation is reasonable and consistent with the data.

Some authors have utilized the location parameter as an initiation time. This is wrong. The initiation process itself is distributed and requires a separate expression. In general, the discussion here concerns the initiation stage of SCC since the examples are based mostly on specimens having initially smooth surfaces. The location parameter is actually a fitting parameter and is not an initiation time.

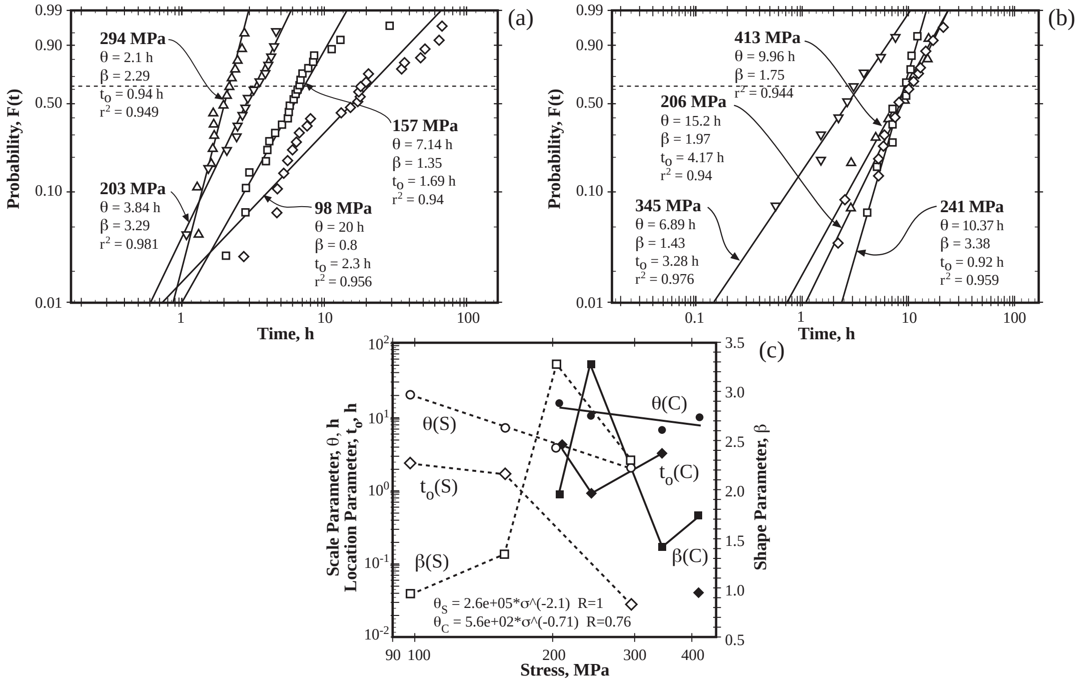

Figure 16 a) Probability vs. time for SCC of Fe-17Cr-11Ni stainless steel exposed to boiling $MgCl_2$ at 154°C° and tested at four stresses. These data are a three-parameter fit of the data shown in Figure 31b. From Shibata and Takeyama.[33] (b) Probability vs. time for SCC of Type 310 stainless steel exposed to boiling $MgCl_2$ at 154°C and tested at four stresses. Specimens were prestrained to 130% yield strength. From Cochran and Staehle.[34] (c) Correlation of θ, β, t_o vs. stress.

The Shape Parameter, β

The shape parameter is the most important of the three statistical parameters since it controls how early the first failures occur for a given mean value of data as illustrated in Figures 1 and 2. Data from field as well as laboratory studies show that slopes over a range from unity to 20 are observed although values in the range of unity to about 5 are the most common.

Despite the great importance of β in predicting early failures, there are no publications that provide insights into the physical significance of β. Such a physical significance of the unit processes that should be incorporated are illustrated in Figure 9 although each of the nine segments in this figure contains substructure that should be identified since the segments themselves are distributed, e.g. the coalescence segment.

Figure 18 illustrates an approach to the physical meaning of β. Figures 18a and 18b show the cdf and hf for β =1.0 and 4.0, respectively, as they are also shown in Figures 1b and 1c. Figure 18a illustrates particularly well the large effect of β on the relative slopes in the cdf. Figure 18b, for the hf, illustrates how the case for β =1.0 produces a probability of failure that is constant in time. The case for β =4.0 produces a probability of failure that is at first zero and at less than $\theta/2$ is low; greater than $\theta/2$ the probability of failure rises rapidly. The implication of these two examples is shown in Figures18c, d, and e. The case for β=1.0, illustrated in Figure 18e, relates to surface processes where the sites for initiation are on the surface and are readily accessible to the environment. When these surface events are the controlling factors in subsequent corrosion, a β =1.0 is expected; and such results are summarized in Figure 5 from the work of Akashi.[17]

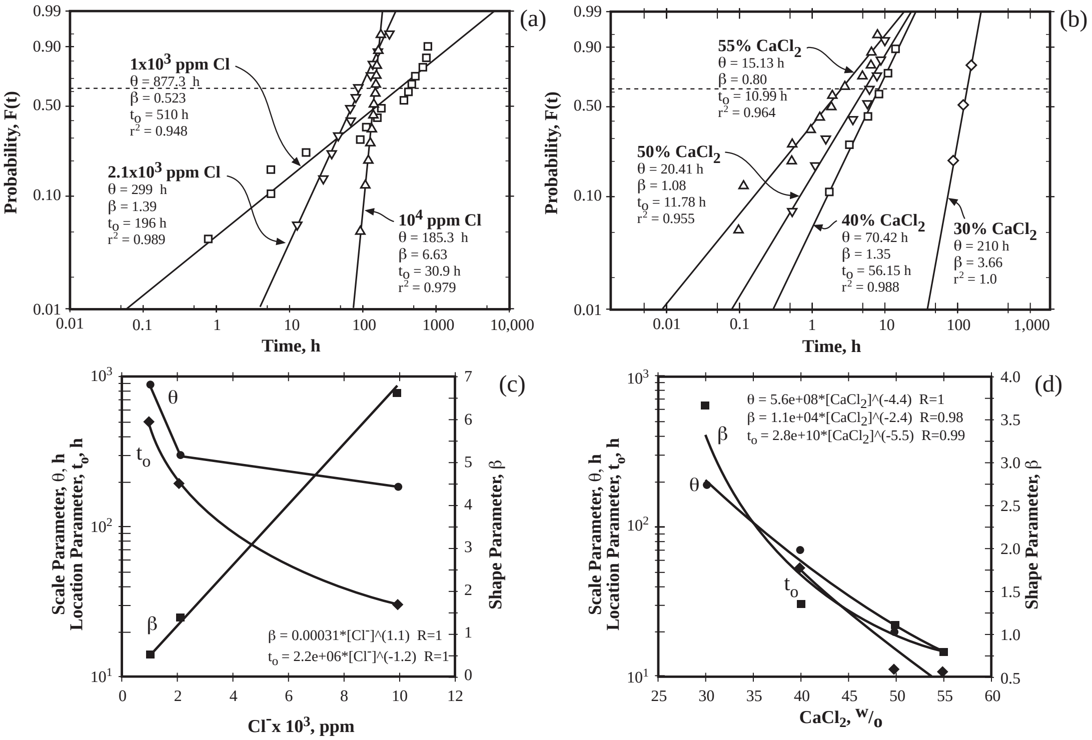

Figure 17 (a) Probability vs. time of sensitized Type 304 exposed to dilute solutions of chloride and stressed at $1.75S_y$ at 80°C in the creviced condition. Data originally plotted as linear H(t) vs. time-to-failure. From Nakayama et al.[35] (b) Correlation of data from (a). (c) Probability vs. time for SCC of Type 304 stainless exposed to high concentrations of $CaCl_2$ at 100°C and 200MPa. From Shibata et al.[36] (d) Correlation of data from (c).

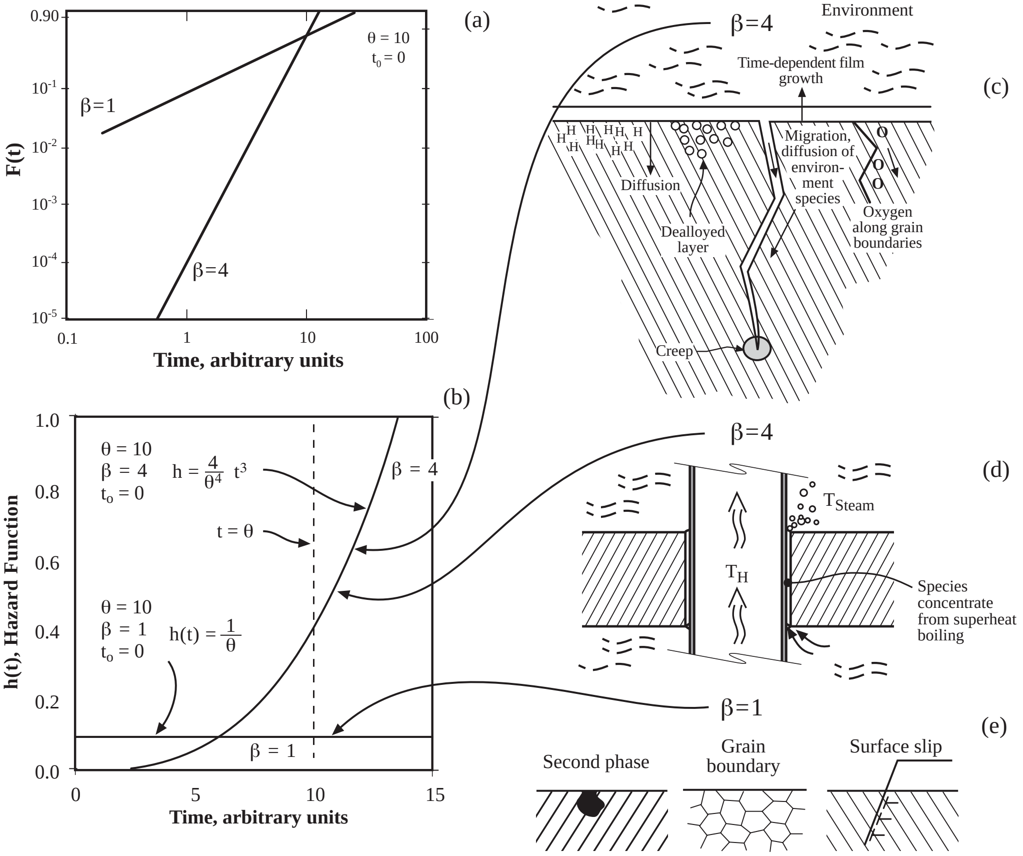

Figure 18 a) cdf for β=1 and β=4 vs. time. (b) hf vs. time for β=1 and β=4 cases at θ=10 and t_o=0. (c) Possible contributions in the metal substrate, for a growing SCC, to the accumulation case for β=4. (d) Possible contributions to the accumulation case β=4 from exterior of the metal surface with a superheated tube support geometry as in Figure 4. (e) Possible contributions to the β=1 case from surface processes.

The case for β=4 is essentially an accumulation case. Some events have to conspire first before failure occurs. Such accumulation events could relate either to the accumulation of a local environment as shown in Figure 18d or to the diffusion of species into a substrate or into a crack as shown in Figure 18c. Thus, the cases for β=1.0 and 4.0, as examples, are distinguished physically by the critical mechanistic processes being either superficial or accumulative, respectively.

Approaching an understanding of space and location parameters seems somewhat intuitive and can be derived directly from observations. An intuitive understanding of the shape parameter is less obvious. For example, in Figures 14 to 17, the shape parameter depends differently upon the stressors—sometimes being directly proportional and sometimes inverse.

In fact, there are five specific complexities in assessing patterns for β that need to be considered:

1. β proportional to stressors—It seems reasonable that increasing a stressor would increase β, i.e. would decrease the dispersion as shown in Figure 1b, when the values of β increase. Stressors include the variables that increase the intensity of corrosion and include: stress, temperature, pH concentration of species, electrochemical potential, and length of time. Thus, one would expect that increasing the stress or the temperature would decrease the dispersion and increase β. Such a result is shown from the work of Shimada and Nagai in Figure 19.

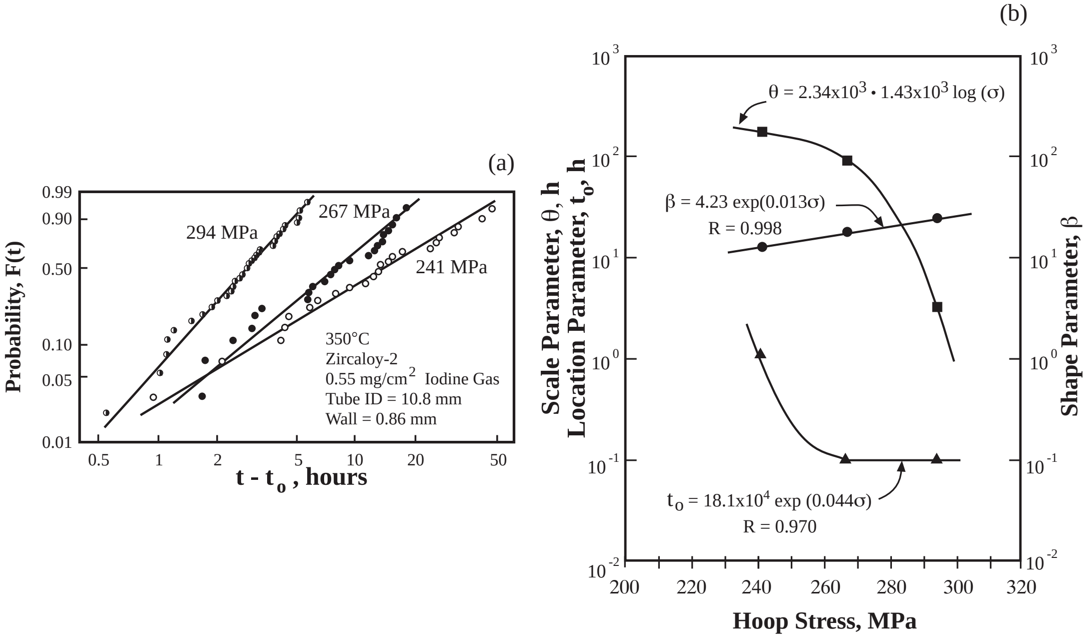

Figure 19 a) Probability vs. time-to-failure for Zircaloy 2 exposed at 350°C to iodine gas. (b) Weibull parameters vs. hoop stress. Adapted from Shimada and Nagai.[37] Determination of curve dependencies from Fang and Staehle.[38]

However, such a pattern of β being proportional to the stressor is not a general result. Figure 15 shows that increasing stress can also reduce the value of β, and this result is obtained from two separate investigations. Figure 17 shows that the effect of concentration on β depends on the range of concentration of chloride species with low concentration producing a positive proportionality and high concentrations producing a inverse proportionality . Figure 16 shows a reproducible peak in the value of β with increasing stress contrary to the effect of stress in Figure 15. This peak seems to relate to a critical value of stress such as the flow stress.

Thus, among investigators there is good agreement for the patterns of β as well as θ and t_o. However, the trends of β are not always intuitive according to an expectation of the dispersion decreasing with increased intensity of the stressors. Reasons for such differences are not obvious.

2. Physical origins of β—The discussion associated with Figure 18 as well as Figure 5 from Akashi[17] indicates that β is associated, in some circumstances, either to conditions related primarily to surfaces or to conditions that relate primarily to accumulation of conditions that precede the propagation of corrosion. However, there is no body of literature nor speculation on the reasons for such patterns.

3. Initiation and propagation—Consistent with the patterns suggested in Figure 18, Shibata and Ichikawa et al.[40,41] have shown that the initiation and propagation produce different values of β. Failures that are dominated by the initiation stage exhibit values of β of close to unity; failures that are dominated by the propagation stage exhibit values in the range of 2 to 5 as shown in Figures 20 and 21.[39] Ichikawa et al have investigated initiation and propagation processes using separate specimens where they were constrained to be controlled by either initiation or propagation. Their results are shown in Figure 21 and show the same patterns as those of Shibata.

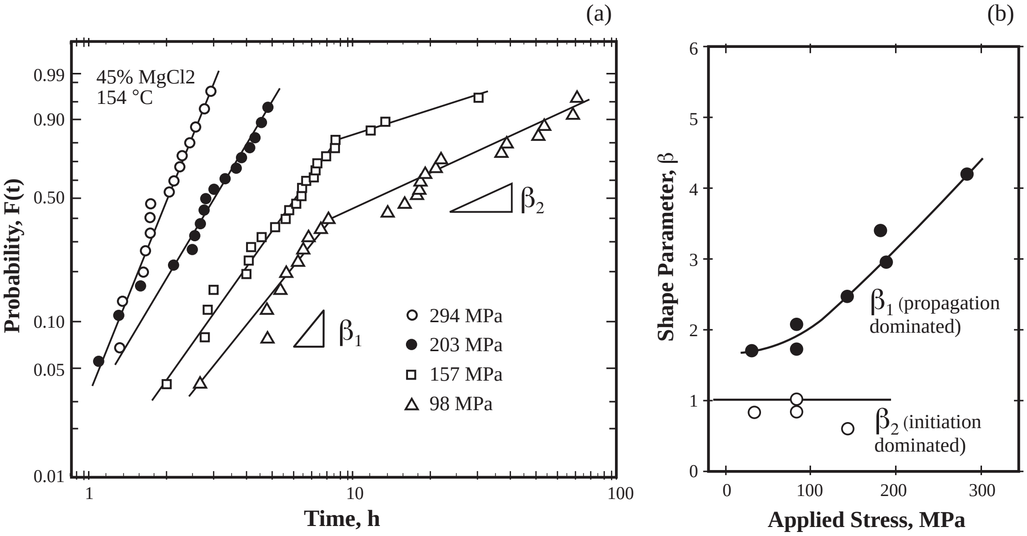

Figure 20 (a) Probability vs. time for Type 304 stainless steel exposed to boiling $MgCl_2$ at 154°C at various stresses. (b) Values of β for upper and lower segments vs. stress from (b). From Shibata and Takeyama.[39]

When both initiation and propagation are important after various times of exposure, the overall Weibull distribution will produce either a bi-modal or a curving shape. Such bi-modal shapes are often due to a change from surface-to accumulation-control as shown in Figure 18. Such combinations make it difficult to extrapolate as well as to estimate the nature of the first failure since there are sometimes significant differences between shape parameters of 1.0 and higher as shown in Figures 2 and 18.

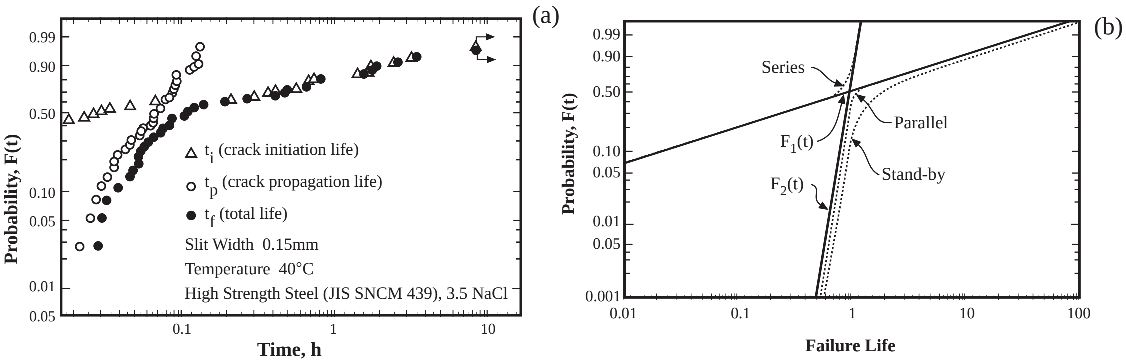

Figure 21 (a) Probability vs. time for data determined for both initiation and propagation of a high strength steel exposed to a 3.5% NaCl solution at 40°C. From Ichikawa et al.[40] (b) Schematic Illustration of the role of both initiation and propagation with the combined result. From Ichikawa et al.[41]

4. Aggregation—The discussion here has assumed implicitly that data were obtained by single investigators and that the value of β relates fundamentally to physical processes. However, more generally, data are developed by numerous investigators and presented as some kind of collection. Figure 22 shows a set of data obtained by Norring[42] for the LPSCC of Alloy 600. The slopes of the individual sets of data are in the range of 1.73 to 7.1. However, if the data points are aggregated and a new correlation is developed using all the data, the value of β is decreased to 1.50 as noted in the figure.

   This effect of aggregation is general, and the result of combining multiple sets of data where the values of θ are different is illustrated in Figure 23. In Figure 23a the aggregate shape parameter, β_g, is plotted vs. the ratio of the highest and lowest scale parameters for the case with four equally spaced cdfs as in Figure 22 and shown specifically in Figure 23b. These calculations show that data tend to a shape factor of unity as the highest and lowest scale parameters are farther apart and as they characterize different sets of nominally similar data.

   A good example of such a β being approximately 1.0 is shown in Figure 3 where the many welds from different locations can be viewed as different heats although exposed to the same nominal water chemistry as in Figure 22.

   Figure 23 suggests that large amounts of data will produce a β_g that tends to unity with all the implications of early failures as implied by Figure 2.

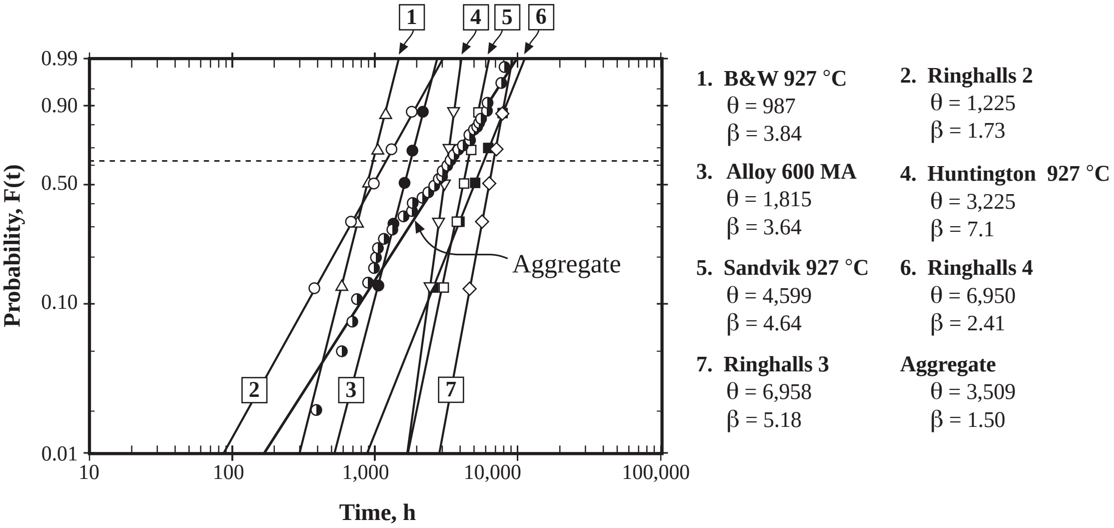

Figure 22 Probability vs. time for seven heats of Alloy 600 exposed to high purity water with hydrogen addition at 365°C using reverse U-bend specimens where failure occurs by the LPSCC submode. From Norring et al.[42] The detailed data were not published with these curves; thus, for analysis, each distribution was assumed to represent five data points, and the analysis of the aggregate distribution was based on this assumption.

5. Testing—The nature of testing affects the value of β as shown in Figure 24 from Shibata[43] and Sato.[44] In these plots there is a general tendency for the shape factor to be proportional to the stressor. For example, the steepest slope of β=13.2 is associated with a SSRT test in Figure 24b. Also, in Figure 24b the more concentrated environment produces less dispersion, β=3.41, than the less concentrated environment, β=1.0. This follows the pattern of β being directly proportional to the stressor.

   In Figure 24a, the field data tend toward β=1.0 as for the data in Figure 3; whereas, the experiments produce higher, although by not much, values of β.

   Thus, methods of testing affect the resulting values of β. Such results are important in accelerated testing where the overall data, i.e. with a β_g, for many heats of materials would tend toward a value of 1.0; whereas, well controlled laboratory testing might produce significantly higher values of β. Such a result would produce misleading predictions for early failures as shown in Figure 25. Figure 25 compares hypothetical cdfs for results from an application (N-1) with results from laboratory testing (A-1). Whereas, the acceleration of the mean values is substantial as would be expected, there is no acceleration when the probability is 0.001 or 0.1% of failures. Thus, accelerated testing could easily give a misleading prediction for the case of early failures.

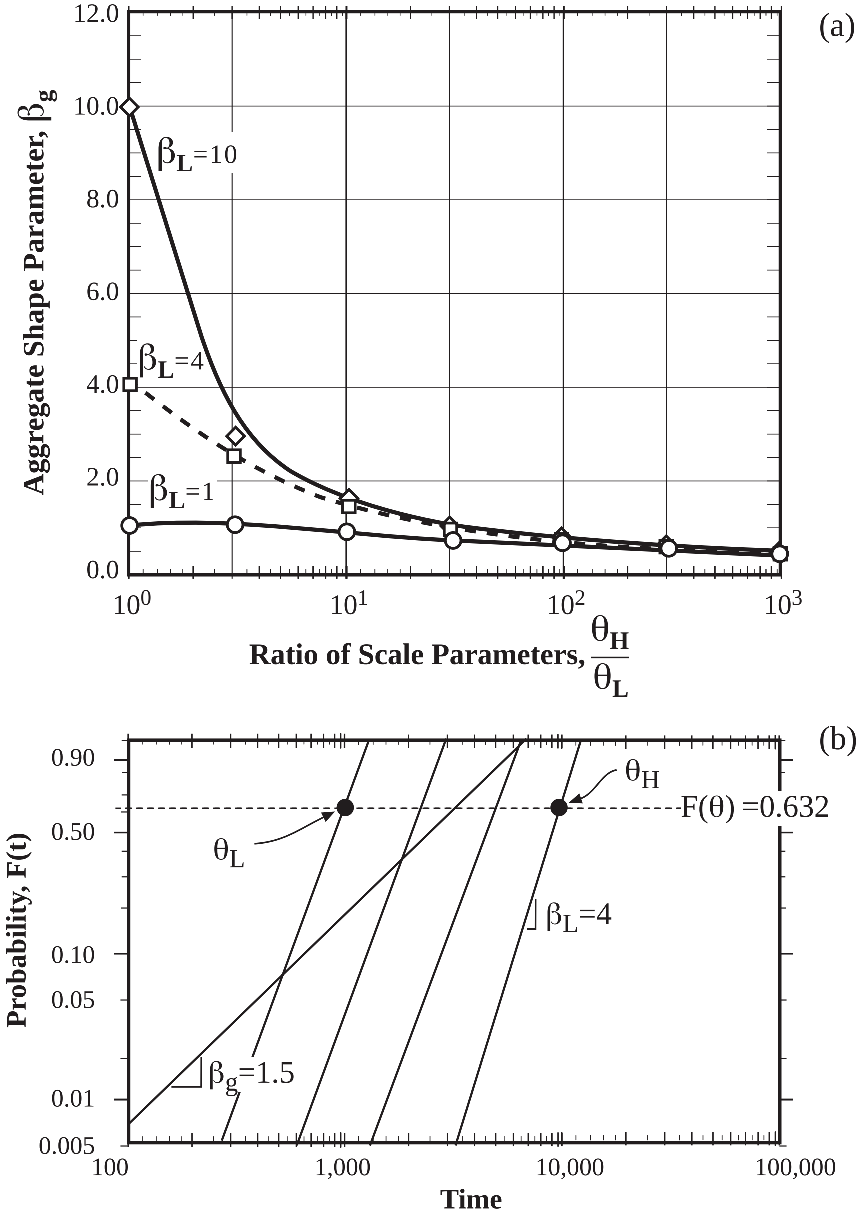

Figure 23 a) Aggregate β_g vs. θ_H/θ_L for local shape parameters of β_L=1, 4 and 10. Four equally spaced sets of data, on a logarithmic scale, are assumed for each calculation and five data points for each component distribution are taken. Based on Weibull distribution. (b) Example of method of calculation. θ_H and θ_L shown with four distributions, each with slopes β_L, and the resulting β_g calculated from aggregating the data for all slopes.

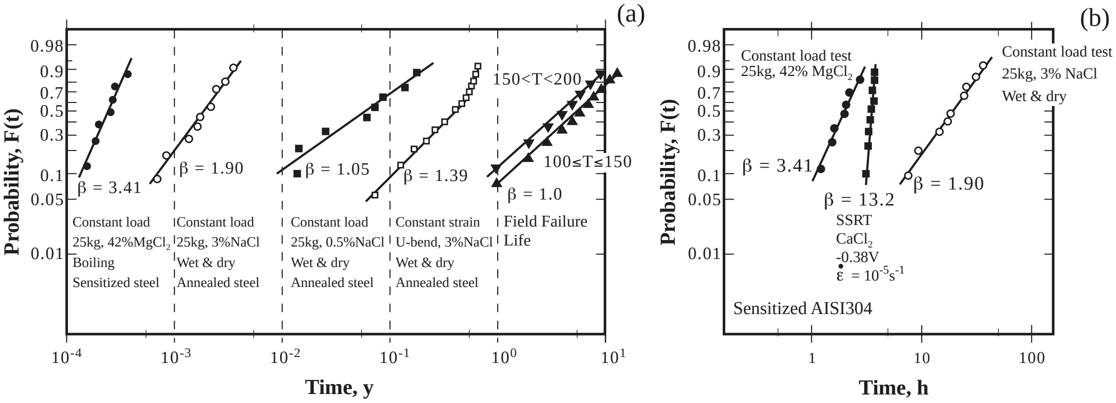

Figure 24 (a) Probability vs. time for various testing methods using Type 304 stainless steel compared with field experience. From Shibata.[43] (b) Probability vs. time comparing the CERT experiment on Type 304 stainless steel with results in (a). From Sato et al.[44]

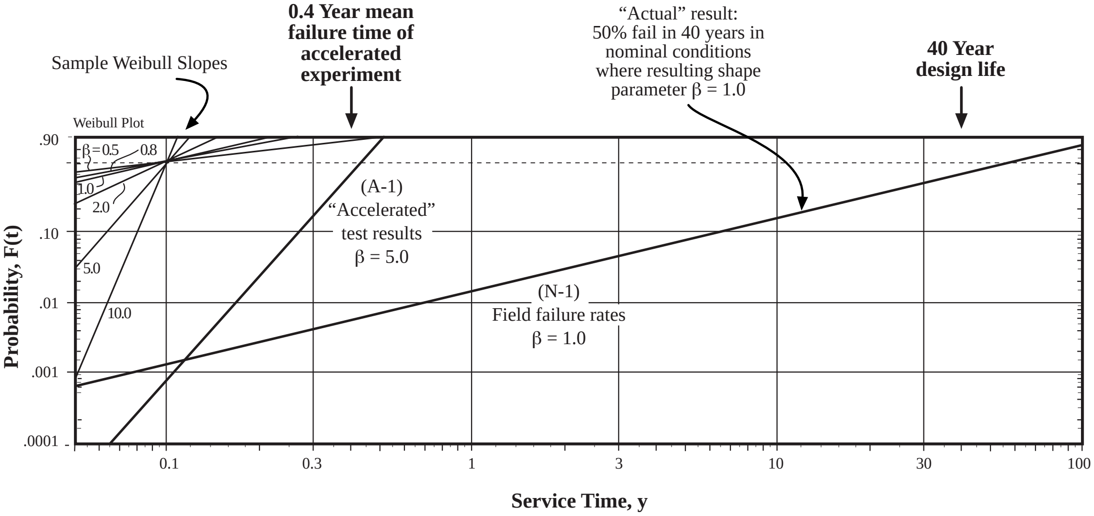

Figure 25 Schematic plot of probability of failure vs. time for field data and accelerated tests based on Weibull coordinates. N-1 corresponds to assumed field results; A-1 corresponds to assumed accelerated testing.

PREDICTION OF EARLIEST FAILURES

The objective of this discussion is to emphasize the importance of earliest failures when compared with the mean time-to-failure. Depending on the value of the shape parameter, β, the earliest failures can occur substantially earlier than the mean as shown in Figures 1, 2, and 18. Such failures can occur so early compared with the mean time-to-failure that data may seem to result from accidents, bad heats, or human errors. In fact, such early failures are to be expected when the pattern of failures is characterized by relatively low values of the shape parameter.

A second objective of this discussion is to demonstrate that the occurrence of early failures can be calculated using an empirical method when the statistical parameters can be evaluated. This approach involves selecting a broadly applicable distribution such as the Weibull and linking its statistical parameters to primary variables that characterize the relevant failure modes. The results of such a calculation permit estimating the time of occurrence of early failures. This method also permits including multiple modes and submodes of failure through determining $R_T(t)$ according to Eqn. (8).

The organization of the calculations developed in this discussion also permits dealing with events that depend on prior events. Such a sequence might involve pitting that is necessary before SCC occurs, although it should be noted that pitting is not often required as the initiating event for SCC. Another more important sequence is that involving the initiation and propagation of SCC as described in Figure 9. In order to handle this in a statistical framework, it would be necessary to develop distributions for both initiation and propagation and then develop a total probability based on their product. This step is not dealt with here. An overall approach to developing predictions of first failures has been considered by Staehle and co-workers.[3,5,6,7]

Steps in developing a model for predicting earliest failures are the following:

The first step is developing an equation similar to that in Figure 8 for expressing each of the statistical parameters. Such expressions would be developed according to Figure 26, and the dependencies would follow the patterns shown in Figures 14-17. Thus, for each of the statistical parameters, θ, β, t_o, an expression would be developed for a cdf similar to that in Figure 8 but in accordance with the dependencies in Figures 14-17. The result would apply then apply to a particular mode or submode of corrosion. Such relationships between the cdfs and submodes of SCC are shown in Figure 27a.

After the submodes to be considered are designed, as shown in Figure 27a, the dependencies are evaluated as shown in Figure 27b. Here, the case for a tube in a tube support is shown from a steam generator in a PWR. Such a joint is known to be corrosive and is complicated by the multiple chemical processes that occur as indicated in Figure 12. To suggest this approach is not so definitive since how these variables are evaluated is more complex than suggested in Figures 27b. If fact, the values of these inputs have to be treated as distributed inputs although using specific values may be adequate. However, this complexity does not change the overall approach.

Once the cdfs of Figure 27a are evaluated with the information from Figures 27b, it is possible to evaluate the cdfs corresponding to the condition designated in Figure 27c. Here a specific pH is selected for evaluation. The final cdfs, then, are shown in Figure 27d. The total probability of failure is based on Eqn. (8) and is shown graphically as $F_T(t)$.

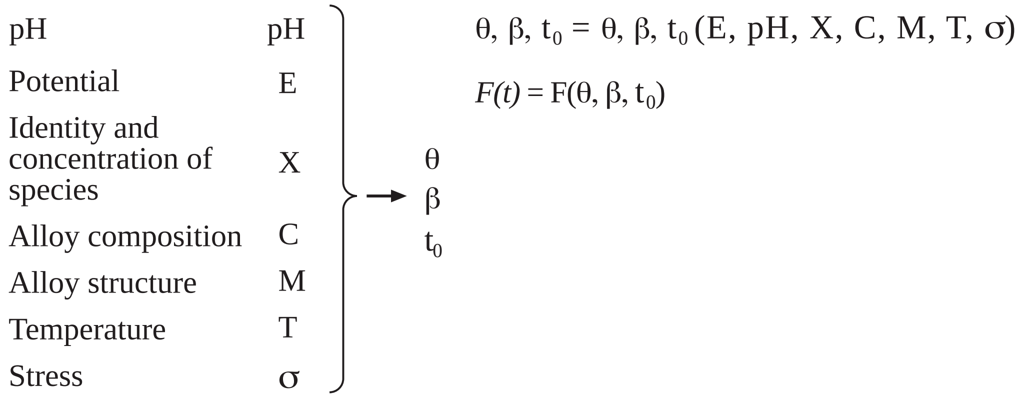

Figure 26 Schematic view of relating the primary variables to the statistical parameters and then obtaining cdfs including statistical parameters that depend on the primary variables.

The $F_T(t)$ of Figure 27d is then the basis for predicting the earliest failures.

Certainly, there are complexities in the procedure illustrated in Figures 26 and 27. Among the important difficulties in developing a prediction, as discussed here, are:

1. Lack of detailed descriptions of the chemical environments at the surfaces of the metal together with their statistical distributions.

2. Heat to heat variation of the response of the metal.

3. Lack of historical patterns and intuitive insights for estimating β.

4. Possible stepwise dependence, e.g. pitting may be necessary for SCC or CF.

5. Mathematical relationships.

Regardless, it is clear that the occurrence of early failures is a reality and that many of the explanations for early failures are not related to bad heats, defective materials, or human error. Such early failures are part of the natural statistical reality. Further, it is possible to develop at least an empirical approach to predicting early failures.

CONCLUSIONS

1. Early failures occur and are a natural part of the statistical nature of corrosion. The occurrence of such early failures relative to the mean depends on the natural dispersion of data for the given corrosion condition. In some cases the earliest failures may occur several orders of magnitude earlier than the mean; in other cases the earliest failures are

not so relatively early. Early failures are more likely related to the natural statistical processes rather than to bad heats, defective materials, and human error.

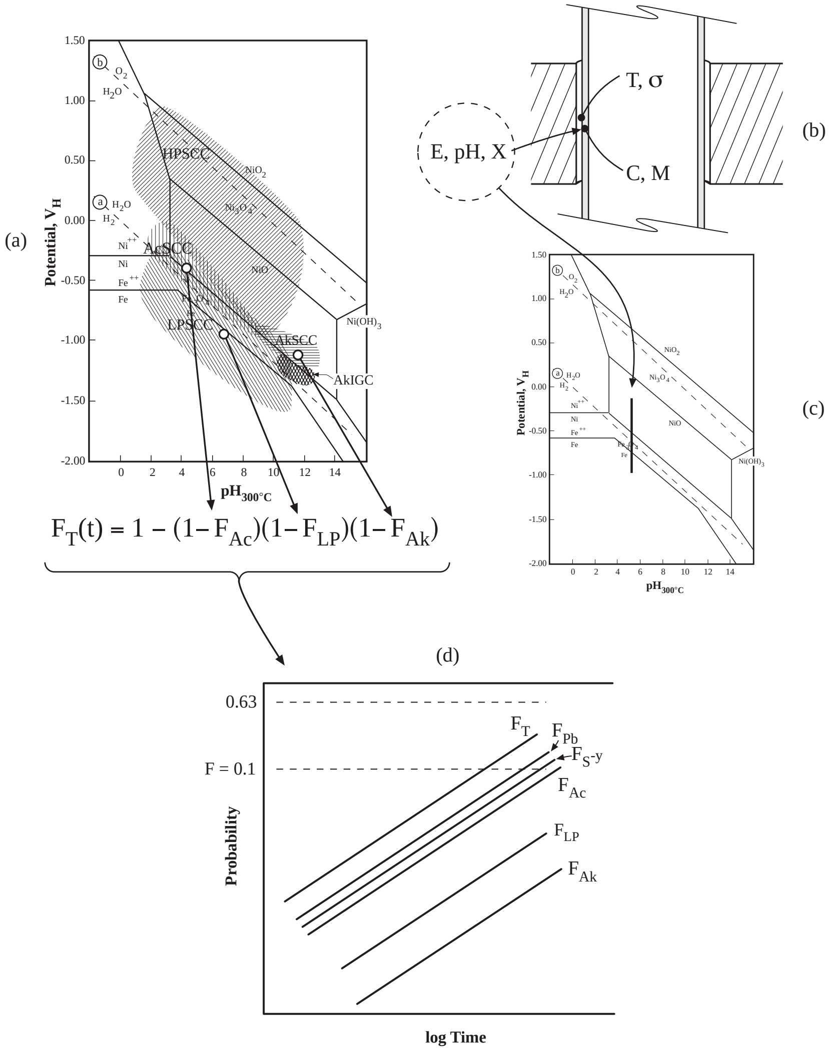

Figure 27 (a) Schematic view of the relationship between submodes of SCC, here for Alloy 600 in the range of 300-350C, and the equation for total reliability in Eqn. (8). (b) Sources of information for evaluating the primary variables from the subcomponent of a tube in a steam generator for a PWR. (c) Illustration of selecting the pH and a range of potentials. (d) The evaluated cdfs together with a total probability.

,

2. The first failure to occur in a set of elements in a component is often the most important event. However, there exists today no bases for predicting such first events. Most predictions are based on results from testing that produces data that is analyzed for its mean value. Such a failure of 50% of the elements would be unacceptable.

3. The proposed approach to predicting first failures is empirical and uses a framework of the Weibull distribution with the statistical parameters evaluated in terms of the primary variables of potential, pH, species, alloy composition, alloy structure, temperature, and stress.

4. This framework permits developing expressions for the probability of failure for multiple non-interacting modes and submodes of failure. The total probability of failure consists of contributions from multiple submodes of corrosion.

5. Developing a quantitative prediction is difficult because: Local environments are difficult to define; heat-to-heat variations seem to have unusual kinds of variabilities; failure processes are often sequential and the critical elements of these segments are often neither clear nor readily quantifiable, and the dispersion of data has little rationalization in the published literature.

6. It is unlikely that a prediction of first failures can be developed from first principles. It seems that using empirical evidence will remain an important contribution for these predictions.

ACKNOWLEDGEMENTS

I appreciate the invitation of the organizers to present this paper. I appreciate discussions with Dr. J. A. Gorman, Dr. Robert Abernethy, and Dr. Zhi Fang.

As usual, I greatly appreciate the work of my staff in preparing this paper especially: Barbara Lea and John Ilg.

REFERENCES

1. R.W. Staehle, “Development and Application of Corrosion Mode Diagrams,” Parkins Symposium on Stress Corrosion Cracking, Eds. S.M. Bruemmer, E.I. Meletis, R.H. Jones, W.W. Gerberich, F.P. Ford, and R.W. Staehle, conference held in Cincinnati, Ohio, October 21-24, 1991, TMS (The Minerals, Metals and Materials Society), Warrendale, Pennsylvania, 1992. p. 447..

2. K.D. Stavropoulos, J.A. Gorman, R.W. Staehle, and C. S. Welty, Jr., “Selection of Statistical Distributions for Prediction of Steam Generator Tube Degradation” Fifth International Symposium on Environmental Degradation of Materials in Nuclear Power

Systems -- Water Reactors, Eds. E. Simonen and D. Cubicciotti, American Nuclear Society, La Grange Park, Illinois, 1991, p. 731.

3. R.W. Staehle, Bases for Predicting the Earliest Penetrations Due to SCC for Alloy 600 on the Secondary Side of PWR Steam Generators; NUREG-CR-6737, U.S. Nuclear Regulatory Commission, Washington, 2001.

4. R.W. Staehle, "Bases for Predicting the Earliest Failures Due to Stress Corrosion Cracking." Chemistry and Electrochemistry of Corrosion and Stress Corrosion Cracking: A Symposium Honoring the Contributions of R. W. Staehle, Ed. Russell Jones, TMS (The Minerals, Metals and Materials Society,) Warrendale, Pennsylvania, 2001, p. K1.

5. R.W. Staehle, "Lifetime Prediction of Materials in Environments," Uhlig's Corrosion Handbook; 2nd Edition, Ed. R.W. Revie, John Wiley and Sons, New York, 2000, p. 27.

6. R.W. Staehle, "Approach to Predicting SCC on the Secondary Side of Steam Generators," presented at Fontevraud V; Contribution of Materials Investigation to the Resolution of Problems Encountered in Pressurized Water Reactors, SFEN, Paris, September 23-27, 2002.

7. Z. Fang and R.W. Staehle, "Development and Application of the SCC Parameter to Predicting SCC in the Secondary Side of Steam Generators," The Ninth International Conference on Environmental Degradation of Materials in Nuclear Power Systems – Water Reactors, Eds. S. Bruemmer, P. Ford, and G. Was, TMS (The Minerals, Metals and Materials Society,) Warrendale, Pennsylvania, 1999, p. 689.

8. R.W. Staehle and Z. Fang, "Factors Affecting the Shape Parameter in the Weibull Distribution with Respect to Predicting Earliest Failures by SCC," Paper 02418, CORROSION 2002, Denver Colorado, April 7-11, 2002, NACE, Houston.

9. W. Nelson, Applied Life Data Analysis, John Wiley and Sons, New York, 1982.

10. A. Stuart and J.K. Ord, Kendall's Advanced Theory of Statistics, Volume 1, Distribution Theory, Oxford University Press, New York, 1987.

11. J.B. Kennedy and A.M. Neville, Basic Statistical Methods for Engineers and Scientists, Third Edition, Harper and Row, New York, 1986.

12. P.D. O'Connor, Practical Reliability Engineering; Third Edition, John Wiley and Sons, New York, 1991.

13. H.M. Wadsworth, ed., Handbook of Statistical Methods for Engineers and Scientists, McGraw-Hill, New York, 1990.

14. WINSMITH (TM) Weibull 3.0U

15. E.D. Eason and L.M. Shusto, Analysis of Cracking in Small Diameter BWR Piping, EPRI NP 4394, Electric Power Research Institute, Palo Alto, 1986.

16. Unpublished data provided by L. Bjornkvist of Vattenfall and J. Gorman of Dominion Engineering.

17. M. Akashi and G. Nakayama, "A Process Model for the Initiation of Stress Corrosion Crack Growth in BWR Plant Materials," Effects of the Environment on the Initiation of Crack Growth; STP 1298, Eds., W.A. Van Der Sluys, R.S. Piascik, and R. Zawierucha, eds., American Society for Testing and Materials, Philadelphia, 1997, p. 150.

18. S. Suzuki, "IGA Resistance of TT Alloy 690 and Concentration Behavior of Broached Egg Crate Tube Support Configuration," Proceedings of the Fifth International Symposium on Environmental Degradation of Materials in Nuclear Power Systems - Water Reactors, D. Cubicciotti, chair., American Nuclear Society, Chicago, 1992, p. 752.

19. Ph. Berge and J.R. Donati, "Materials Requirements for Pressurized Water Reactor Steam Generator Tubing," Nuclear Technology Vol. 55, 1981, p. 88.

20. Private communication with A.R. McIlree, EPRI, Palo Alto, November 1999.

21. H. Nagano, K. Yamanaka, T. Minami, M. Inoue, T. Yonezawa, K. Onimura, N. Sasaguri, and T. Kusakabe, "Effect of Alloying Elements and Heat Treatment on the Corrosion Resistance of Alloy 690," Proceedings: Workshop on Thermally Treated Alloy 690 Tubes for Nuclear Steam Generators; NP-4665S SR, C.E. Shoemaker, ed., EPRI, Palo Alto, 1986, p. 10/1.

22. F. Vaillant, D.Buisine, B. Prieux, J.C. Fournel, and A. Gelpi, "Effects of Microstructure and Mechanical Properties of Alloys 600 and 690 on Secondary Side SCC," Control of Corrosion on the Secondary Side of Steam Generators, R.W. Staehle, J.A. Gorman, and A.R. McIlree, eds., NACE, Houston, 1996, p. 321.

23. R.J. Jacko, Corrosion Evaluation of Thermally Treated Alloy 600 Tubing in Primary and Faulted Secondary Water Environments; NP-6721, EPRI, Palo Alto, 1990.

24. I.L.W. Wilson, F.W. Pement, R.G. Aspden, and R.T. Begley, "Caustic Stress Corrosion Behavior of Fe-Ni-Cr Nuclear Steam Generator Tubing Alloys," Nuclear Technology Vol. 31, 1975, p. 70.

25 P.M. Scott, “2000 F.N. Speller Award Lecture: Stress Corrosion Cracking in Pressurized Water Reactors – Interpretation, Modeling, and Remedies,” Corrosion Vol. 56, 2000, p. 771.

26. R.W. Staehle, “Environmental Definition,” Materials Performance Maintenance, Eds. R.W. Revie, V.S. Sastri, M. Elboujdaini, E. Ghali, D.L. Piron, P.R. Roberge and P. Mayer, Pergamon Press, Ottawa, 1991, p. 3.

27 B. Sala, P. Combrade, A. Gelpi, and M. Dupin, “The Use of Tube Examinations and Laboratory Simulations to Improve the Knowledge of Local Environments and Surface Reactions in TSPs,” Control of Corrosion on the Secondary Side of Steam Generators, Eds. R.W. Staehle, J.A. Gorman, and A.R. McIlree, NACE, Houston, 1996, p. 483.

28. F. Cattant, M. Dupin, B. Sala, and A. Gelpi, “Analyses of Deposits and Underlying Surfaces on the Secondary Side of Pulled Out Tubes From a French Plant,” Contribution of Materials Investigation to the Resolution of Problems Encountered in Pressurized Water Reactors; Proceedings of the International Symposium: Fontevraud III, F. de Keroulas, chair., French Nuclear Energy Society, Paris, 1994, p. Tr1.

29. G.L. Webb, Environmental Degradation of Alloy 600 and Welded Filler Metal EN82 in an Elevated Temperature Aqueous Environment; WAPD-T-2989, Bettis Atomic Power Laboratory, Pittsburgh, 1993.

30. R.J. Jacko, Corrosion Evaluation of Thermally Treated Alloy 600 Tubing in Primary and Faulted Secondary Water Environments; NP-6721-SD, Electric Power Research Institute, Palo Alto, 1990.

31. W.L. Clarke and G.M. Gordon, “Investigation of Stress Corrosion Cracking Susceptibility of Fe-Ni-Cr Alloys in Nuclear Reactor Water Environments,” Corrosion Vol. 29, 1973, p. 1.

32. M. Akashi and A. Ohtomo, “Evaluation of the Factor of Improvement for the Intergranular Stress Corrosion Cracking Life of Sensitized Stainless Alloys in High-Temperature, High-Purity Water Environment,” Journal of the Society of Materials Science of Japan Vol. 36, 59, 1987, p. 59.

33. T. Shibata and T. Takeyama, “Analysis of Stress Corrosion Cracking Failure Times of Type 316 Stainless Steel by the Weibull Distribution,” Boshoku Gijutsu Vol. 30, 1, 1981, p. 47.

34. R.W. Cochran and R.W. Staehle, “Effects of Surface Preparation on Stress Corrosion Cracking of Type 310 Stainless Steel in Boiling 42% Magnesium Chloride,” Corrosion Vol. 24, 1968, p. 369.

35. G. Nakayama, M. Akashi, and A. Ohtomo, "A Probabilistic Assessment for the Stress Corrosion Cracking Lifetime of Sensitized 304 Stainless Steel in Sodium Chloride Solutions," ISIJ International Vol. 31, 1991, p. 223.

36. T. Shibata, J. Nakata, and S. Fujimoto, "Probability Distribution of SCC Failure Time Type 304 Stainless Steel in CaCl2 Solution," Lifetime Prediction of Corrodible Structures, Ed. R.N. Parkins, NACE, Houston, 1994, p. 1064.

37. S. Shimada and M. Nagai, "Variation of Initiation Time for Stress Corrosion Cracking in Zircaloy-2 Cladding Tube," Reliability Engineering Vol. 9, 1984, p. 19.

38. Z. Fang and R.W. Staehle, Calculations with KalidaGraph Software, Version 3.0.

39. T. Shibata and T. Takeyama, "Probability Distribution of Failure Times of Stress Corrosion Cracking of 17Cr-11Ni Stainless Steel," Tetsu-To-Hagane Vol. 66, 1980, p. 693.

40. M. Ichikawa, T. Takura, and S. Tanaka, " A Statistical Aspect of Stress Corrosion Cracking of a High Strength Steel in NaCl Solution," International Journal of Fracture Vol. 16, 1980, p. 251.

41. M. Ichikawa, T. Takura, and S. Tanaka, "A Statistical Study of Stress Corrosion Cracking Life," Bulletin of the ISME Vol. 2, 1983, p. 1857.

42. K. Norring, J. Engstrom, and P. Norberg, "Intergranular Stress Corrosion Cracking in Steam Generator Tubing. Testing of Alloy 690 and Alloy 600 Tubes," Proceedings of the Third International Symposium on Environmental Degradation of Materials in Nuclear Power Systems – Water Reactors, Eds. G.J. Theus and J.R. Weeks, The Metallurgical Society, Warrendale, Pennsylvania, 1988, p. 587.

43 T. Shibata, "Corrosion Probability and Statistical Evaluation of Corrosion Data," Uhlig's Corrosion Handbook; 2nd Edition, Ed. W.R. Revie, John Wiley and Sons, New York, 2000, p. 367.

44. E. Sato, H. Abo, and T. Murata, "Lifetime Estimation and Accelerated Stress Corrosion Cracking Test of Stainless Steel in a Neutral Chloride Environment," Corrosion Vol. 46, 1990, p. 924.

Elevated Temperature Grain Boundary Embrittlement and Ductility-Dip Cracking of Nickel-base Weld Metals

John C. Lippold and Antonio J. Ramirez
The Ohio State University
Columbus, OH USA

Abstract

Intergranular cracking of thick-section, highly restrained weldments made with Filler Metal 52 and 82 has been attributed to a phenomenon known as ductility-dip cracking (DDC). In austenitic weld metals, DDC occurs preferentially along migrated grain boundaries (MGBs) that form in the weld metal following solidification. They represent crystallographic boundaries that migrate away from the parent solidification grain boundary at elevated temperature. This paper will discuss the mechanism of DDC in these filler metal weld deposits in terms of the relationship of DDC to composition, grain boundary structure, and precipitation behavior. In addition, a new test technique, the Strain-to-Fracture (STF) test, will be introduced as a new tool to quantify the susceptibility of a variety of stainless steels and Ni-base alloys to DDC.

The STF test was developed to determine the relationship between temperature and minimum strain to initiate grain boundary cracking in the DDC temperature range. Using this test, a strain-temperature envelope is determined that can be used to quantify susceptibility. Significant differences in DDC susceptibility have been observed between Filler Metals 52 and 82 using the STF test that correlate well with cracking encountered during actual fabrication. For example, strains as low as 2% in the temperature range from 750 to 1150 ºC are sufficient to initiate cracks in Filler Metal 52 weld deposits, while strains in excess of 4% are required to initiate cracking in Filler Metal 82.

Considerable microstructural characterization has been conducted in order to understand these differences in DDC susceptibility. Techniques include optical and scanning electron microscopy, transmission electron microscopy, and electron backscattered diffraction (EPSD). These characterization studies have revealed that susceptibility is related to the degree of grain boundary "tortuosity" and the inter-related effects of grain boundary precipitation. Filler Metal 52 weld metals exhibit long, straight MGBs with little or no grain boundary pinning that promotes tortuosity. In contrast, Filler Metal 82 weld metals contain tortuous MGBs as a result of (Nb,Ti)C formation that occurs at the end of solidification. These particles are very effective in pinning the MGBs, resulting in a grain boundary that is highly resistant to grain boundary sliding and cracking during elevated temperature deformation. The paper will provide additional insight into the mechanism of DDC, including potential preventative measures.

Weldability of Austenitic Materials

Austenitic weld metals may suffer from a variety of cracking phenomena. These alloys are especially susceptible to “hot” cracking due to the presence of liquid films along grain boundaries, forming either at the end of solidification or during reheating. In addition, austenitic weld metals are susceptible to a number of elevated temperature solid-state cracking phenomena, including ductility-dip cracking, and reheat or strain-age cracking. Table 1 lists the cracking phenomena associated with austenitic weld metal. All of these cracking phenomena occur along grain boundaries in the weld metal and are dependent on the composition and nature of those boundaries.

Cracking in austenitic weld metal is associated with the weld metal solidification grain boundaries and/or weld metal migrated grain boundaries. Figure 1 is a schematic illustration of the three boundary types, 1) solidification grain boundaries (SGB), 2) solidification subgrain boundaries (SSGB), and 3) migrated grain boundaries (MGB) in fully austenitic weld metal.(1) The solidification grain boundaries are high angle grain boundaries that form during the solidification process due to the intersection of groups, or packets, of opposing subgrains (cells and dendrites). Additionally, segregation during the solidification process adds a compositional component to the SGBs. The instability of the solid/liquid interface during the solidification process generates a substructure formed by cells and/or dendrites within the grains, with small crystallographic misorientation at the subgrain boundary. Thus, the SSGB represents a low angle boundary with an associated compositional component resulting from solidification segregation. Once the weld metal has solidified, the crystallographic component of the SGB may migrate away from its original position, leaving behind the compositional component of the SGB. This migration is driven by a reduction in boundary free energy by straightening relative to the parent SGB. The MGB then represents a high angle crystallographic boundary whose composition reflects the microstructure into which it has migrated. Segregation of impurity elements to the MGBs is also possible via a grain boundary “sweeping” mechanism.

Table 1: Weldability issues with austenitic materials

Cracking Mechanism	Location	Factors that Promote
Solidification Cracking	Solidification grain boundary	Impurity and alloy elements segregation Continuous liquid film
Weld Metal Liquation Cracking	Solidification grain boundary Migrated grain boundary	Impurity and alloy elements segregation Large grain size High heat input
Ductility-Dip Cracking	Migrated grain boundary	Large grain size Grain boundary mobility
Reheat or Strain-Age Cracking	Migrated grain boundary	Relaxation of residual stresses Intragranular precipitation Impurity segregation
Copper-Contamination Cracking	Migrated grain boundary	Cu abraded on surface Temperature > 1093 °C
Hydrogen-Assisted Cracking	Migrated grain boundary	Grain boundary precipitation Threshold H concentration

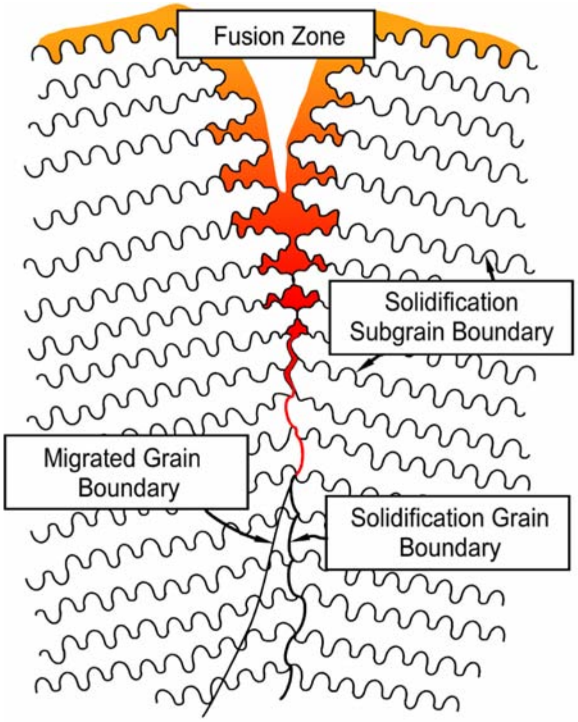

Figure 1, Schematic illustration of weld metal boundaries in austenitic weld metal. (1)

Ductility Dip Cracking

Haddrill and Baker (2) defined ductility-dip cracking (DDC) as the loss in ductility, over a temperature range below the solidus, sufficient to produce cracking under the influence of thermal strain caused by welding. Ductility-dip cracking susceptibility is quantified by the ductility-dip temperature range (DTR) and the threshold strain for cracking. (3) A schematic showing the expected ductility as well as a ductility-dip is shown in Figure 2. Zhang et al (4), determined that for a material to be considered resistant to DDC the DTR should be less than 100°C wide and/or the threshold strain should be greater than 15%.

Hemsworth et al. (5) defined DDC as occurring above $0.5T_m$ (T_m = melting point) at boundaries that are free from liquid films. It is not clear exactly when the ductility-dip cracks occur but it appears that they can occur during both the heating and cooling portion of the weld thermal cycle.

Most of the materials susceptible to DDC have a face-centered cubic (FCC) and/or austenitic microstructure. They tend to be single phase from room temperature to melting and solidify with an FCC crystal structure. In the weld metal, DDC occurs preferentially along migrated grain boundaries (MGBs). It may also occur in the base metal although the HAZ of wrought materials have been found to be more resistant to DDC than that of autogenous weld metal.

A number of tests have been used to determine susceptibility to DDC, including the Gleeble hot ductility test and the Varestraint test. Kikel et al. (6) used the “Double Spot” Varestraint test technique to evaluate DDC in nickel-base Filler Metal 52, Filler Metal 82 and other nickel-base alloys. Their studies showed Filler Metal 52 to be more susceptible to DDC than Filler Metal 82. Although DDC was identified with this technique, the test proved to be limited in its ability to precisely control peak temperature, thermal cycle and applied strain. In addition to these limitations, avoiding the solidification and liquation cracking temperature ranges proved difficult and metallographic sample preparation was severely inhibited by the final sample geometry.

Because of these limitations, a more discriminating test technique for DDC evaluation was developed by Nissley and Lippold (7,8) using the Gleeble thermal-mechanical simulator. This test technique, termed the Strain-to-Fracture (STF) test, allows for a material to be tested at a specific temperature and a pre-determined strain. Unlike the “Double-Spot” Varestraint test, temperature and strain are tightly controlled within a temperature range outside of the solidification and liquation-cracking temperature ranges such that DDC can be isolated and evaluated accordingly.

Other than alloy composition and crystal structure (FCC), other factors that influence DDC include grain size, precipitation behavior, impurity segregation, grain boundary orientation, grain boundary “tortuosity, and recrystallization. Recent studies by Collins et al. (9,10) and Ramirez and Lippold (11,12) have quantified the DDC susceptibility of Ni-base base filler metals 52 and 82 using the STF test and provided new insight into the mechanism of DDC in Ni-base weld metals. A summary of that work is provided here.

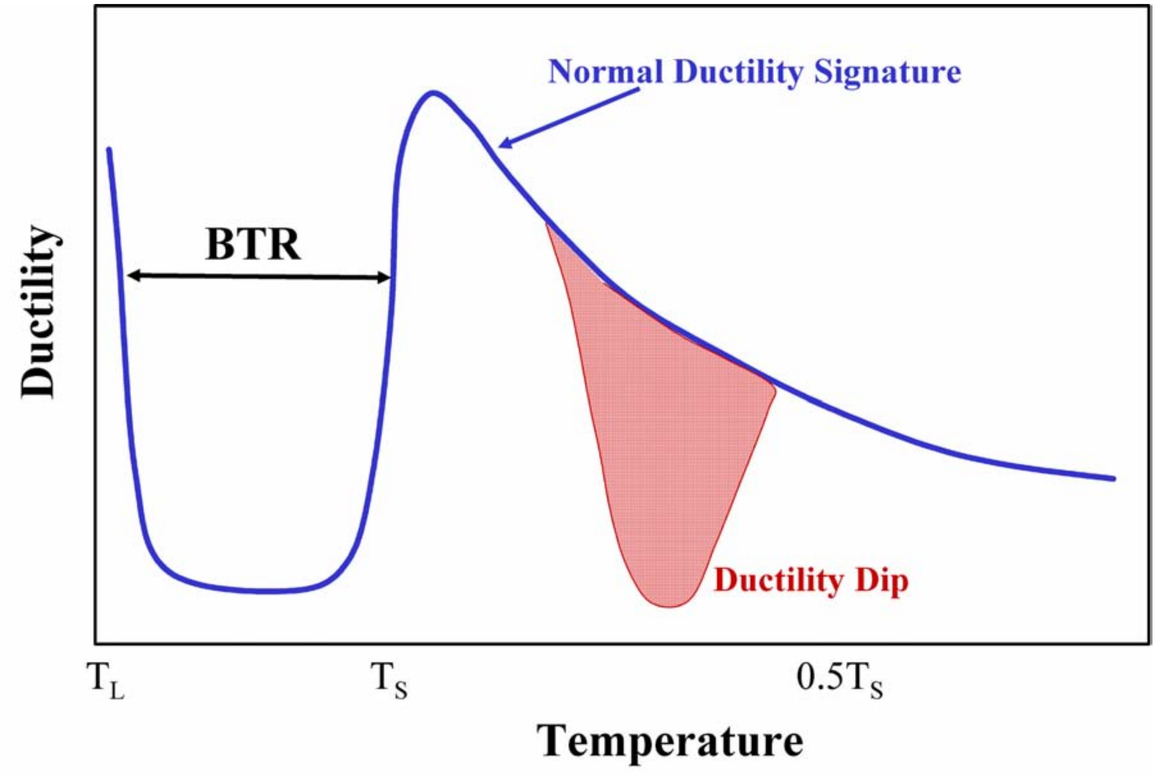

Figure 2, Ductility versus temperature behavior for a normal material and one that exhibits a ductility dip.

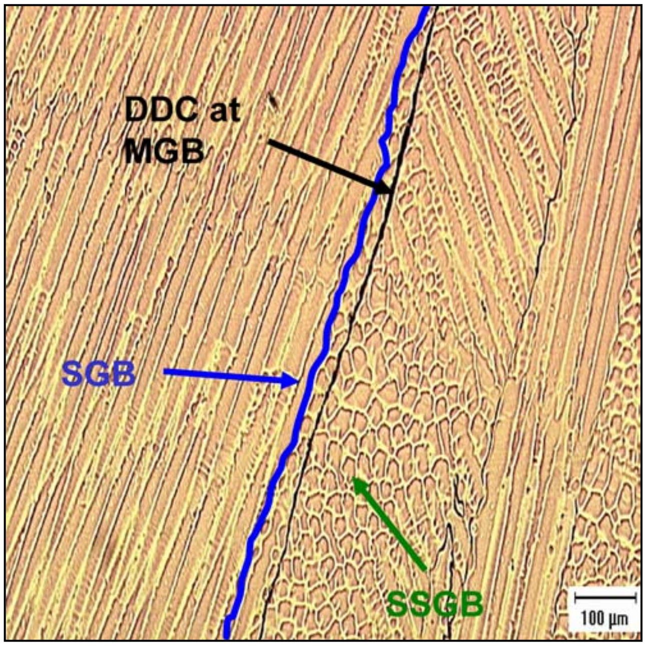

Figure 3. Cracking along a migrated grain boundary in a Filler Metal 52 weld deposit.

Strain-to Fracture Test Results

A representative ductility-dip crack in a FM52 strain-to-fracture sample is shown in Figure 3. Note that cracking occurs along a migrated grain boundary in the microstructure and that this boundary is extremely straight (non-tortuous).

Strain-to-fracture testing of both FM52 and FM82 filler metal deposits was conducted over the temperature range of 600 to 1200 ºC and a strain range of 1 to 20%. Details of the sample preparation and testing procedures can be found elsewhere. (9,10). Results for Filler Metal 52 are shown in Figures 4 and 5. In Figure 4, the threshold strain-to-fracture is represented by the heavy line. This defines the minimum strain below which ductility dip cracking will not occur. Note that DDC in Filler Metal 52 can occur at strains below 2% in the temperature range from 850 to 1150 ºC. In Figure 5, the total number of cracks is plotted as a function of temperature and strain. Note that there is a very dramatic increase in cracking above the threshold strain.

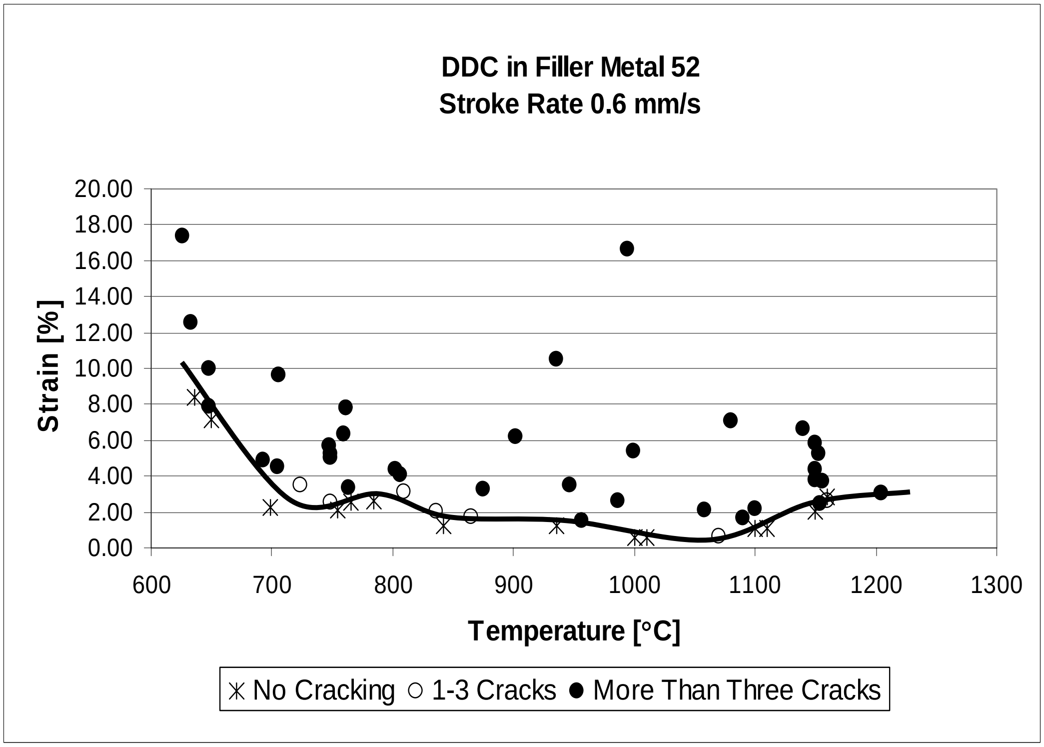

Figure 4, Strain-to-fracture test results for Filler Metal 52.

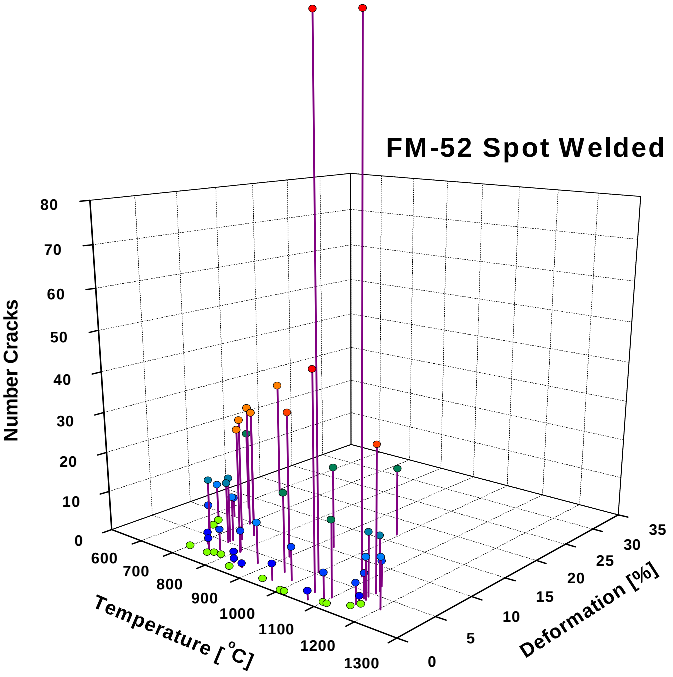

Figure 5, Strain to fracture results for Filler Metal 52. Number of cracks versus strain and temperature.

STF results for two heats of Filler Metal 82, plotted together with Filler Metal 52 results from Figure 4 are shown in Figure 6. This data shows that FM82 also exhibits a drop in elevated temperature ductility over the same temperature range as FM 52, but that the threshold strain to cracking is higher. The higher threshold strain for FM82 reflects the fact that it has better resistance to DDC under fabrication conditions.

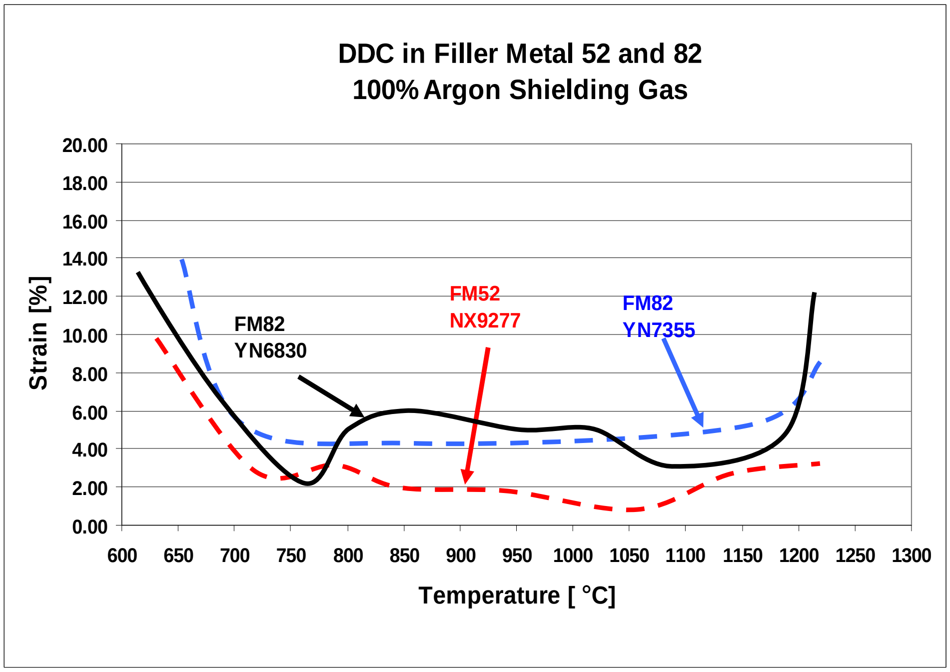

Figure 6. Strain-to-fracture results for Filler Metal 52 and two heats of Filler Metal 82

STF testing of FM82 also investigated the effect of shielding gas. Both 100% argon and 95%Ar/5% H_2 shielding gases were used to prepare STF samples. The latter shielding gas mixture was selected since it is widely used in conjunction with FM52 and FM82 filler metals. As shown in Figure 7, the introduction of hydrogen significantly reduces the threshold strain-to-fracture for this filler metal. Above 800 °C, the threshold strain drops below 1% and the degree of cracking in the sample increases dramatically. With only 2% applied strain at 1000 °C, literally dozens of cracks were observed in the FM82 STF sample.

Ductility-Dip Cracking Mechanism

Ductility-dip cracking can be characterized as a grain boundary, creep-like phenomenon where resistance to cracking at the low temperature extreme of the ductility trough results from the inoperability of GB sliding. Ductility recovery at the high temperature extreme is due to the onset of dynamic recrystallization. In the STF samples, ductility-dip cracks are normally formed at about 90° to the externally applied load, verifying the GB orientation dependency of such a GB sliding phenomenon. The GB triple points and any other irregularity along the GBs, such as intergranular precipitates and GB steps and jogs oppose GB sliding, leading to local strain concentration. These strain concentration sites along the GBs then become the void initiation sites. If the temperature and strain conditions are appropriate, the growth and linking of these voids cause microcrack formation, resulting in DDC.

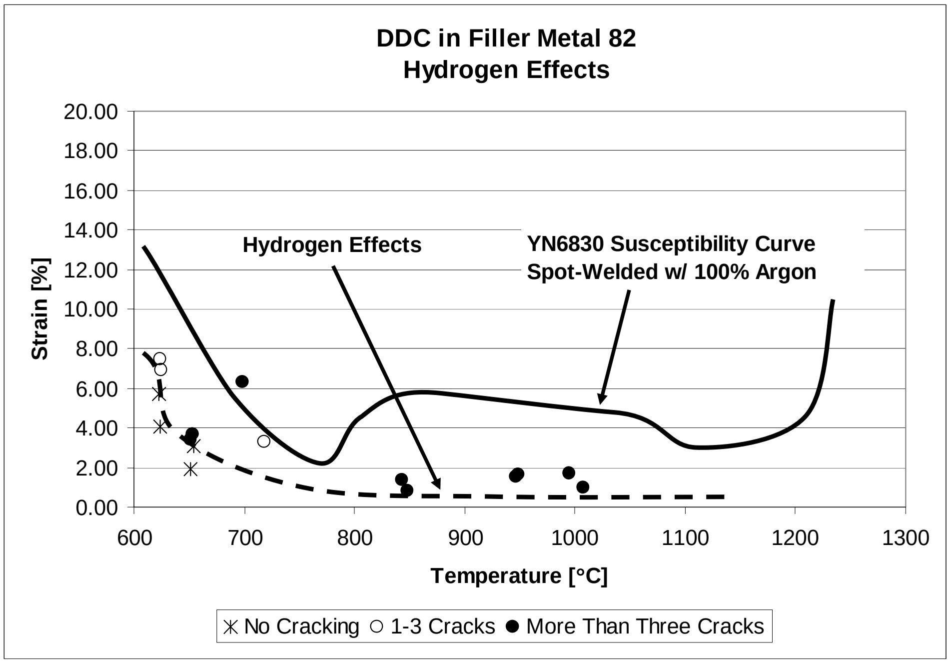

Figure 7. Effect of hydrogen on DDC of Filler Metal 82. Comparison of strain-to-fracture tests of samples made using shielding gas consisting of 100% Ar and 95% Ar + 5% H.

Microstructure Effects. Weld metal microstructure is the primary factor that influences susceptibility to DDC. In the FM52 weld metal, the migrated grain boundaries were typically very straight with little metallographic evidence of grain boundary precipitation. A representative MGB, as characterized in the SEM, is shown in Figure 8. These straight, non-tortuous boundaries were found to be the most susceptible to DDC at relatively low applied strains. Other boundaries were observed in FM52 weld metal that exhibited more tortuous grain boundaries, such as that shown in Figure 9, but these were unusual. These more tortuous boundaries resulted from grain boundary pinning by large carbides that formed at the end of solidification. They were much more resistant to cracking than the straight boundary shown in Figure 8.

In FM82, effective GB pinning resulted from the presence of medium-sized (1 μm) (Nb,Ti)C carbides that form at the end of solidification via a eutectic reaction. In FM82, the migrated grain boundaries were found to be quite tortuous due to the presence of these particles. This imposes a mechanical locking effect on the boundary that reduces strain accumulation at triple points and allows strain to be more uniformly distributed along the boundary.

Strain accumulation in the microstructure can be measured using an electron backscatter diffraction (EBSD) technique. Using this technique, a strain map on a microstructure level can be produced. An example of such a map is shown in Figure 10. This clearly shows that strain accumulates along the migrated grain boundaries, particularly at triple points and locations where grain boundary pinning has occurred.

Composition Effects. Alloy composition also has an important effect on DDC resistance. The addition of elements that result in the precipitation of medium size particles during or at the end of solidification will result in tortuous grain boundaries and therefore improved DDC resistance. For FM82, the combination of C, Nb, and Ti promotes a eutectic reaction at the end of solidification and the formation of medium size (Nb,Ti)C carbides. As described previously, these have a beneficial effect on increasing grain boundary tortuosity and enhancing the mechanical locking of the boundary during straining.

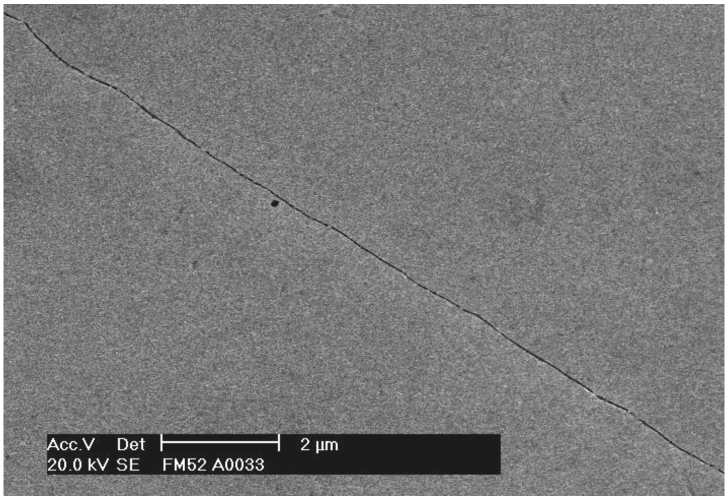

Figure 8. Straight, precipitate-free grain boundary in Filler Metal 52 weld metal.

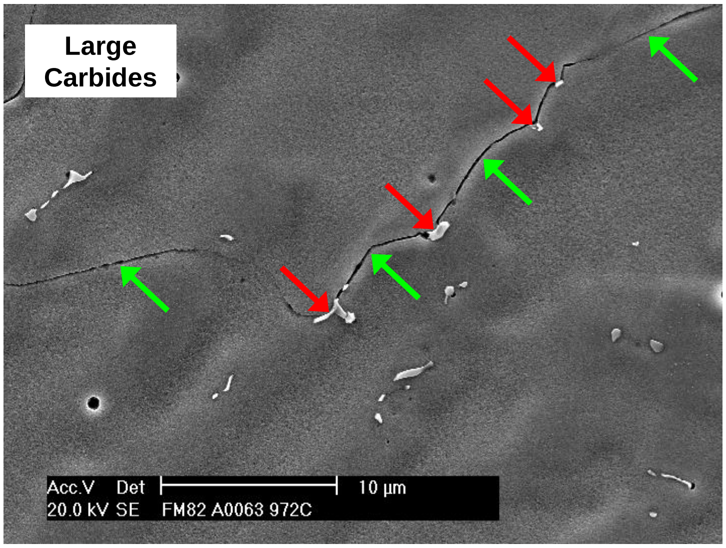

Figure 9. Tortuous grain boundary in Filler Metal 52 resulting from local grain boundary pinning.

For the case of FM-52, the sporadic formation of large carbides and nitrides (TiN) had a similar effect on GB tortuosity, but this effect was not widespread enough to improve resistance to cracking. Although, the effect of particle size and type on DDC resistance is not entirely clear, it appears that control of precipitate distribution by appropriately modifying the composition is one approach for increasing resistance to DDC.

Impurity segregation to the migrated boundaries can also influence susceptibility. Collins showed that additions of sulfur severely reduced the threshold for cracking in FM82. (10) Thus, it appears that reducing impurities, including sulfur, phosphorus, oxygen, and others, is helpful. The dramatic effect of hydrogen on reducing the cracking threshold (Figure 7) was surprising, since hydrogen is generally thought to be quite mobile in the DDC temperature range. The potential for trapping of hydrogen at grain boundary sites is the subject of a continuing investigation.

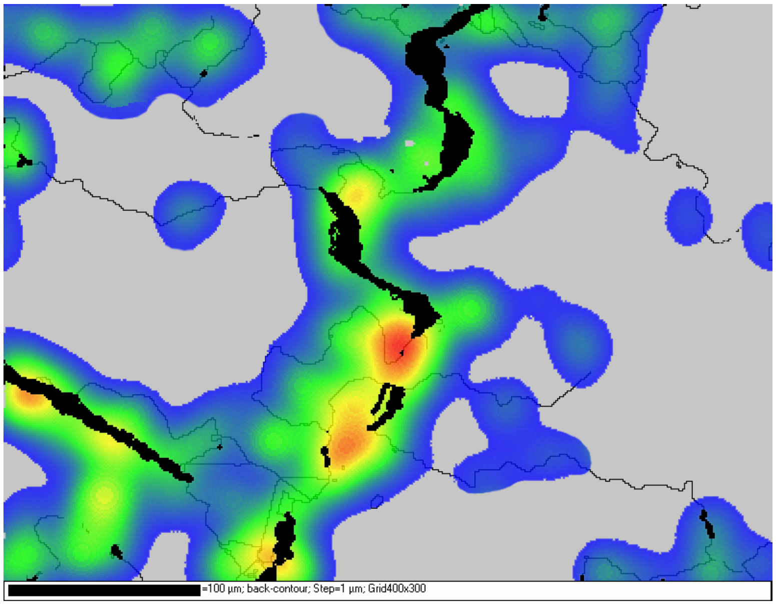

Figure 10. Microstrain mapping in a cracked strain-to-fracture sample of Filler Metal 82 strained 11.3% at 1150 °C.

Summary

Ductility-dip cracking in Ni-base filler metals 52 and 82 has been quantified using the strain-to-fracture test. Results from this test show that the ductility dip is actually a ductility "trough" that extends from 750 to 1150 ºC. Within this temperature regime the threshold strain for cracking was 2% in Filler Metal 52 and 4-5% in Filler Metal 82. Above the threshold strain, Filler Metal 52 exhibit much more severe cracking than Filler Metal 82 for equivalent temperature and strain conditions. This is reflective of the higher DDC susceptibility encountered during fabrication of highly restrained, welded sections.

The primary factors influencing DDC susceptibility are grain size, grain boundary tortuosity, precipitation behavior, and impurity segregation. Filler Metal 52 weld metal exhibits long, straight migrated grain boundaries that result in strain accumulation and cracking at grain boundary triple points. Filler Metal 82 weld metal contains many (Nb,Ti)C precipitates that pin the migrated grain boundaries, resulting in a tortuous grain boundary path. This tortuosity provides a grain boundary locking effect that effectively opposes grain boundary sliding. In studies of other austenitic alloys (Alloy 690, Type 310 and 304 SS, and AL6XN SS), grain boundary tortuosity was found to be the most influential factor relative to the onset of DDC.

Additions of sulfur and hydrogen to Filler Metal 82 weld deposits were found to significantly increase DDC susceptibility. The addition of hydrogen was particularly damaging, reducing to threshold strain to fracture to less than 1% in the temperature range from 800 to 1100 ºC. This is also reflective of industry experience, where the use of 95Ar-5H_2 shielding gas mixtures has been found to promote more cracking than 100% He shielding.

Considerable work has been conducted to characterize the microstructure and fracture characteristics of these filler metal deposits. These investigations included the use of SEM, TEM, and EBSD techniques to characterize the nature of the grain boundaries in these weld metals and to relate the grain boundary characteristics to fracture morphology. The reader is referred to the work of Collins (10,13,14) and Ramirez (11,12) for details of this work.

References

1. J.C. Lippold, W.A.T. Clark, M. Tumuluru. 1992. An investigation of weld metal interfaces, *The Metals Science of Joining*, Warrendale, PA. The Metals, Minerals and Materials Society, pp. 141-146.
2. Haddrill, D.M., Baker, R.G., “Microcracking in Austenitic Weld Metal”, *British Welding Journal*, Volume 12, Number 9, August 1965.
3. Arata, Y., Matsuda, F., Katayama, S., “Solidification Crack Susceptibility in Weld Metals of Fully Austenitic Stainless Steels (Report II),” *Transactions of JWRI*, Vol. 6, No. 1, June 1977, pp. 105–116.
4. Zhang, Y.C., Nakagawa, H., Matsuda, F., “Weldability of Fe-36%Ni Alloy (Report III),” *Transactions of JWRI*, Vol. 14, No. 1, July 1985, pp. 107–114.
5. Hemsworth, B., Boniszewski, T., Eaton, N.F., "Classification and Definition of High Temperature Welding Cracks in Alloys," *Metal Construction & British Welding Journal*, February 1969, pp. 5-16.
6. J.M. Kikel and D.M. Parker, Ductility Dip Cracking Susceptibility of Filler Metal 52 and Alloy 690, *Trends in Welding Research*, 1998, pp. 757-762.
7. N.E. Nissley and J.C. Lippold, 2003. Ductility-Dip Cracking Susceptibility of Austenitic Alloys, *Trends in Welding Research*, Proc. of the 6th Intl. Conf., ASM International, pp. 64-69.
8. N.E. Nissley and J.C. Lippold. 2003. Development of the strain-to-fracture test for evaluating ductility-dip cracking in austenitic alloys, *Welding Journal*, 82(12):359s.
9. M.G.Collins, J.C. Lippold and J.M. Kikel, 2003. Quantifying Ductility-Dip Cracking Susceptibility in Nickel-base Weld Metals using the Strain-to-Fracture Test", *Trends in Welding Research*, Proc. of the 6th Int. Conf., ASM International, pp. 586-590
10. M.G. Collins and J.C. Lippold. 2003. An investigation of ductility-dip cracking in Ni-base filler metals-Part 1, *Welding Journal*, 82(10):288s-295s
11. A.J. Ramirez and J.C. Lippold, 2004. High temperature cracking in nickel-base weld metal, Part 1-Ductility and Fracture Behavior, submitted to *Materials Science and Engineering A.*
12. A.J. Ramirez and J.C. Lippold, 2004. High temperature cracking in nickel-base weld metal, Part 2–Insight into the mechanism, submitted to *Materials Science and Engineering A.*
13. M.G. Collins, A.J. Ramirez, and J.C. Lippold. 2004. An investigation of ductility-dip cracking in Ni-base filler metals-Part 2, accepted to the *Welding Journal (projected publication January 2004)*
14. M.G. Collins, A.J. Ramirez, and J.C. Lippold. 2004. An investigation of ductility-dip cracking in Ni-base filler metals-Part 3, accepted to the *Welding Journal (projected publication February 2004)*

Acknowledgements

The issue of DDC in austenitic materials has been the subject of considerable study at The Ohio State University over the last 5 years. The authors wish to thank Mr. Matt Collins and Mr. Nathan Nissley whose graduate work has added greatly to our understanding of this phenomenon. We also acknowledge Mr. Jeffrey Sowards and Mr. Matthew Gonser, undergraduate students in our research group, who worked tirelessly to prepare samples for STF testing and characterization. Finally, we would like to thank our sponsors, most notably BWX Technologies, Inc. and the AWS Foundation for providing the motivation and resources for conducting these studies.

Impact of PWSCC and Current Leak Detection on Leak-Before-Break

D. Rudland, R. Wolterman, and G. Wilkowski
Engineering Mechanics Corporation of Columbus
Columbus, OH

This paper assesses the effect of using PWSCC crack morphology parameters (roughness, number of turns, and actual flow path/pipe thickness) in determining the difference in the leakage crack size, and how the difference in the leaking crack sizes changes typical margins from past LBB submittals and published reports. Several past LBB submittal cases were selected; in addition, cases from generic LBB reports published by EPRI were also selected. The results of the analyses showed that the past submittals by some NSSS companies used the surface roughness comparable to an air-fatigue crack with no turns and the actual flow path equal to the thickness of the pipe. This condition would give the shortest possible leakage flaw size. The roughness, number of turns, and actual flow path to thickness ratio for PWSCC cracks was determined from photomicrographs of service-removed cracks.

When using the PWSCC crack morphology parameters that corresponded to the crack growing parallel to the long direction of the dendritic grains (V.C. Summer and Ringhals cases), then the leakage flaw size increased 69 percent over the air-fatigue crack length at the same leak rate. Using the same critical crack size as was used in the initial LBB submittals and the published documents, the margins on the crack size changed from 1.77 to 6.0 for the initial submittals (which we also reproduced) to 0.88 to 2.74 from our calculations for a PWSCC crack.

If the crack grew in the buttered region of the bimetallic weld, then based on metallographic sections from service-removed flaws, there would be a more tortuous flow path. For this crack condition, in all but one case, the margins on the normal operating versus N+SSE crack lengths were below the safety factor of two required for LBB approval. The average margin decreased from 3.39 for the air-fatigue crack to 1.55 for the PWSCC crack growing transverse to the long direction of the dendritic grains. This was about an additional 20 percent decrease in the margin from the case of having the PWSCC grow parallel to the long direction of the dendritic grains.

These results show that LBB is difficult to satisfy for PWSCC susceptible pipe using the current SRP 3.6.3 LBB approach. This LBB assessment did not consider the possible development of a long circumferential surface crack, which would be more detrimental to LBB behavior. Such cracking behavior would violate the LBB screening criterion.

Manuscript was not available for publication in the Proceedings